Doctoral Thesis in Physics

Development and optimization of ultrasensitive magnetoresistive sensors

submitted to

Faculty of Physics
Bielefeld University

by

Anastasiia Moskaltsova, M. Sc.

Bielefeld, September 08, 2021

Declaration

I wrote this thesis by myself and used none but the indicated sources and references. Text and figures were partly taken from the corresponding publications, which originated directly from this work.

Bielefeld, 08.09.2021

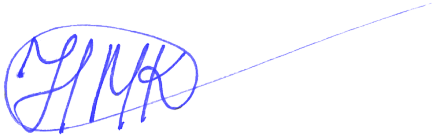

Anastasiia Moskaltsova

Reviewers
Prof. Dr. Günter Reiss
Jr. Prof. Dr. Luana Caron

Printed on non-aging paper ISO 9706
BIELEFELD UNIVERSITY, FACULTY OF PHYSICS
CENTER FOR SPINELECTRONIC MATERIALS & DEVICES

Dissertation to attain the doctoral degree of science (doctor rerum naturalium)

To my family.

”The good thing about science is that it’s true whether or not you believe in it.”
Dr. Neil deGrasse Tyson

TABLE OF CONTENTS

LIST OF ABBREVIATIONS

AC	Alternating current
AD	Alzheimer's disease
AFCM	Antiferromagnetically coupling maximum
AFM	Antiferromagnetic
AHE	Anomalous Hall effect
ALD	Atomic layer deposition
AMR	Anisotropic magnetoresistance
AMTP	Anisotropic magnetothermopower
ANE	Anomalous Nernst effect
CIP	Current-in-plane
CPP	Current-perpendicular-to-plane
CSF	Cerebrospinal fluid
DC	Direct current
DL	Damping-like
DOS	Density of states
E-beam	Electron beam lithography
ENBW	Equivalent noise bandwidth
FL	Field-like
FM	Ferromagnetic
FWHM	Full width of half-maximum
GMR	Giant magnetoresistance
HDD	Hard disk drive
HM	Heavy metal
ISHE	Inverse spin Hall effect
MEMS	Micro-electro-mechanical systems
MOKE	Magneto-optic Kerr effect
MPE	Magnetic proximity effect
MR	Magnetoresistance
MRAM	Magnetic random access memory
MTJ	Magnetic tunnel junction
NM	Non-magnetic
PD	Parkinson's disease
PHE	Planar Hall effect
Py	Permalloy $Ni_{81}Fe_{19}$
RF	Radiofrequency

RKKY	Ruderman-Kittel-Kasuya-Yosida coupling
SAF	Synthetic antiferromagnet
SD	Standard deviation
SHA	Spin Hall angle
SHE	Spin Hall effect
SIMS	Secondary-ion mass spectrometry
SMR	Spin Hall magnetoresistance
SNR	Signal-to-noise ratio
SOC	Spin-orbit coupling
SOT	Spin-orbit torque
STT	Spin-transfer torque
TC	Time constant
TMR	Tunneling magnetoresistance
USMR	Unidirectional spin Hall magnetoresistance
VSM	Vibrating sample magnetometer
XAS	X-ray absorption spectrometry
XMCD	X-ray magnetic circular dichroism
XRD	X-ray diffraction
XRMR	X-ray resonant magnetic reflectivity
XRR	X-ray reflectivity
YIG	Yttrium iron garnet

INTRODUCTION

Today we cannot imagine our lives without "smart" devices, like smartphones, computers, smart watches and even cars. Various sensors are hidden inside each of the modern devices, that are responsible for their "smartness". These tiny helpers can detect magnetic fields, acting as a compass, recognize acceleration and tilt rotations of the phone screen or diagnose various diseases and even save lives by triggering an airbag in a car [1–4]. Nowadays for example, every car has about 60 to 100 sensors inside and according to predictions, this number is going to increase to 200 [5], while in 1970 a car was nearly sensorless [6].

The sensors purpose is only to detect specific properties, *e.g* physical or chemical in quality or quantity, and send the acquired information to electronics for further processing. Depending on the parameter of interest, various types of sensors exist, including magnetoresistive (MR) sensors, micro-electrical mechanical systems (MEMS), chemical and optical sensors. The global sensor market was about 139 billion $ in 2017 and predict to grow up to 287 billion $ by 2025 [7], where the magnetic sensor market is predicted to reach 4.22 billion $ worldwide by 2026 [8].

Even though magnetic sensors account for only $\approx$1.6% of the global sensor market as of 2018, they are utilized for various applications, as for instance angle sensors in automotive [9], industrial and consumer areas [4, 10, 11], biomedical [12, 13], flexible devices [14–16], navigation [17], space exploration [18–20].

With increasing device miniaturization as well technological progress, the requirements for the MR sensors of tomorrow include ultra-high sensitivity, low noise and high signal-to-noise ratio (SNR), robustness as well as low production cost and environmental friendliness.

The main focus of this thesis is the development of highly sensitive MR sensors for early diagnosis of Alzheimer's (AD) and Parkinson's (PD) diseases in the frame of the EU Horizon 2020 MADIA Project [21]. Today worldwide around 50 million people are living with dementia, the most common type of the neurodegenerative diseases, including AD and PD. Current predictions estimate that by 2050 the number of people suffering from dementia will increase to about 152 million people [22]. At present there are no available cures for both of the disease, but most importantly, there are no means to early diagnose them.

The state-of-the-art magnetoresistive sensors, especially based on the planar Hall effect (PHE), were developed in the frame of this thesis and are a cornerstone of a multidisciplinary diagnostic platform. The main working principle of this platform is

based on detection of stray magnetic fields of magnetic nanoparticles (MNPs), which are functionalized with AD and PD specific biomarkers and can flow in a solution inside of a microfluidic channel, built on top of the MR sensor. The sensors are operated at an AC current, which excites a second harmonic response, that in turn is sensitive to the magnetic nanoparticles's stray fields and changes the sensor's second harmonic signal accordingly. As the MNPs used here are of sizes between 25 and 35 nm and their magnetic fields decay as $\approx 1/\mathrm{r}^3$, where r is a distance between a particle and the sensor's surface, it is of extreme importance not only to achieve high sensitivity, but also to bring the sensors as close as possible to the MNPs solution. One of the novel approaches utilized here, is the use of the so-called compensated thin film stack, where a top Ru layer thickness is adjusted as such to set the second harmonic response as close as possible to zero. On top of that, the noise of the device has to be characterized to properly choose the AC input current frequency and to ensure the best SNR.

Among various MR effects that are being used in today's electronics, novel promising MR effects are being discovered, as for example, so-called unidirectional spin-Hall magnetoresistance (USMR) [23]. This effect is of particular interest for modern applications, as it allows to distinguish in-plane magnetic field direction, unlike other MR effects that are quadratic with magnetization **m**. Therefore, it is a perfect candidate for future magnetic field sensors.

The USMR effect is a spintronic effect, which means it combines spin and electronic properties of a system. In this work, various thin film stacks with Co/Pt as a core were studied, in order to develop a material system with large USMR effect. This effect is relatively small. It accounts only for $\sim$ 0.002% - 0.005% of the total device resistance [24] in comparison, for example to anisotropic magnetoresistance (AMR) ($\sim$ 2-4%) or giant magnetoresistance (GMR) in spin-valves ($\sim$ 20%) [25, 26]. Therefore one established method of measuring is by utilizing the second harmonic voltage measurements for longitudinal and transverse voltages. In comparison to the DC current injection, in this method an AC current is injected into the system, which allows to separate various effects present in the device.

One of such interesting effects that emerges in systems with Pt in the vicinity of a ferromagnet (FM) is the magnetic proximity effect (MPE). It describes the spin-polarization up to a few atomic layers of Pt at the interface with the FM. Such a presence of an additional magnetic layer in a material system might lead to the emergence of new or changes in existing effects. In this work the synchrotron based technique x-ray resonant magnetic reflectivity (XRMR) was used to study the MPE. It is a powerful method to obtain a depth-resolved magnetic profile of a thin film stack.

In the following chapters, the relevant theoretical background as well as the experimental methods, used to obtain the data, will be introduced.

The experimental results chapters are distinct by topic and they will put in light the details of development and characterization of the corresponding samples.

The results presented in this thesis have already been published in various peer-reviewed journals or are in preparation for publication. The corresponding articles are referenced in the respective chapters.

CHAPTER 1

THEORETICAL BACKGROUND

In the modern world scientific progress helps in all areas of human life. In the content of the health and disease treatment, state-of-the-art science can not only improve people's lives, but also diagnose life-threatening diseases. In this chapter a brief introduction to the two neurodegenerative diseases, Alzheimer's and Parkinson's, will be given. Further in this chapter, the physics behind the magnetic sensors, used for the detection of the biomarkers, associated with the AD and PD, will be discussed. As a last point, the theory behind the spin Hall-based effects, as well as the magnetic proximity effect will be given, since they might be present in a magnetic thin film system and thus influence the output of a MR sensor.

1.1 Alzheimer's and Parkinson's diseases

Alzheimer's disease is one of the neurodegenerative diseases, which main symptoms are progressing loss of memory and cognitive decline, including the time or place confusion. Additionally, behavioral symptoms as personality changes and depression often occur [27]. Presently, there are no cure available, moreover, there are no reliable diagnostic methods, and none of the existing methods can identify the AD at the early stages, before any symptoms occur. To better understand the mechanism behind the AD progression, a closer look into the nervous system must be taken.

The AD starts to develop as early as 20 years before the first symptoms are noticeable. When people reach final stage of the disease they are bed-bound and are in need of constant care. Ultimately, AD is fatal and in 2016 accounted for over 2 million deaths globally, out of which almost half a million in Western Europe [28].

There are two proteins in the brain that are heavily involved in Alzheimer's progression. One of them is β-amyloid, which reaches abnormal levels in the brain of someone with Alzheimer's and forms plaques outside neurons that collect between neurons and disrupt cell function (see Fig.1.1). These β-amyloid plaques contribute to cell death as they interfere with neurons' communication at synapses [27]. The second protein, called tau (τ) protein, forms neurofibrillary tangles inside neurons and thus blocks the neuron's transport system. At the early stages of the disease the immune system is acti-

vated and clears the plaques and tangles, however with time it cannot keep up and that is the time, when a patient starts to show the first symptoms.

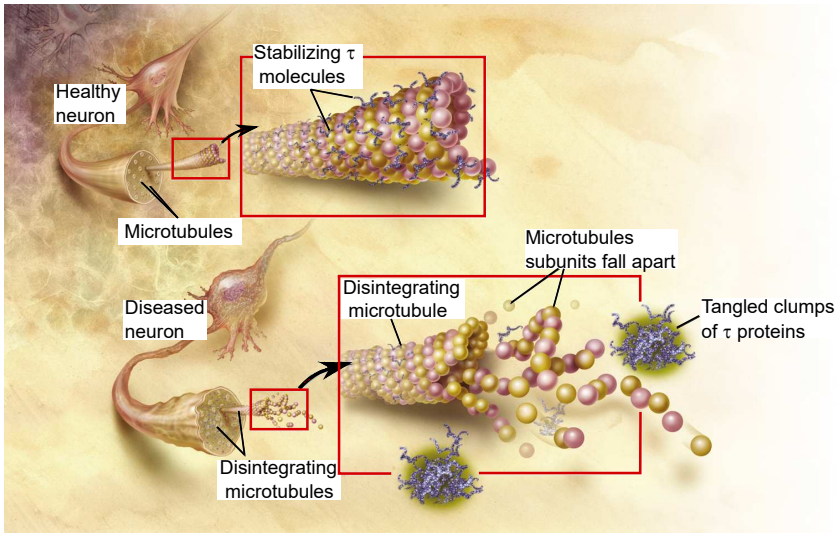

Figure 1.1: Comparison of the healthy and AD-damaged neurons (Diagram via Wikimedia Commons).

Unfortunately, it is not clear, how exactly these proteins relate to each other, or what makes them to accumulate to such damaging levels [22].

Parkinson's disease is another type of progressive neurodegenerative disorder, that affects the dopamine producing nerve cells in the brain. Parkinson's disease symptoms include muscle rigidity, rest tremors, changes in speech, gait and bradykinesia, as well as other non-motor symptoms like depression and sleep disorder. Current detection methods are based on clinical criteria, as there is no definitive test for the diagnosis except for the confirmation of the hallmark Lewy body on autopsy [29]. Additionally, it is challenging to identify the PD at the early stages, when the signs and symptoms overlap with the other syndromes [30]. However, unlike in case of AD, Parkinson's patients do not loose their identity and can live long with the disease.

One of the main protein linked to the PD progression is α - synuclein [31], which is a natively unfolded presynaptic protein. When fibrillar α - synuclein is present in the brain it acts as a major structural component of Lewy bodies in PD progression. When accumulated, α - synuclein disrupts basic cellular functions and leads to death of dopamine-generating cells in the *substantia nigra*, a region of the midbrain [31]. Current treatments of PD include Levodopa, the most commonly prescribed medicine, which is transformed into dopamine by the brain cells. Among other medications and treatments are dopamine agonists, the drugs that act like dopamine in the brain, and deep

brain stimulation. The treatments can help to relieve the symptoms, but the disease is incurable.

As both AD and PD start developing decades before the first symptoms are visible and there are no reliable methods to detect the diseases at early stages, yet, it is crucial to develop accurate and versatile early diagnoses tools. This could help not only to start an early treatment and possibly decelerate the disease progression, but also to boost research and development of the AD and PD cure.

One of the solutions for the early diagnostics can be the combination of the various state-of-the-art technologies from different fields (biology, chemistry, physics, medicine) into building a multidisciplinary platform, which can quickly and accurately detect the targeted biomarkers corresponding to the disease of interest in the patient's sample. Ideally, this would involve saliva or blood samples, as they are easy to collect and handle in comparison to the cerebral spinal fluid, which is used nowadays.

Such a technology is a fundamental milestone of the EU Horizon 2020 MADIA project [21]. In this project magnetoresistive sensors of different types have been developed for further use as sensors of magnetic nanoparticles, which bind to the targeted biomarkers. The main results of the work within the MADIA project is discussed later in this thesis (see Chapter 3).

1.2 Magnetoresistive effects

Magnetoresistive effects play an important role in today's electronics and are the basis of many MR devices available nowadays. Among the wide variety of applications, ones of the most common are the hard disk drives (HDDs), magnetic random access memory (MRAM) [32–34], magnetometers, biomedical devices and others [4, 10–17].

As the name suggests, magnetoresistance is a change of the electrical resistance in the presence of a magnetic field. The first experiments were conducted in the 19th century and currently there is a whole family of MR effects, that differ in their underlying mechanisms, but ultimately are characterized by the MR ratio, which is the change of the electrical resistance in the presence and absence of the external magnetic field.

In this work, the MR sensors based on several magnetoresistive effects, in particular anisotropic magnetoresistance, the planar Hall effect, tunneling magnetoresistance (TMR) and unidirectional spin-Hall magnetoresistance will be discussed. The effects, being different in their working principle, also differ in the production cost, as well as in such important parameters like sensitivity, noise and robustness. Depending on the target the parameters can vary in their significance. For example in space-related applications the ability to function under harsh environmental conditions may be a deciding

factor [20].

1.2.1 Anisotropic magnetoresistance and planar Hall effect

The first observation of a magnetoresistance was carried out by William Thomson (Lord Kelvin) in 1856. He discovered that the resistance of an iron piece increases if the current and magnetic field are applied in the same direction [35]. If the current is applied perpendicular to the magnetic field, the resistance of the iron piece decreases. After the initial experiments with an iron slab, Thomson continued his experiments with nickel. He detected the similar behavior as previously, however, stronger in amplitude [35]. This effect is known today as the anisotropic magnetoresistance effect. The change of the electrical resistance in this case is caused by the simultaneous action of spin-orbit interaction and the magnetization of the ferromagnet [36].

The AMR effect is measured in the longitudinal geometry as shown in the Fig.1.2 (a) (green curve). The resistivity, then depends on the angle between the magnetization and the current and can be expressed as follows

$$\rho_{xx} = \rho_{\perp}(1 + \frac{\rho_{\parallel} - \rho_{\perp}}{\rho_{\perp}} \cos^2\theta), \tag{1.1}$$

with $\rho_{\parallel}$ and $\rho_{\perp}$ being the resistivities along and perpendicular to the magnetization, and θ is the relative angle between the magnetization vector and the current [37]. The AMR ratio is a measure of the effect's amplitude and can be expressed as [25, 38]

$$\frac{\Delta\rho}{\rho} = \frac{\rho_{\parallel} - \rho_{\perp}}{\rho_{\perp}}. \tag{1.2}$$

It took over a century to detect the equivalent of AMR in the transverse geometry, which is called planar Hall effect [39]. Similarly as for AMR, the equation for the PHE can be derived as [37]

$$\rho_{xy} = (\rho_{\parallel} - \rho_{\perp}) \sin\theta \cos\theta. \tag{1.3}$$

Figure 1.2 shows an example of the AMR and PHE measurements in a four-point geometry for a Hall cross structure. Here, ρ_{xx} corresponds to AMR and ρ_{xy} to PHE, while j denotes the direction of the applied current. As the result of such a measurement, an angular dependence of both effects can be determined (see Fig.1.2 (b)).

Ultimately, the both effects have the same origin as was shown for the nanocrystalline $Co_{20}Fe_{20}B_{20}$ [37]. The major mechanism behind the effects depend on the material. In strong ferromagnets it is linked to the spin-orbit coupling (SOC), which enables the *s-d* scattering. Campbell *et al.* [40] demonstrated, that when spin-orbit coupling

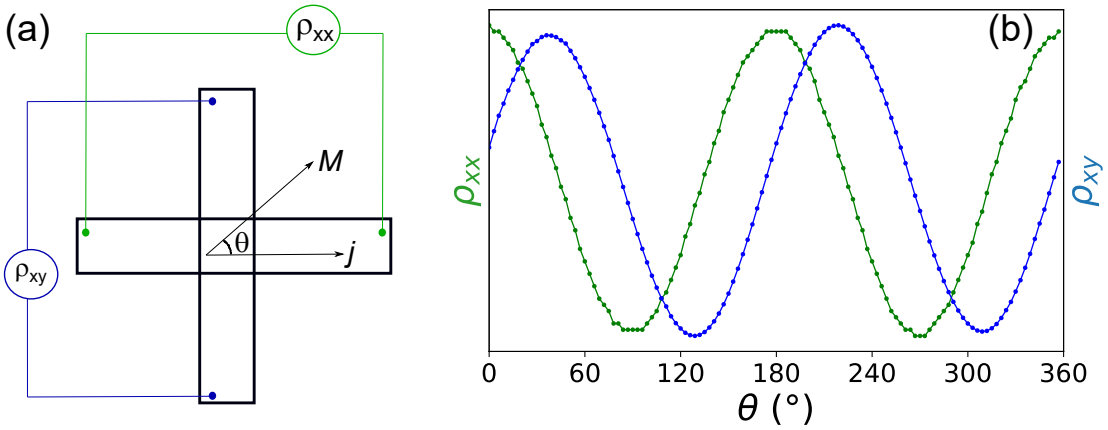

Figure 1.2: AMR and PHE effects comparison. (a) Shows a typical Hall cross structure and measurement geometry for the longitudinal ρ_{xx} (AMR) and transverse ρ_{xy} (PHE) resistance cases. (b) Represents an exemplary angular dependence of the both effects.

in the *d* band is present in a system, it makes the mixing of spin-up electrons from the *d* band into the spin-down *d* band possible. Furthermore, the calculations show that during the mixing process there is a part of resistivity originating from the spin-down electrons, is shifted to the spin-up electrons resistivity and here is where the anisotropy comes from, since this effect appears to be about two times stronger, when the traveling direction of the electrons relative to the magnetization is parallel.

Both AMR and PHE are widely used for sensing applications, mostly as magnetic field sensors [18, 41], rotational sensors [42] and others. Although both effects are utilized nowadays, PHE has a number of advantages over AMR, e.g. linearity near zero field, low signal offset ($<$ mV) [43]. The effect size in case of AMR varies for different materials, however typically do not exceed few percents at room temperature. The AMR amplitudes of 2.0 % for *fcc* Co and 2.2 % for *fcc* Ni were reported by Malozemoff *et al.* [44]. While in the case of CoFeB the AMR amplitude of 0.22 % was measured [37]. However, with the discovery of giant magnetoresistance and later tunneling magnetoresistance, most of the attention has been shifted towards the newer effects with higher MR ratios.

1.2.2 Giant and tunneling magnetoresistance

In 1988 A. Fert and P. Grünberg independently reported a new magnetoresistance effect [45, 46] for Fe/Cr layers with antiferromagnetic interlayer exchange coupling. In both cases the measurements were performed at low temperatures regime and the measured effect size was 50% at 4 K and 10% at 5 K. The new effect was called Giant

Magnetoresistance (GMR) and has a different physical origin as compared to AMR and PHE. For the discovery of Giant Magnetoresistance A. Fert and P. Grünberg were awarded the Nobel Prize in Physics in 2007.

Unlike the AMR, the GMR effect occurs in tri- or multilayer systems, with two ferromagnetic materials being sandwiched between a non-magnetic conductor (eg. Cu, Cr, Ru etc), with layer thicknesses of tenth to few nanometers. Due to the Ruderman-Kittel-Kasuya-Yosida (RKKY) [47–49] interlayer exchange coupling, the ferromagnets can be coupled ferromagnetically or antiferromagnetically. Figure 1.3 depicts the oscillating nature of the RKKY coupling, in which the positive sign of the coupling strength corresponds to antiferromagnetic (AFM) and negative sign to ferromagnetic (FM) coupling, respectively. In the presence of an external magnetic field, the magnetization of both ferromagnetic layers is forced to align parallel to each other.

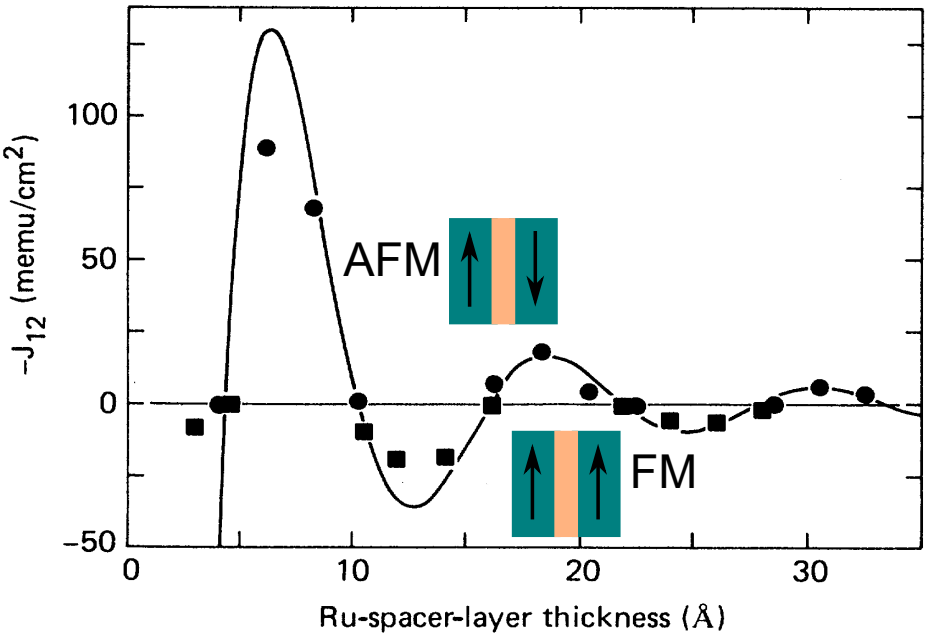

Figure 1.3: RKKY interlayer exchange coupling strength as a function of interlayer material thickness, in this example Ru sandwiched between $Ni_{80}Fe_{20}$ ferromagnets (adapted from Ref. [50]).

Figure 1.4 represents the two distinct states with maximum and minimum resistances. If the layers are magnetized in the opposite direction with no external magnetic field applied (Fig.1.4 (a)), the resistance is higher, when compared to the parallel alignment in the presence of a strong magnetic field (Fig.1.4 (b)).

Such a behavior can be explained by the spin-dependent scattering. This mechanism

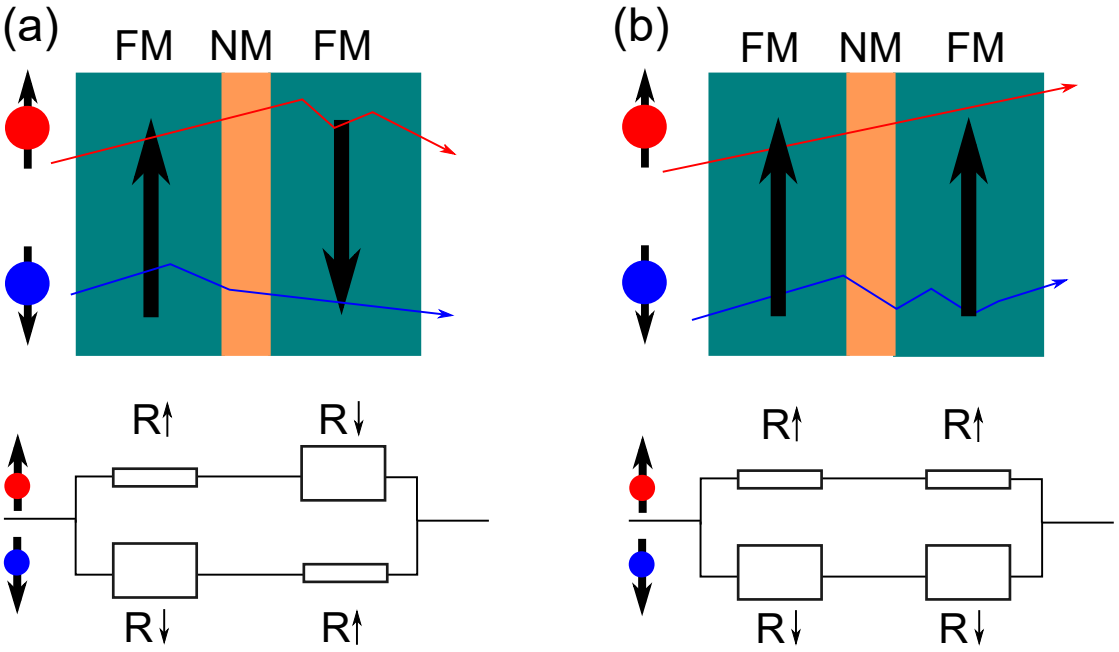

Figure 1.4: GMR effect shown for a trilayer structure FM/NM/FM, with FM and NM being ferromagnetic and non-magnetic materials respectively. (a) Describes a case of the AFM alignment. (b) Represents the ferromagnetic alignment of the two FM. The parallel resistances scheme shown below visualizes high (R↓) and low (R↑) resistance states.

can be explained by the two channel model, first proposed by Mott in 1936 [51]. In this model Mott describes the electrical current in metals separated in two independent parts, one with spin-up (↑) and one with spin-down (↓) electrons. Thus, the difference in the resistance occurs from different scattering of the majority and minority electrons. Therefore, the GMR ratio can be expressed as [52, 53]

$$\frac{\Delta R}{R}(\%) = \frac{(R\downarrow - R\uparrow)^2}{4(R\uparrow R\downarrow)}, \tag{1.4}$$

in which $\frac{\Delta R}{R}$ is the GMR ratio and R↑(↓) are the resistance of the spin up (spin down) electrons.

The above discussed basics of the GMR effect are shown for simple multilayer structures. In general, the GMR systems can be sorted into three groups, with different control of the magnetic order [54]:

- Ferromagnetic multilayers, coupled antiferromagnetically. The simplest structure FM/NM/FM as used in [45, 46].

- Multilayers with different FM layers coercive fields, e.g. FM_1/NM/FM_2, as for

example $Ni_{80}Fe_{20}$/Cu/Co/Cu, first shown by Shinjo *et al.* [55].

- Spin valves, with one of the FM layers being pinned by a neighboring AFM layer, thus making this ferromagnet "fixed" or "pinned", while the second FM layer is then free to rotate. Such a concept was first introduced by Dieny and colleagues [56] and became widely used due to high sensitivity in near-zero fields.

Each of the above mentioned groups have their advantages and disadvantages, and used depending on the application, available production facilities etc.

Already in 1975, i.e. long before the GMR, another MR effect was reported, in which the non-magnetic conducting layer is substituted by an isolator, only few atomic layers thick. This effect is called tunneling magnetoresistance, due to the quantum tunneling process of the electrons through the insulating barrier. A typical system to realize TMR device is a magnetic tunnel junction (MTJ), as depicted in Fig. 1.5 (a).

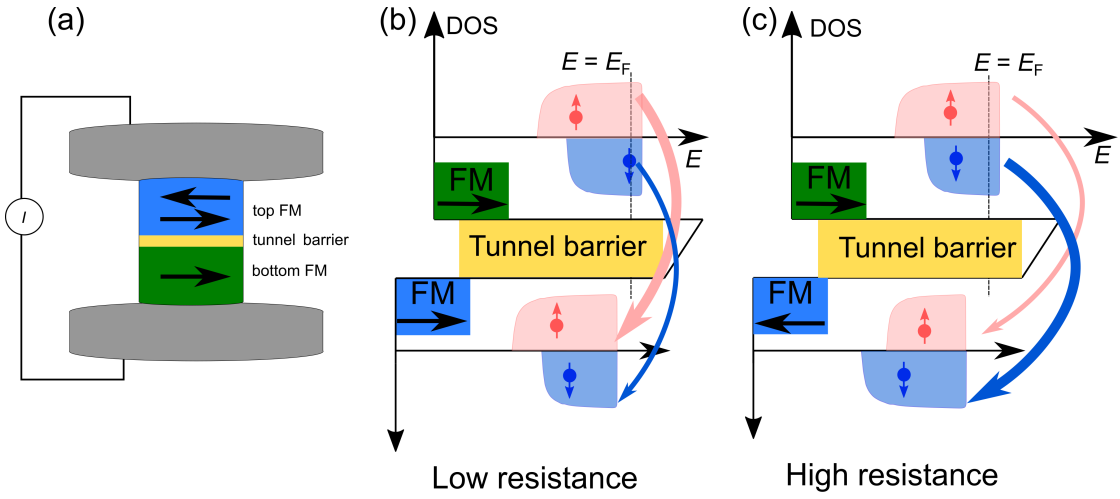

Figure 1.5: (a) An example of a MTJ in the current-perpendicular-to-plane (CPP) geometry. (b) The tunneling process in the case of the parallel alignment of the magnetizations of both FM electrodes. (c) Illustration of the antiparallel alignment of the magnetizations.

The first reported TMR ratios were measured at low temperatures and did not exceed few tenth of percent [57, 58]. These works did not gain enough attention back in their time and only after the discovery of GMR, a significant amount of research was put towards improvement of the TMR effect. Moodera and colleagues as well as Miyazaki and Tezuka [59, 60] reported the first TMR observations at room temperatures with the effect size of 10% for CoFe/Al_2O_3/Co and and Fe/Al_2O_3/Fe structures, in which amorphous Al_2O_3 was used as an insulating barrier. Later, the typical TMR ratios of

35% [61, 62] were achieved with alumina barriers and a maximal value of 80% was reported by Wei *et al.* [63] for microscale ring-type MTJs.

With the start of utilization of the single crystalline MgO barriers, the TMR ratios improved as high as 604% at room temperature as reported by Ikeda *et al.* [64]. MgO single crystal barrier promotes the coherent tunneling through the MTJ, thus improving drastically the TMR ratios as compared to the amorphous alumina barriers [65–67]. One of the direction towards the TMR enhancement, is the usage of Heusler alloys or spinel as FM material [68–70], with a predicted TMR of 1000% for spinel MTJs [71].

1.3 Noise in magnetoresistive sensors

Noise, as any random undesirable disturbance in a system which interferes with its intended operation [72], is important whenever the amplitudes of the processed signals are similar to those of the existing noise. Noise is responsible for errors in measuring the level of a weak analog signal. Consequently, noise establishes the ultimate limit of measurement sensitivity. In general, noise can be divided into intrinsic (everything coming from *inside*) and extrinsic (everything coming from *outside*), with the terms *inside* and *outside* being relative to a system under study.

The total intrinsic noise, typically present in a magnetoresistive sensor, can be described as the square root of the sum of the squares of all the incoherent noise sources

$$S_{total} = \sqrt{S_{1/f}^2 + S_{thermal}^2 + S_{shot}^2} \qquad (\frac{V}{\sqrt{Hz}}), \tag{1.5}$$

with $S_{1/f}$ corresponding to the flicker noise, called sometimes pink noise and it has a $1/f$ spectrum. This type of noise can have both magnetic and electrical origin and can be typically described as following [73]

$$S_{1/f} = \sqrt{\frac{V^2 \gamma_{\mathrm{H}}}{N_{\mathrm{C}} f}}, \tag{1.6}$$

with V being the applied voltage, γ_{H} is Hooge constant, N_{C} is charge carrier density.

The terms $S_{thermal} + S_{shot}$ are thermal and shot noise, respectively, which are frequency independent and called white noise. Thermal noise is present in every system due to random motion of free electrons within a piece of a conductor. In 1928 H. Nyquist derived a formula for an idealized resistor, while J.B. Johnson confirmed it experimentally in the same year, hence, thermal noise is often called Johnson-Nyquist noise [74, 75]

$$S_{thermal} = \sqrt{4k_{\mathrm{B}}TR}, \tag{1.7}$$

in which k_B is Boltzmann's constant, T the temperature (on the Kelvin scale) and R the resistance of the material.

Shot noise, on the other hand, emerges due to fluctuations of the charge current and can be described by the Schottky formula, expressed for voltage by [76]

$$S_{shot} = \sqrt{2eI_{rms}R^2}, \tag{1.8}$$

with e being the electron charge and I_{rms} the root mean square AC charge current amplitude.

Another important parameter is the so-called $1/f$ knee, that gives a frequency, above which white noise is dominant. It is paramount to know this frequency when operating in the AC regime, to be sure no flicker noise is present. In general, even in case of highly sensitive MR sensors, large noise in the operating frequency range can be an obstacle and reduce signal-to-noise ratio.

In principle, an objective comparison of the noise in various MR sensors is problematic since the size, magnetic materials and their thickness, as well as shape and overall complexity of the system typically vary considerably. Overall, the requirements to noise and SNR are usually set by the final application of the MR sensor.

1.4 Spin Hall effects

The ability to create, propagate and control spin currents is at the heart of today's spintronics. One of the main mechanisms behind is the spin Hall effect (SHE), which arises in materials with strong spin-orbit coupling. SHE thus allows to convert a charge current into a transverse spin current. Nowadays, many spintronic devices utilize SHE based phenomena, such as the spin Hall magnetoresistance (SMR), unidirectional SMR and spin-orbit torques (SOTs). For instance, unlike a conventional spin-transfer torque (STT) MRAM, for which high charge current densities are required to switch the magnetization, SOT based MRAM could need two to three orders of magnitude less charge current density to flip the magnetization state. Hence, such a memory cell would be more robust and thermally stable as less Joule heating affects the system [77–79].

In 1879, Edwin Hall performed experiments with metallic conductors and found that such materials generate a charge voltage in transverse direction [80] as depicted in Fig. 1.6 (a). This behavior was attributed to the Lorentz force acting on the electron charge current [81]. However, later he reported a different effect of magnetic and non-magnetic

conductors. In case of a ferromagnetic material, in addition to the contribution proportional to the magnetic field, there was another, magnetization dependent, component. This additional component is today known as anomalous Hall effect (AHE) (see Fig. 1.6(b)).

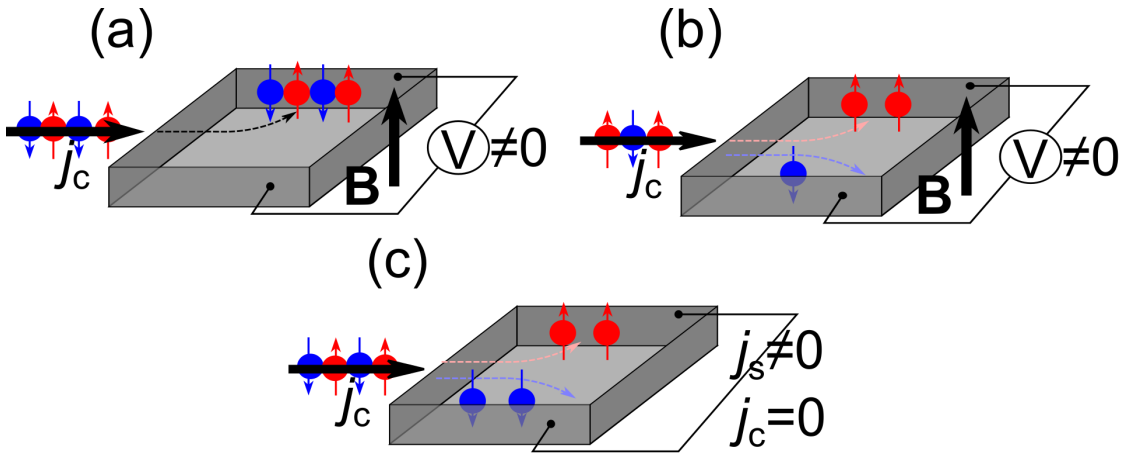

Figure 1.6: A schematic representation of the different Hall effects. (a) Hall effect in metals, with j_c being the charge current density, **B** the magnetic field, applied perpendicularly to the sample plane. (b) AHE in ferromagnetic materials. (c) The SHE, for which in the absence of an applied magnetic field electrons with different spins are deflected transversely, j_s spin current can be measured perpendicularly to the injected charge current.

In contrast, in paramagnetic materials with strong SOC (e.g. Pt, Ta, W), a net transverse spin current is detected when a charge current is driven into the material, as shown in Fig. 1.6(c), without any additional out-of-plane magnetic field.

The first theoretical prediction of the possibility to transform charge current into spin current by means of SOC was discussed in 1971 by Dyakonov and Perel [82]. The pioneering experimental confirmation followed few years later, when Chazalviel and Solomon measured quantitatively the spin Hall effect of InSb [83] and in Ge [84] with exceptionally high accuracy. However, the more intensive research emerged with the works of Hirsch *et al.* and Zhang *et al.* three decades later [85, 86], which revived interest on the topic. The subsequent experimental observations of the SHE were then reported for semiconducting GaAs and InGaAs [87, 88].

There are several mechanisms, responsible for the SHE, which can be divided into intrinsic and extrinsic effects. Figure 1.7 depicts a schematic representation of the three mechanisms, which include skew scattering and side jump (extrinsic), and intrinsic.

In the case of the spin skew scattering mechanism (see Fig. 1.7(a)), SOC creates an

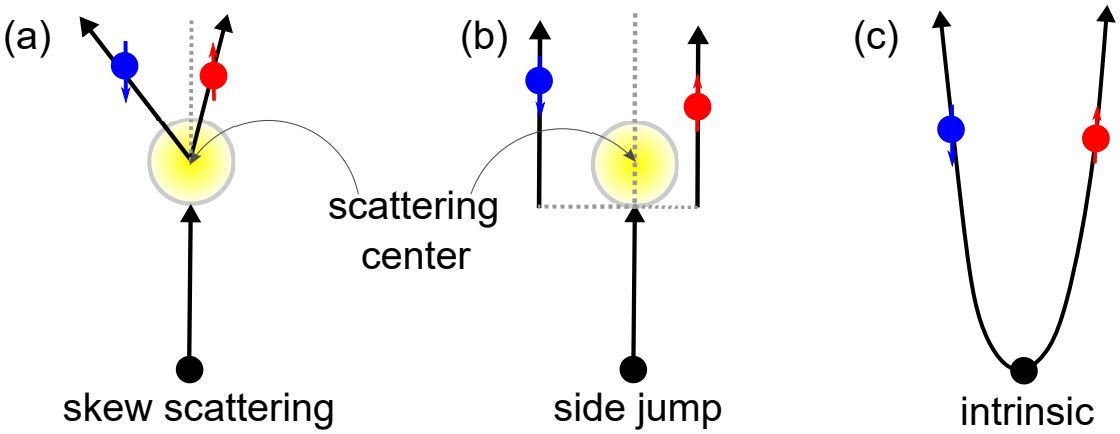

Figure 1.7: A sketch of the different SHE mechanisms. (a) Spin skew scattering. (b) Side jump. (c) Intrinsic Spin Hall effect.

effective magnetic field gradient. Thus, a net force to or away from a scattering center exists. Hence, when SOC is present in a system, spin skew scattering generates the SHE [81, 89]. Side jump scattering arises via difference in spin dependent acceleration and deceleration. After a number of scattering processes this creates an effective transverse displacement of the electron (see Fig. 1.7(b)). In contrast, intrinsic SHE arises in the absence of scattering due to the Berry curvature of the crystal's band structure, as shown in Fig. 1.7(c).

As a measure of charge to spin current conversion effectiveness, a spin Hall angle θ_{SH} is introduced as

$$\theta_{\mathrm{SH}} = \frac{j_s}{j_c}, \tag{1.9}$$

with j_{s} and j_{c} being spin and charge current densities, respectively. Spin Hall angle θ_{SH} values vary for different materials. Among the largest reported θ_{SH} are -33% for β-phase W [90] and $\sim$ 10% for Pt. However, the θ_{SH} values vary strongly depending on the deposition method and parameters, such as temperature and impurities, as it was shown for Pt by Sagasta *et al.* [91]. They measured the spin Hall angle of 10% for sputtered Pt films which correspond to the moderately dirty regime. In contrast, the authors report $\theta_{\mathrm{SH}} < 3\%$ for the superclean metal regime, obtained via evaporated Pt. Alternatively, instead of single materials, various alloys are investigated nowadays in order to enhance the spin Hall angle, for example $W_{0.7}Hf_{0.3}$ all amorphous alloy (θ_{SH} = 20%) [92] or $Pd_{0.1}Pt_{0.9}$ (θ_{SH} =18%) [93].

The SHE is responsible for various phenomena in spintronics applications. For instance, a new type of magnetoresistive effect, based on SHE, was reported in 2012 [94, 95] and is called spin Hall magnetoresistance (SMR). Various explanations exist for

the origins of the SMR, as for example Huang *et al.* discuss SMR in terms of a static magnetic proximity effect in Pt for Pt/yttrium iron garnet (YIG) bilayers [96]. It was also shown that SMR can be explained by a non-equilibrium proximity effect, which is generated by SHE and inverse spin Hall effect (ISHE) [95].

1.4.1 Unidirectional spin Hall magnetoresistance

Recently, another type of SHE-based magnetoresistance was discovered by Avci *et al.* [97], for which the resistance of a sample changes, when either charge current or magnetization direction is reversed. Therefore, it was named unidirectional spin Hall magnetoresistance. Unlike other MR effects (AMR, GMR, TMR), this effect is linear in magnetization, meaning 0° and 180° in plane magnetization states can be distinguished. Thus, USMR can be potentially used as an in-plane magnetic field sensor, as well as for memory applications [24].

The USMR was first detected as nonlinear longitudinal resistance term of second harmonic order (2ω). Such detection is possible, when an alternating charge current is injected into the system (more details on the measurement technique will be given in Chapter 2). The detected signal was found to have a distinct angular dependence $R_{2\omega} \sim \sin\theta \sin\varphi \sim M_y$, for which θ and φ are the angles depicted in the inset of Fig. 1.8.

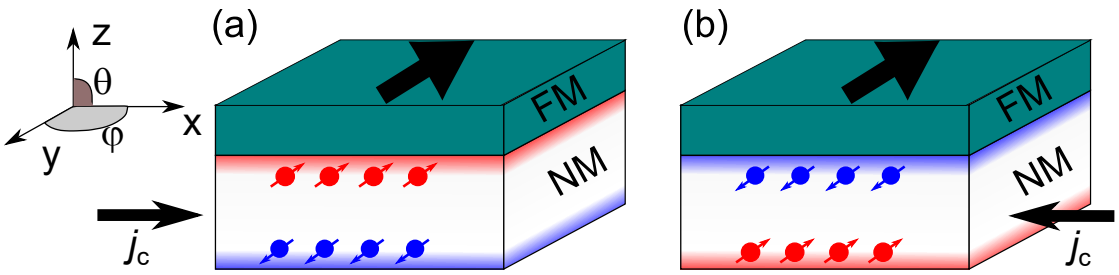

Figure 1.8: A schematic description of the USMR. The inset on the left hand side shows the axes, with φ being the angle between the injected charge current j_c and the FM magnetization. Due to the SHE, a spin accumulation at the FM/NM interface is generated. (a) Represents the case when the spin accumulation at the FM/NM interface has the same direction as the magnetization of the adjacent FM. (b) Depicts the case when the charge current direction is 180° - rotated, resulting in the opposite directions of the spin accumulation at the interface and the magnetization.

Figure 1.8 describes in detail the USMR effect for the case of FM/NM bilayer. When a charge current is injected into such a system, a spin accumulation in the NM will be generated due to the SHE at the FM/NM interface. Hence, when the direction of the

spins at the FM/NM interface and the magnetization of the ferromagnet are matching, a high resistance state is observed (Fig. 1.8(a)). On the other hand, when the direction of the injected charge current is reversed, as can be seen in the Fig. 1.8(b), the system is in the low resistance state. Such a difference of the resistances arises from the spin dependent electron mobility in FM, similarly to the current-in-plane GMR effect [97, 98].

The USMR effect has common features of the current-in-plane GMR and SHE. It can be described by the drift-diffusion model, for which two separate conduction channels for the majority and minority electrons exist. When the SHE is present in a system, a splitting of the spin-dependent electrochemical potentials occurs. Thus, a net spin accumulation at the interface $\mu_s = \mu^{\uparrow} - \mu^{\downarrow}$ exists, with $\mu^{\uparrow}$ and $\mu^{\downarrow}$ being the spin-dependent electrochemical potentials for spin $\uparrow$ and spin $\downarrow$, respectively. As was theoretically calculated by Zhang and Vignale [98], the USMR depends strongly on both FM and NM layer thickness. When one of the layer thickness (t) is smaller than the spin diffusion length (λ), the USMR would be non-existent. While for the case of thicker films, with $t \gg \lambda$, a larger portion of the current is shunted into the bulk and consequently the interfacial effects are non-pronounced, leading to decrease of the USMR effect, as it was studied experimentally in detail by Yin *et al.* [99].

Usually, other SHE-related phenomena are also present in systems exhibiting the USMR effect. One of those effects is the SOT.

1.4.2 Spin-orbit torques

In materials with strong spin-orbit coupling like Pt, Pd, W, Ta, due to SHE, SOTs can emerge, which can affect and eventually switch the magnetization of an adjacent ferromagnet [100–103]. The first discussion on the possibility of switching magnetization via current was suggested by Slonczewski in 1996 [104]. The SOTs can be described by the Landau-Lifshitz-Gilbert-Slonczewski equation

$$\frac{\partial \vec{m}}{\partial t} = -\gamma \vec{m} \times H_{eff} + \alpha \vec{m} \times \frac{\partial \vec{m}}{\partial t} + \frac{\gamma}{M_s} \vec{T}, \tag{1.10}$$

in which γ is the gyromagnetic ratio, α is the Gilbert damping term, M_s is the saturation magnetization and $\vec{T}$ is the sum of all torques. The unitary magnetization direction $\vec{m}$ can be defined as $\frac{\vec{M}}{M_s}$.

In the case of SOTs, the term $\vec{T}$ can be described as

$$\vec{T} = \vec{T}_{FL} + \vec{T}_{DL}, \tag{1.11}$$

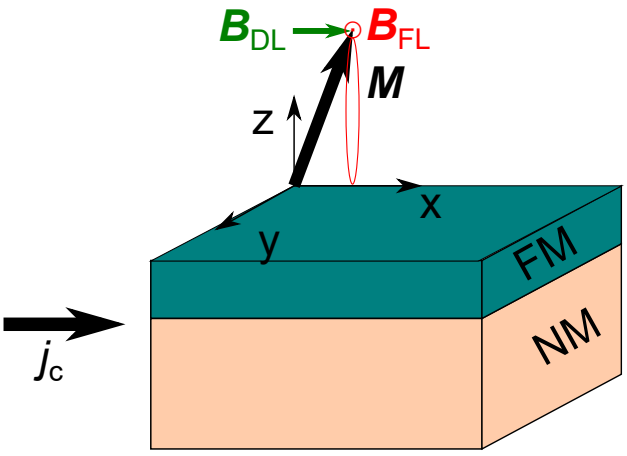

Figure 1.9: A schematic depiction of the SOTs generated by the SHE in a FM/NM bilayer. Here, the case of the out-of-plane magnetized FM is shown, with the magnetization vector $\overrightarrow{M}$ represented by a black arrow.

with $\overrightarrow{T}_{FL}$ and $\overrightarrow{T}_{DL}$ being the field-like (FL) and damping-like (DL) SOTs, respectively. These torques can be represented via the effective magnetic fields $\overrightarrow{B}_{FL,DL}$ as [79]

$$\overrightarrow{T}_{FL,DL} = \overrightarrow{M} \times \overrightarrow{B}_{FL,DL}. \tag{1.12}$$

When a charge current j_c is applied along the x direction as depicted in Fig.1.9, the effective fields can be rewritten as

$$\overrightarrow{B}_{FL} = B_{FL}\overrightarrow{y}, \tag{1.13}$$

$$\overrightarrow{B}_{DL} = B_{DL}\overrightarrow{m} \times \overrightarrow{y}. \tag{1.14}$$

From the Eq. (1.13), it can be seen that $\overrightarrow{B}_{\mathrm{FL}}$ originating from the field-like SOT acts on the magnetization as a transverse magnetic field, as shown in Fig. 1.9 (in red color). DL effective field B_{DL}, in contrast, is also called "longitudinal field" and is acting similarly to the Gilbert damping, as depicted in Fig. 1.9 with a green arrow. Figure 1.9 shows an example of both FL and DL effective fields acting on the magnetization in case of an out-of-plane magnetized FM. The origin of the DL and FL torques are being under debate in the past years. It has been proposed that the DL SOT originates from the SHE, while FL SOT is associated to a simultaneous action of spin Hall and Rashba effects [105]. The typical values of the B_{DL} and B_{FL} are of the order of 0.1 to 10 mT, whereas for the case of DL torque, the sign correlates with the θ_{SH} sign of the NM.

As the DL and FL effective fields depend strongly on the injected current density, a spin torque efficiency term has been proposed in order to compare the SOT strength in

various systems. The spin torque efficiency is defined as

$$\xi_{DL,FL} = \frac{2e}{\hbar} M_s t_{FM} \frac{B_{DL,FL}}{j_c}. \tag{1.15}$$

Here, e is the electron charge, $\hbar$ is the Planck constant, t_{FM} is the thickness of the ferromagnetic layer. The value of ξ reflects the ratio between the effective spin current absorbed by the FM and the charge current injected in the NM. Therefore, in the case of the DL torque, the efficiency is equal to the spin Hall angle θ_{SH}. As a result, the determination of the SOTs in a system is one of the most efficient ways to extract the bulk θ_{SH} values in the limit of a transparent interface and insignificant memory loss [79].

1.5 Magnetic proximity effect

It was mentioned before that in some cases, when a material such as Pt is in the vicinity of a ferromagnet, the magnetic proximity effect (MPE) arises, thus leading to a spin-polarized Pt layer at the Pt/FM interface. Pt and Pd have a large θ_{SH} and, therefore, are often used as spin-current generator or detector. The detection of various effects such as spin Seebeck, SMR and others can be hampered, if there is MPE in Pt. Hence, it is of great importance to study and analyze the MPE in spintronic systems in order to obtain a clear picture of the origin of the effects.

A number of materials, which are close to the Stoner criterion [106], can become magnetic due to the MPE, including Pt [107], Pd [108, 109], V [110, 111], Cr [112] and Ru [113].

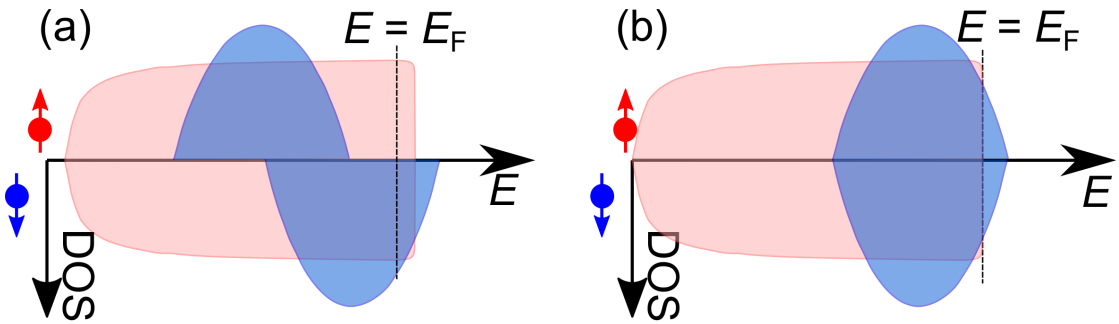

Figure 1.10: Schematic view of the density of states (DOS) in FM and NM. (a) DOS for ferromagnetic 3*d* metals. (b) DOS of a 3*d* paramagnetic metal. E_F denotes the energy at the Fermi level (adapted from Ref. [114]).

To better understand the nature of the MPE, it is helpful to look back at the origins of ferromagnetism. In 1928 Heisenberg [115] introduced a theory, in which the interaction

energy between two spins S_1 and S_2 can be described as

$$w_{12} = -2J_{exchange} S_1 \cdot S_2, \tag{1.16}$$

with J_{exchange} being the exchange integral. Ferromagnetic alignment occurs in systems with $J_{\text{exchange}} > 0$, while in the case of $J_{\text{exchange}} < 0$, antiferromagnetic alignment is favorable [116]. This behavior is the consequence of the energy minimization in Eq. (1.16), in which energy is lowest when $J_{\text{exchange}} > 0$ and $S_1 \parallel S_2$.

One of the main features of any ferromagnetic material is the presence of a spontaneous magnetization. Such a magnetization results from the filling of incomplete energy shells ($3d$ and $4f$). Figure 1.10 depicts a comparison of the density of states (DOS) between a $3d$ ferromagnet (e.g. Co, Ni, Fe) and a paramagnetic $3d$ metal. Here, for the case of the NM, the electrons fill empty states above the Fermi level due to the Pauli exclusion principle [117]. In such a case the kinetic energy of the whole system is high. However, for the FM case, due to the $3d$ electron band the DOS at the Fermi level is higher and therefore the kinetic energy is smaller. Thus, minimizing the overall energy of the system and making ferromagnetic ordering energetically favorable. Hence, a Stoner criterion of ferromagnetism [106] can be introduced as

$$J_{\text{exchange}} D(E_F) > 1, \tag{1.17}$$

with $D(E_F)$ being the density of states at the Fermi level. This means that materials with either a large exchange integral or a high DOS at the Fermi level can be stable ferromagnets.

Materials such as Pt, Pd and some others, with the Stoner criterion <1 (0.65 and 0.8 for Pt and Pd, respectively [118]) can still become ferromagnetic up to a few atomic layers, when brought in vicinity of a stable ferromagnet. Such a phenomenon occurs due to the exchange interaction with the adjacent FM and this can alter the exchange energy to promote spin dependent band splitting, thus making the NM ferromagnetic.

Up to recently, this phenomenon has been studied mostly by x-ray magnetic circular dichroism (XMCD) [119–124]. XMCD influences the x-ray refractive index and changes it relative to the magnetization of the whole sample. The refractive index of a material is given as

$$n = 1 - \delta + i\beta. \tag{1.18}$$

However, due to magnetic circular dichroism in the magnetic material, the optical parameters δ and β are altered by a fraction $\pm\Delta\delta$ and $\pm\Delta\beta$, depending on the helicity

of the x-rays ($\uparrow$ for circularly right and $\downarrow$ for circularly left polarizations, respectively), thus modifying the refractive index as

$$n_{\uparrow(\downarrow)} = 1 - (\delta \mp \Delta\delta) + i(\beta \mp \Delta\beta). \tag{1.19}$$

Therefore, the change of the reflected light intensity can be measured and further analyzed. The XMCD effect is especially beneficial for experiments on transition metal or rare earth $L_{2,3}$ and $M_{4,5}$ edges, respectively [125, 126]. Quantitative element and symmetry specific properties of the sample can be extracted from the XMCD data, making it possible to separate spin and orbital magnetic moments. Yet, the extracted data do not provide information on the structural properties. Additionally, the XMCD signal scales with the thickness of the probed element, and in order to extract the thickness independent information it is necessary to measure a thickness series. This technique requires tunable energies, highly circularly polarized x-rays and therefore is only available at synchrotron facilities.

However, recently another synchrotron based technique, x-ray resonant magnetic reflectivity (XRMR) has been proven to be more advantageous over XMCD in magnetic depth profile studies [127–129]. Moreover, it has been shown by XRMR measurements that the MPE is mostly independent from the Pt [130] as well as FM thickness [131]. In addition, the strength of the MPE increases linearly with the FM moment [132, 133] and can be manipulated by the use of a Ta buffer layer [134]. The XRMR measurement technique and the fitting procedure of the experimental data will be discussed in more detail in Chapter 2.

CHAPTER 2

EXPERIMENTAL METHODS

In this chapter, the details of various techniques used throughout the work are discussed.

Magnetization measurements were performed using a 7 T Cryogen Free Magnet system with a vibrating sample magnetometer (VSM). The measurements were performed at room temperature and with in-plane magnetic fields. Additional information on saturation, anisotropy and coercivity fields were obtained from magneto-optic Kerr effect (MOKE) measurements, performed in the magnetic field range up to 2 T.

2.1 Fabrication of sensors

The thin film stacks studied in this work were deposited by magnetron sputtering using a LEYBOLD high vacuum sputtering chamber, with a base pressure of down to 1×10^{-7} mbar. This sputtering tool is equipped with seven sources, onto which single materials, alloys or composite targets can be assembled. All the metallic layers were sputtered using direct current (DC) sputtering, while the MgO layer was produced by radiofrequency (RF) sputtering. In the case of USMR samples, the protective top layer TaO_x was obtained via natural oxidation of a metallic Ta layer at ambient atmosphere.

Figure 2.1 depicts a typical fabrication process, starting from the deposition of a thin films stack (Fig. 2.1(a)). The thin film stacks were further patterned into the desired structures via several steps of lithography, as shown in Fig. 2.1(b) and (d). Both electron beam (e-beam) and optical lithography techniques were used in this work. The samples underwent a set of standard lithography steps: resist coating (photo or e-beam), heat treatment, exposure, and development. The uniform resist coating was obtained by manual dispersion of the resist and subsequent spincoating for 60 s at 4 krpm and 30 s at 5 krpm for optical and e-beam lithography, respectively, resulting in 1 μm and 0.35 μm thick resist. In both cases, a thermal treatment at 100 °C for 4 min (85 °C for 2.5 min for e-beam resist) was necessary.

Depending on the design, non-inverted or inverted masks were used for the lithography. For the optical lithography, non-inverted masks, in combination with a positive

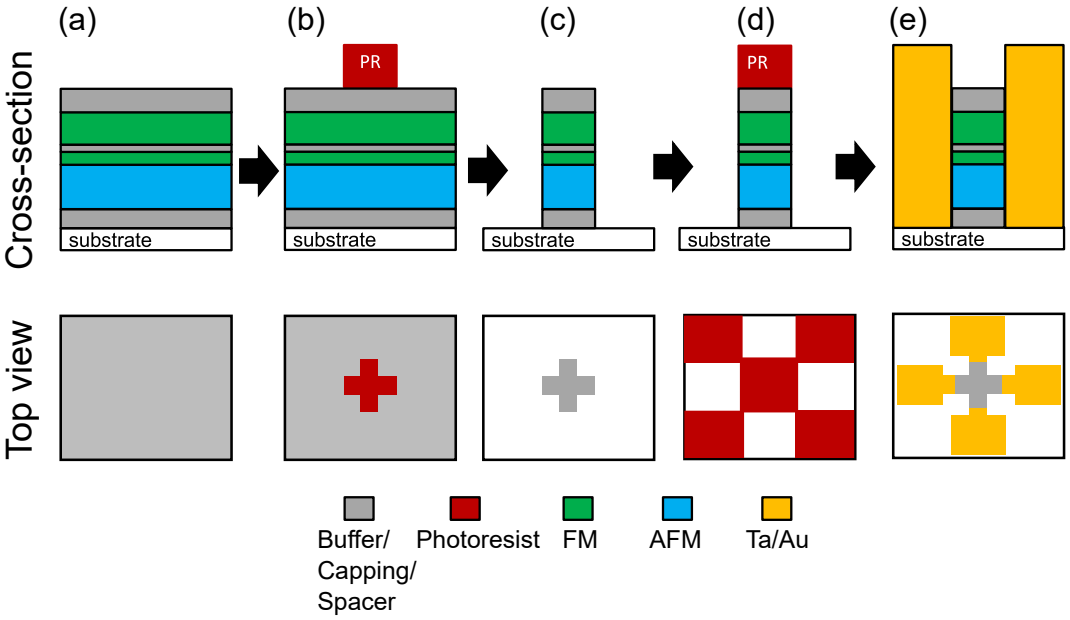

Figure 2.1: Example of the fabrication process of a planar Hall effect sensor with a single Hall cross patterned. (a) Thin films deposition. (b) First lithography to define the sensor. (c) Definition of the sensor via SIMS and consequent resist removal. (d) Second lithography step for the contact pads definition. (e) Deposition of Ta/Au and lift-off.

resist, were utilized for the first lithography step to define the sensor's area, while the inverted masks were used for the definition of the electrical contacts (depicted in Fig. 2.1(d)).

To define the sensor area and remove unwanted material, secondary-ion mass spectrometry (SIMS) was utilized. This technique is a type of dry etching, allowing to remove all the material, not protected by resist, via ion bombarding at an Ar pressure of 2.4×10^{-5} mbar. Here, the sample was rotating during the etching and angled at about 30° with respect to the ion beam. With the implementation of a mass spectrometer, it is possible to precisely control the etching through complex stacks and thus stop the process at the desired layer or substrate.

Finally, most of the samples fabricated within this work include a definition of the Tantalum/Gold contact pads (as depicted in Fig. 2.1(d)). Here, an inverted mask was used in contrast to the sensor definition step (b). After the lithography, the sample areas, which were not covered with resist, were filled with the sputtered Ta 10/Au 80 (thickness in nm), while the rest of the sample was protected by the resist. The contacts were then finally defined via the so-called lift-off process, with unexposed resist being lifted off from the sample, leaving Ta/Au only on exposed areas. The final sensor design is then

shown in Fig. 2.1(e).

In the case of samples used for the detection of magnetic nanoparticles, further fabrication steps were performed, as the deposition of a protective isolating layer and the definition of a microfluidic channel. The isolating layer (20 nm Al_2O_3) for PHE sensors was deposited at IFW (Dresden, DE) by atomic layer deposition (ALD). Selected sensors were then sent to SCRIBA (Bologna, IT) [135] for the microfluidic channel fabrication on top of the sensor. A detailed discussion on the sensors design for magnetic nanoparticles detection will be given in Chapter 3.

2.2 Basics of the lock-in detection

Lock-in detection technique was used extensively within this work for various measurements (PHE effect characterization, USMR and SOTs measurements). This technique allows to detect tiny AC signals, even if the signal of interest is obscured by noise [136, 137]. In order to perform such measurement, lock-in amplifiers are used. Usually, a lock-in amplifier requires a reference signal with a fixed frequency ω_{ref}, generated either by an internal or an external oscillator. The lock-in amplifier multiplies an input signal by the reference and integrates the result over set time, defined as a time constant. For the sinusoidal waves the output response can be written as $V_{sig}\sin(\omega_{ref}t+\theta_{sig})$, with V_{sig} and θ_{sig} being the measured signal amplitude and phase, respectively.

The detected response can be described in the polar format by the magnitude R and phase θ

$$R = \sqrt{(X^2 + Y^2)} = V_{sig}, \tag{2.1}$$

$$\theta = \arctan(\frac{Y}{X}), \tag{2.2}$$

in which X and Y are the outputs in the Cartesian format and are proportional to cosθ and sinθ, respectively. These outputs can be described as follows

$$X = V_{sig}\cos\theta \qquad Y = V_{sig}\sin\theta. \tag{2.3}$$

The output X is typically called an "in-phase" component, while Y is referred to as "quadrature" component.

Usually, the input signal amplitude can be generated as peak-to-peak or rms value. The peak-to-peak values were used for signals generation throughout this work. It is

possible to recalculate peak-to-peak values into rms as follows

$$V_{rms} = \frac{V_{peak-to-peak}}{2\sqrt{2}}. \tag{2.4}$$

The rms signal was used for the calculation of the current density for all the cases, as it describes the average current flowing through a sample.

2.3 Magnetic nanoparticles detection

The PHE sensors developed within this work were characterized utilizing a multi-demodulator lock-in amplifier (Zurich Instruments MFLI-MD). A sensor was stimulated by an alternating current at a frequency f = 767.13 Hz ($\omega = 2\pi f$) and first (1ω) and second (2ω) harmonics of the transverse voltage were then measured, as depicted in Fig. 2.2. This technique gives an advantage for the detection of magnetic nanoparticles,

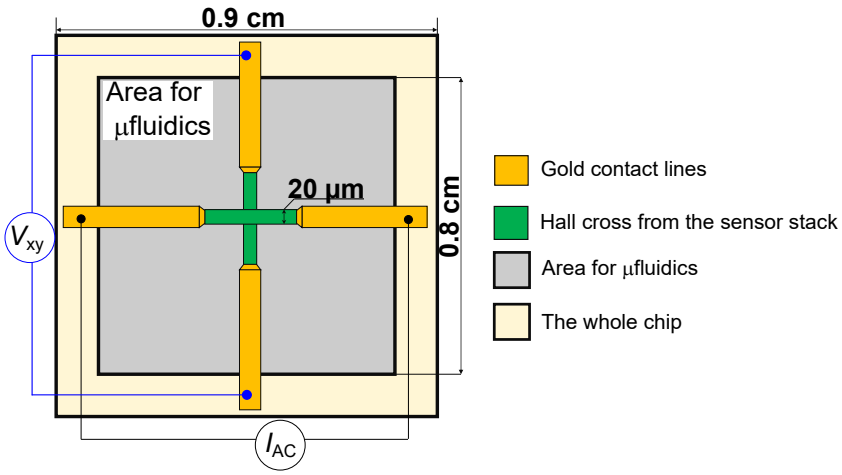

Figure 2.2: Schematic representation of the PHE sensor geometry for the harmonics characterization.

since there is no need in using an external magnetic field in order to magnetize the MNPs. Moreover, the 2ω signal is smaller in comparison to the 1ω or DC response (few μV vs. few mV, respectively), hence it is more sensitive to the small changes of voltage output, associated with the presence of MNPs.

The detection of magnetic nanoparticles is realizable due to the combination of several principles. When an AC current is applied to the sensor, as depicted in Fig. 2.2, it generates an AC magnetic field (Oersted field) in its vicinity. The nanoparticles, being superparamagnetic, become magnetized due to the Oersted field, when they are above the sensor. Consequently, the magnetized nanoparticles possess AC stray fields, which interact with the magnetic field in the sense layer, changing the magnetization of the

sense layer. The transverse voltage, resulting from the planar Hall effect, is proportional to the product of the in-plane magnetization components $m_x \cdot m_y$. The PHE signal has two components, corresponding to the first and second harmonics. The 2ω component is the one sensitive to the MNPs stray fields and changes, when a magnetic particle is present in sensor's vicinity.

The magnetic field of any particle can be described as a function of a distance r between the particle and the sensing layer and can be written according to the Biot-Savart law as follows

$$|\vec{B}(\vec{r})| \sim \frac{m_{MNP}}{r^3}, \tag{2.5}$$

with m_{MNP} being the magnetic moment of the particle.

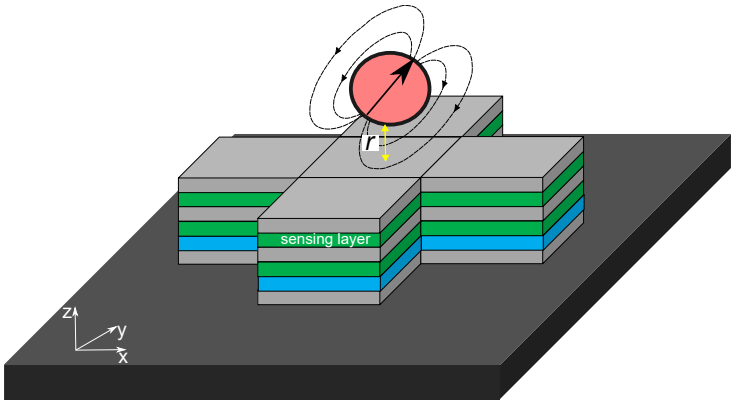

Figure 2.3: A depiction of a magnetic particle with its stray field above a magnetoresistive sensor in a Hall cross design, in which r is a distance between the particle and the sensing layer.

Figure 2.3 shows the case, in which a single particle is located on top of the sensor. For accurate particle detection several requirements must be met:

- Isolation of the structures, to avoid short circuiting, fluid leakage and/or material corrosion.
- The distance r must be as small as possible, according to the Eq. 2.5.
- Ideally, no external magnetic field should be present, as it will saturate the sensor and disturb the detection procedure.
- The sensors must exhibit high sensitivity and low noise.
- The sensors' magnetic field dependence must have a linear-regime at zero field, as well as no hysteresis.

There are several ways to detect MNPs, two of which were used in this work. The first method is static detection, with a drop of a diluted MNP solution placed on top of the sensor with a micropipette. The sensor's output signal was measured before and after the drop placement and then compared, where a change in signal was then associated with the particles.

Another detection method is based on the combination of the magnetoresistive sensor and a microfluidic channel, fabricated directly on top of the sensor allowing controlled flow of the MNP solution, making it a dynamic method. The measurement setup for this case is shown in Fig. 2.4.

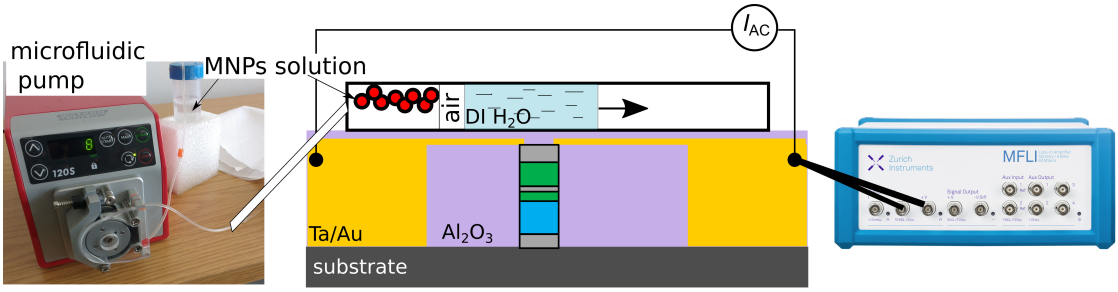

Figure 2.4: Schematic representation of the flow of the magnetic nanoparticles inside the microfluidic channel fabricated on top of the MR sensor. The flow of the MNPs is controlled via a microfluidic pump and the sensor's response signal is then measured by a lock-in amplifier.

Here, a microfluidic pump was used to move the MNP solution within the microfluidic channel. The experiment protocol consisted of several steps, starting with pumping of a reference solution (typically deionized water). After measuring the sensor's response for a certain time with no changes observed, the nanopartcile solution was pumped through the channel. In this case, as depicted in Fig. 2.4, an air bubble was introduced as an interface between the deionized water and the MNP solution. This step allowed for a clear optical distinction between the two solutions and made it possible to precisely define the time, when the MNP solution entered the area above the MR sensor.

2.4 Noise characterization

High quality MR sensors typically exhibit a high signal- to-noise ratio. This can be achieved by either maximizing the MR ratio and/or minimizing the sensor's noise. Therefore, it is of high importance to evaluate noise levels, as it also helps to choose the frequency of injected AC charge current, where the noise is minimal.

The noise characterizations were performed using a multi-demodulator lock-in amplifier (Zurich Instruments MFLI-MD) with the sample placed into a shielding holder (see Fig. 2.5), to minimize the noise from the surroundings. The sensor was stimulated by an AC current and the resulting first (1ω) and second (2ω) harmonics of the Hall voltage response were measured. The frequency sweeps were performed in the range from 1 Hz to 24 kHz at four fixed AC voltage amplitudes. The applied AC voltage amplitudes were chosen in such a way, that the total current density was equal for the Hall crosses of the same size on different substrates. The standard deviation (SD) of the X and Y channels, corresponding to the signal deviation of 1ω and 2ω, respectively, was detected. The SD was then recalculated into the noise S following the relation

$$S = \frac{SD}{\sqrt{ENBW}} \qquad (\frac{V}{\sqrt{Hz}}), \tag{2.6}$$

with ENBW being the equivalent noise bandwidth. A single stage RC filter has an equivalent noise bandwidth of 1/4TC, with TC being the time constant [136]. In this work, the time constant was set to 200 ms and a double stage filter was used (12 dB/oct rolloff) resulting in an ENBW of 625 mHz.

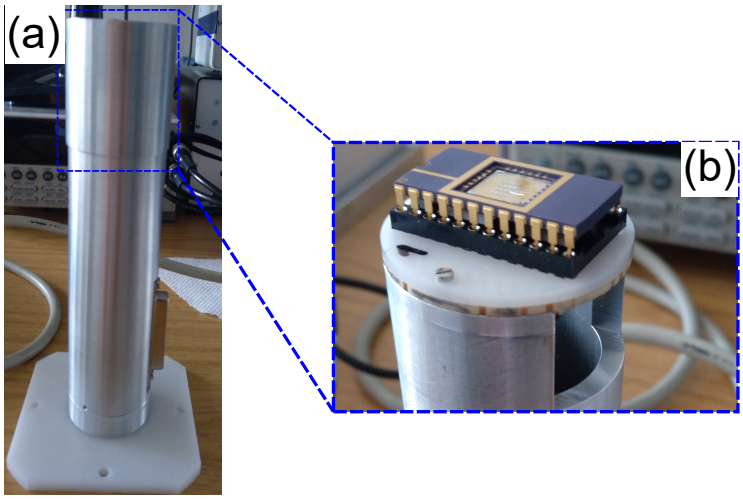

Figure 2.5: (a) Shielding sample holder for noise measurements. (b) Close up of the chip carrier placement with the wirebonded sample.

One of the important parameters to characterize is the setup noise, in this case coming from the lock-in amplifier itself. The device noise depends on the input range [137] and the lowest noise of 2.5 nV/$\sqrt{Hz}$ for frequencies $>$ 1 kHz can be achieved for the input ranges below 30 mV. A number of experiments were performed in order to confirm it and compare to the sample's noise. Figure 2.6 shows the results of such comparison,

in which a black solid line corresponds to the sample's noise, measured separately. It is evident, that for both applied voltages of 1 V (in Fig. 2.6(a)) and 8 V (in Fig. 2.6(b)) the noise of the sample coincide with the noise of the empty lock-in amplifier at the input range of 10 mV. The sharp changes of the noise at 10 Hz for both voltages are attributed to the input signal overload.

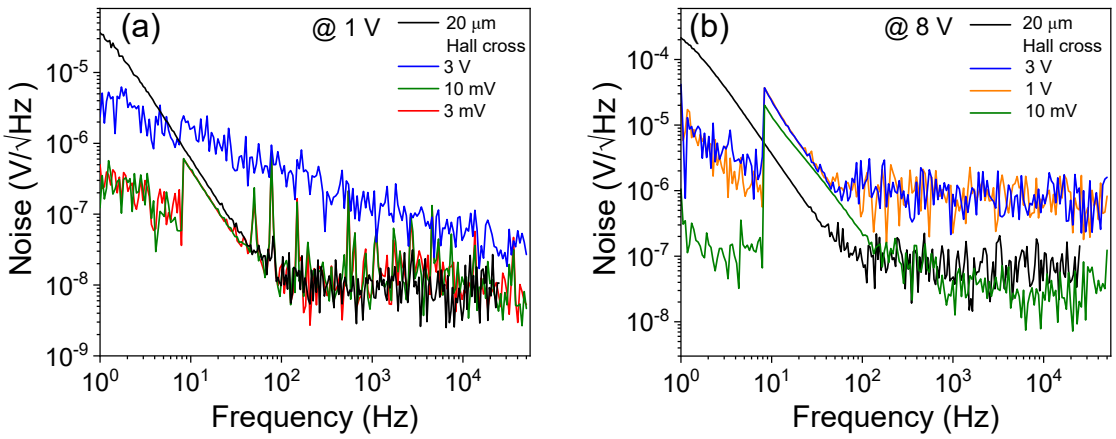

Figure 2.6: Comparison of the MFLI noise levels at various input ranges at the applied AC voltage amplitude of (a) 1 V and (b) 8 V. Black solid line represents noise measured separately for the 20 μm Hall cross.

In Chapter 3 the dependence of the applied voltage and Hall crosses size on the noise amplitude will be discussed in detail. Knowing the noise levels it is then possible to estimate the sensor's detectivity, which corresponds to the smallest detectable magnetic field at a specific frequency. In order to obtain the detectivity of the sensors, sensitivity measurements have to be performed.

2.5 Sensitivity measurements

The sensitivity of a sensor Σ was probed by the direct measurement of an AC magnetic field, generated by a copper bar in vicinity of the sensor's surface (see Fig. 2.7). The AC current was applied to the bar in phase with the sensor's current and generated an AC magnetic field with the same frequency as the sensor's input current. By changing the amplitude of the current sent through the copper bar, it was possible to change the AC magnetic field strength down to mOe range.

Finally, the most important parameter of a sensing device is the detectivity D_B, which gives information on the lowest detectable magnetic field at a given frequency in

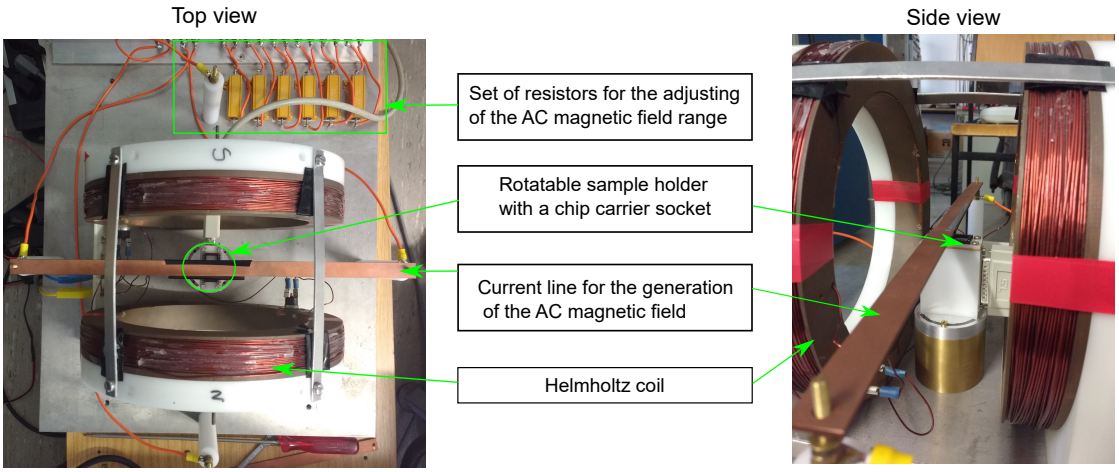

Figure 2.7: Sensitivity measurement setup.

$T/\sqrt{Hz}$. It can be calculated as

$$D_B = \frac{S_{total}}{\Sigma} \quad (\frac{T}{\sqrt{Hz}}), \tag{2.7}$$

with Σ being represented in μV/mT and S_{total} is the total noise, as described in detail in Chapter 1. This step is a crucial part of the sensor characterization, determining the later performance of the sensor in terms of the detection of nanoparticles.

2.6 Harmonic voltage measurement technique

For the USMR and SOT studies, the harmonic voltage measurement technique was used [97, 138], where, unlike for PHE sensors, both longitudinal and transverse first and second harmonics were detected. Here, the measurements were carried out inside a dual Halbach cylinder array with a rotating magnetic field up to 1.0 T (MultiMag, Magnetic Solutions Ltd.). Two Signal Recovery SR7230 lock-in amplifiers, each having two demodulators, were used to simultaneously detect first and second harmonics. The AC current was modulated at a frequency f = 1.176 kHz with the time constant of 200 ms and the RC filter being 24 dB, with the amplitudes between 2.0 and 2.5 mA.

Figure 2.8 represents a measurement geometry of a Hall bar, used for USMR and SOT studies. Here, the width of the Hall bar is $w = 4 - 10$ μm, while the width of the voltage pick up lines was kept constant at $w/3$. The pick up lines were separated by a distance of $5w$, which assures good signal quality and lower noise. Such a Hall bar geometry allows for simultaneous measurements of both, longitudinal and transverse voltages, as depicted in Fig. 2.8 in red and blue, respectively.

When an AC current $I(t) = I_0 \sin(\omega t)$ with constant amplitude I_0 and frequency

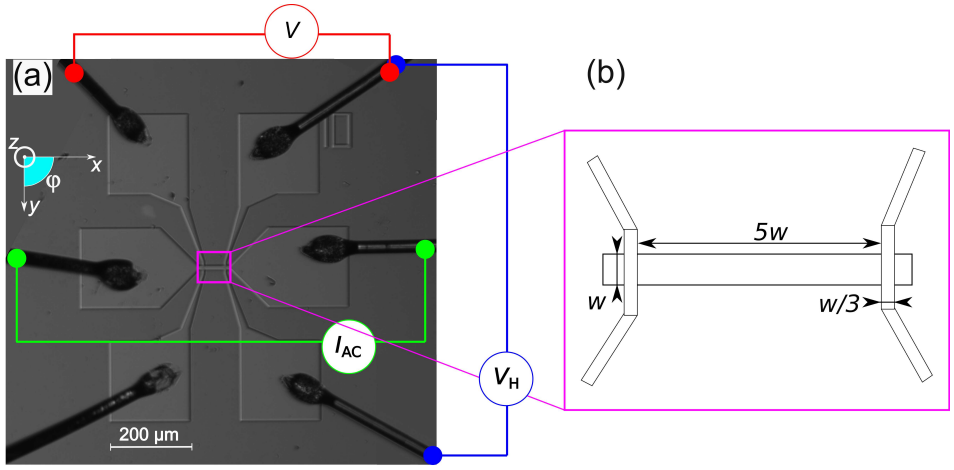

Figure 2.8: (a) An SEM image of a 10 μm Hall bar after wirebonding. The green line represents the AC current injection path, while longitudinal and transverse pick up contacts are shown in red and blue, respectively. (b) A schematic configuration of the Hall bar structure.

$\omega = 2\pi f$ is injected into a system, it results in the emergence of n-harmonic components in such a way, that the total measured voltage can be described as the sum of the voltages of all harmonics

$$V = \sum_n n_i V^i. \tag{2.8}$$

The measured AC voltage can be then described, independently of the measurement geometry, as [97, 138]

$$V(t) = R(t) I_0 \sin(\omega t). \tag{2.9}$$

Several effects of the different origins can be measured by this technique. The first harmonic resistances in longitudinal and transverse geometries are excited via AMR and Hall resistance and read

$$R_\omega = R^z + (R^x - R^z)\sin^2\theta\cos^2\varphi + (R^y - R^z)\sin^2\theta\sin^2\varphi. \tag{2.10}$$

$$R_\omega^H = R_{AHE}\cos\theta + R_{PHE}\sin^2\theta\sin 2\varphi, \tag{2.11}$$

with θ and φ being the polar and azimuthal angles of the magnetization vector $\overrightarrow{M}$, respectively.

The main origins of the second harmonic effects measured in this work are SOTs, thermal and non-linear effects (here USMR). In general, the measured longitudinal and transverse second harmonic resistances can thus be written as [97, 138]

$$R_{2\omega} \propto I_0(R_{2\omega}^{SOT} + R_{2\omega}^{\nabla T} + R_{2\omega}^{USMR}). \tag{2.12}$$

$$R_{2\omega}^{H} \propto I_0(R_{2\omega}^{H,SOT} + R_{2\omega}^{H,\nabla T}). \tag{2.13}$$

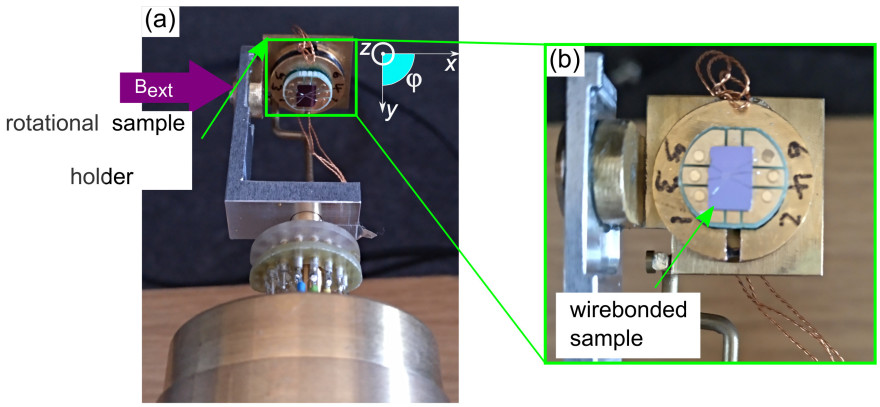

Figure 2.9: The measurement setup used for the SOTs and USMR characterizations. (a) A rotational sample holder (highlighted in green). The sample holder is typically covered with a cylinder and placed inside a rotational magnetic field. (b) A close-up of the wirebonded sample placed in the sample holder. The sample can be rotated freely in-plane and out-of-plane.

The measurement setup is shown in Fig. 2.9. In Fig. 2.10, the main effects measured for each harmonic and geometry are presented. As was shown by Eqs. (2.10) - (2.13), the 2ω resistances are a sum of different effects. Additionally, Fig. 2.10 gives information on the angular dependence of the effects, for the measurements performed in the xy plane, hence varying the angle φ between 0° and 360° (as shown in Fig. 2.9).

In order to extract the information on USMR and SOTs, the separation of the effects must be performed. As was shown by Avci *et al.* [139], by measuring the angular dependence in the xy plane for various applied magnetic fields, one can extract the resistance originating from the thermal gradient due to the Joule heating, thus identifying $R_{2\omega}^{H,\nabla T}$. As it can be seen from the Eq. (2.13), $R_{2\omega}^{H}$ consists of two components with distinct angular dependencies. While the FL SOT is proportional to $(2\cos^3\varphi - \cos\varphi)$, the DL component is proportional to $\cos\varphi$. At the same time, the effects originating from the thermal gradients (here mainly out-of-plane gradient), like the spin Seebeck effect (SSE) and the anomalous Nernst effect (ANE) follow a $\cos\varphi$ angular dependence. Additionally, magnetic thermopower effect (AMTP) may occur with the $\cos 2\varphi$ angular dependence. It must be noted, that the thermal contributions may also occur in the lon-

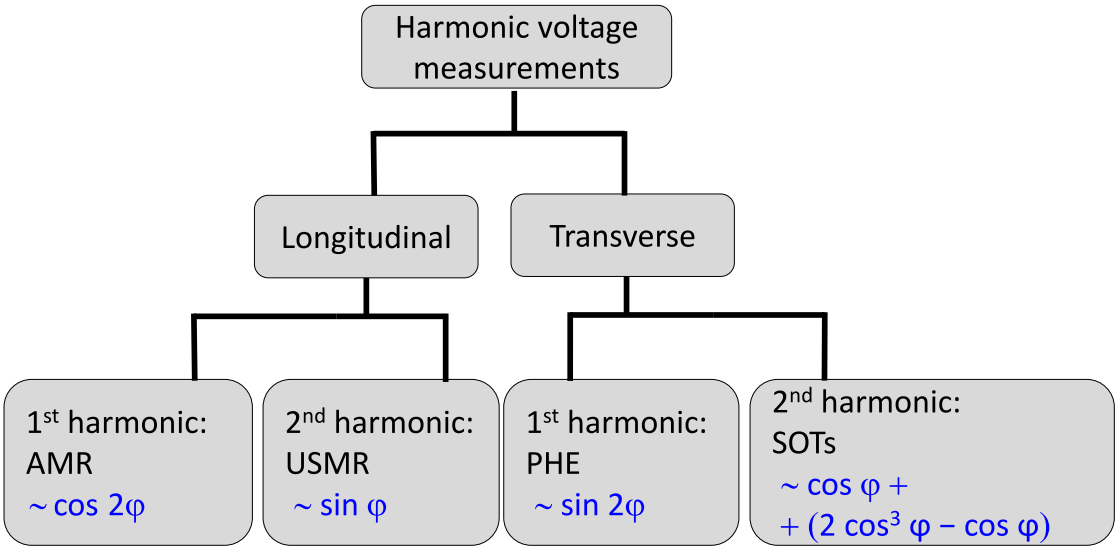

Figure 2.10: Harmonic longitudinal and transverse voltage measurements scheme. Angular dependencies for each effect represented in blue.

gitudinal resistance and end up in a sin φ dependence. Thus, by fitting the raw data with a sum of these functions, it is possible to extract the corresponding effects.

Avci *et al.* [139] discussed a technique for separating the thermal effect and DL SOT, which have the same $\cos\varphi$ angular dependence. Here, the amplitude of the $\cos\varphi$ fit function is plotted as a function of the inverse total magnetic field $\frac{1}{B_{total}}$, in which B_{total} is a sum of the external applied magnetic field, anisotropy and demagnetizing fields, $B_{total} = B_{ext} + B_{demag} - B_{anis}$. It is expected that the thermally induced effects do not depend on the external magnetic field and are constant, while the DL SOT changes with the applied external magnetic field. Hence, by linearly fitting the data, it is possible to extract the $R_{2\omega}^{H,\nabla T}$ as an intersection with the y-axis.

Similarly, the amplitude of the USMR effect can be expressed as

$$R_{2\omega}^{USMR} = R_{2\omega} - R_{2\omega}^{\nabla T}. \tag{2.14}$$

Here, it is important to note that the temperature effects in longitudinal and transverse geometries are differently scaled and can be converted by $R_{2\omega}^{H,\nabla T} = \frac{l}{w} R_{2\omega}^{\nabla T}$, with l and w being the separation between the voltage pick up contacts and Hall bar width, respectively (see Fig. 2.8). A more detailed discussion on the separation of the different effects can be found in the Chapter 4.

2.7 X-ray reflectivity

In order to determine the thickness and roughness of the layers in various samples, x-ray reflectivity (XRR) was used. Here, XRR was performed utilizing a Philips X'Pert Pro MPD x-ray diffractometer tool with Cu K_α radiation, corresponding to the wavelength of λ = 1.5419 Å and energy of E = 8041 eV. The measurements were done in Bragg - Brentano $\theta - 2\theta$ geometry.

The typical $\theta - 2\theta$ geometry for XRR is presented in Fig. 2.12. Here, the incident x-rays shine onto a sample. Part of the radiation is reflected, while another part is absorbed. The refractive index of a material can thus be written [140, 141] as

$$n = 1 - \delta + i\beta, \tag{2.15}$$

in which δ and β are the dispersion and absorption, respectively, and can be represented as

$$\delta = \frac{\lambda^2}{2\pi} r_e \rho, \tag{2.16}$$

$$\beta = \frac{\lambda}{4\pi} \mu, \tag{2.17}$$

in which r_e is the electron Lorentz classical radius (2.818×10^{-15} m), μ is the coefficient of attenuation and ρ is the density. When the incident angle θ is smaller than the critical

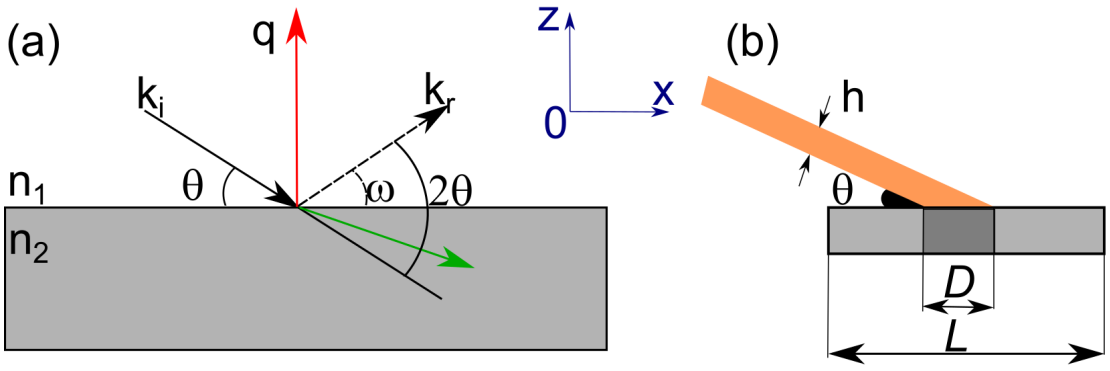

Figure 2.11: (a) XRR $\theta - 2\theta$ geometry, with k_i and k_r being the vectors of the incident and reflected x-rays, respectively, with q=k_r-k_i being the scattering vector. (b) Geometrical footprint correction, with h being the beam width, D is the illuminated area of the sample and L is the total sample length.

angle θ_c, total external reflection is observed, which means that all incoming x-rays are reflected (not taking any evanescent x-rays into account). The critical angle θ_c scales with the electron density $\theta_c \propto \sqrt{\rho_e}$, and is typically below 1°, for example $\theta_c = 0.424°$ for Ni and $\theta_c = 0.57°$ for Au [140].

When an incident angle is larger than the critical angle, the intensity of the reflected x-rays decays proportional to q^4. If the sample is a thin film system, the intensity oscillates with a characteristic period while decaying due to interference at the thin film interfaces. These oscillations were first described by H. Kiessig [142] and are called Kiessig fringes. From the oscillation period the film thickness can be derived as

$$d = \frac{2\pi}{\Delta q_z} \approx \frac{\lambda}{\Delta 2\theta}, \tag{2.18}$$

with $q_z = \frac{4\pi}{\lambda} \sin\theta$. In case of relatively small angles ($\theta < 5°$), it can be assumed that $2\Delta \sin\theta \approx \Delta 2\theta$ with $\Delta 2\theta$ being the oscillation period.

The size of the beam is a major parameter, as the starting angle of the XRR measurements is usually below the critical angle of the external reflection. Typically, the XRR measurements conditions are such that due to the finite beam width only a part of a sample is illuminated, as depicted in Fig. 2.12(b). Here, the x-ray beam with width h shines at a sample at the angle θ, thus illuminating only the area D out of the whole sample length L. Therefore, it is necessary to perform the so-called footprint correction, in which the footprint of the beam on the surface of the sample along the beam direction is

$$D = \frac{h}{\sin\theta}. \tag{2.19}$$

Hence, the angle θ_{fp}, at which the footprint length coincides with the sample's length can be calculated as

$$\theta_{fp} = \arcsin(\frac{h}{L}). \tag{2.20}$$

Finally, using the recursive Parratt algorithm [143], it is possible to fit the experimental data with the simulated reflectivity curve. Thus, when the fitted curve is such that it describes the experimental data, the thickness of the layers as well as roughness and density can be extracted. In this work, GenX [144] and ReMagX [145] software tools were used to simulate the XRR curves and to extract the structural parameters.

XRR is a powerful and reliable technique for the determination of the structural parameters with high precision. By adding a magnetic field into the measurement setup and using circularly polarized x-rays, not only the structural parameters space, but additional magnetism-related parameters can be probed.

2.8 X-ray resonant magnetic reflectivity

In order to access the depth profile of an induced magnetization, x-ray resonant magnetic reflectivity, a synchrotron-based measurement technique, was used. The XRMR

measurements were performed at the resonant scattering and diffraction beamline P09 [146] at the third generation PETRA III synchrotron facility at DESY (Hamburg, Germany). The beamline allows to execute measurements at room and low temperatures, in vacuum as well as in ambient atmosphere, with an available energy range of 2.7 to 50 keV.

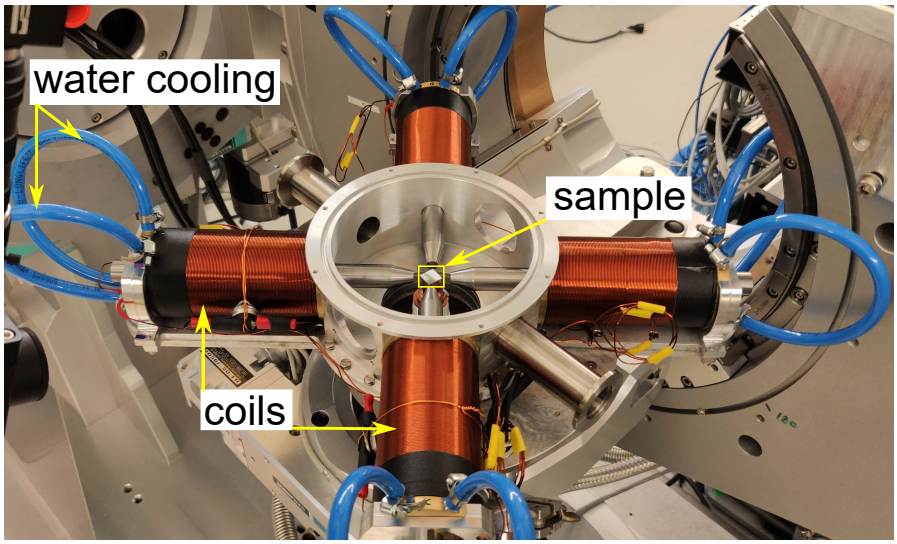

Figure 2.12: XRMR setup at P09 beamline at DESY. A four coil vector electromagnet with adjustable distance and integrated water cooling.

For investigation of the MPE in bi- and trilayers containing Pt, the XRMR measurements were carried out at the Pt L_3 absorption edge with a photon energy of 11566.5 eV (corresponding to the wavelength λ = 1.07192 Å). The resonant XRR curves were measured in θ - 2θ scattering geometry using circularly polarized x-rays. The degree of circular polarization of x-rays was 99 $\pm$ 1 %. An external magnetic field ($\pm$ 90 mT) was applied in the scattering plane parallel to the sample surface. The reflected intensity was detected, where for each scan the helicity of the circularly polarized x-rays was kept fixed, while the magnetic field direction was alternated. The measurement setup with the four coil vector electromagnet is shown in Fig. 2.12. The distance between the poles is adjustable, so samples of various sizes can fit. The magnetic field strength can be adjusted by varying the applied coil current.

It was shown by Kuschel *et al.* using *ab initio* calculations for Pt L_3 edge, that $\Delta\delta \approx 0$ and $\Delta\beta$ is at maximum at 1 eV below the whiteline of the Pt L_3 absorption edge [130]. Based on this finding, an x-ray absorption spectrum (XAS) was taken prior to the reflectivity curves, in order to precisely determine the resonance energy of each sample and thus to be able to set the measurement energy 1 eV below the corresponding L_3 absorption edge. The calculated $\Delta\beta$ profile was further used in this work to relate

the depth profile, obtained by XRMR, to the final magnetic moment values per Pt atom.

The non-magnetic reflectivity was obtained by averaging the two curves, measured with circularly left and right polarized x-rays, and is defined as $I = \frac{I_+ + I_-}{2}$, with I_+ and I_- corresponding to the XRR intensity at positive and negative magnetic fields, respectively. The XRMR asymmetry ratio is defined as $\Delta I = \frac{I_+ - I_-}{I_+ + I_-}$.

In the case of simple bilayers, such as Fe/Pt, in which no oxidization or marginally interdiffusion states between the layers is expected, the fitting procedure is rather straightforward as described by Klewe *et al.* [132]. However, when the samples under study consist of multilayered thin films, with a complex oxide capping layer, more unknown parameters must be added into the simulation, hence complicating the analysis procedure. Therefore, the advanced analysis procedure was used in this work, as described in detail by Krieft *et al.* [147].

For the analysis of the obtained data, first the averaged resonant XRR curves were fitted, utilizing the recursive Parratt algorithm [143] and ReMagX software [145]. In the simulations the stack is represented as a list of layers corresponding to different compounds within the so-called layer mode. The roughness is modeled with the matrix formalism, utilizing the layer segmentation approximation of the ReMagX tool. The extracted information on the thicknesses of the layers as well as roughness is later used for the asymmetry ratio fitting.

The asymmetry ratio was modeled with the Zak matrix formalism [148], in which the additional magnetic contribution is simulated by a convolution of a Gaussian spin polarization depth profile with the interface roughness at the Co/Pt interface resulting in a Gaussian-like magnetic Pt depth profile. The goodness of fit (χ^2) is defined as the sum of the squared error, logarithmically weighted for XRR and linearly for XRMR. It represents the differences between the experimental and simulated reflectivity curves and asymmetry ratios. The maximum value of $\Delta\beta$ and the effective thickness of the spin-polarized layer, defined as full width at half maximum (FWHM) of the Gaussian-like profile, were then extracted.

CHAPTER 3

ULTRASENSITIVE SENSORS FOR MAGNETIC PARTICLES DETECTION

This chapter reports on the development and characterization of ultrasensitive magnetoresistive sensors for Alzheimer's and Parkinson's diseases early detection within the EU HORIZON 2020 MADIA project.

The sensors developed in this work were further used as a corner stone of a diagnostic platform, where the main working principle lies in the detection of magnetic nanoparticles by MR sensors. The results obtained on magnetic nanoparticles detection at various stages of the project were mostly obtained from the joint work between MADIA project partners: CNR-Lecce, SCRIBA and CNR-Bologna.

The work presented here was done in the close collaboration with Luca Marnitz, who participated in MADIA project from the Bielefeld University side as well. The corresponding references to his work are placed accordingly.

Parts of the results reported within this chapter were presented at the IEEE MagFrontiers conference, spring meeting of DPG-2019, as well as various project reports. Some of the results are also a part of the peer-reviewed article A. Elzwawy, H. Pişkin, N. Akdoğan, M. Volmer, G. Reiss, L. Marnitz, **A. Moskaltsova**, O. Gurel, and J.-M. Schmalhorst, "Current trends in planar Hall effect sensors: evolution, optimization, and applications", J. Phys. D **54**, 353002 (2021) [149] and a book sub-chapter: G. Reiss, L. Marnitz, **A. Moskaltsova**, and J.-M. Schmalhorst "Magnetic biosensors" in "Nanomagnetic Materials Fabrication, Characterization and Application" [150].

Finally, the method of the thin films stack compensation has been jointly developed and a German patent was issued on 11.02.2021 "Vorrichtung und Verfahren zum Detektieren von magnetischen Partikeln" [151].

3.1 Optimization of the magnetoresistive sensors sensitivity

In the frame of MADIA project three types of magnetoresistive sensors were studied as potential candidates for the final application, which are PHE, GMR and TMR sensors. Each of them has advantages and drawbacks. This section is focused on comparison

between the sensors of various types.

3.1.1 Tunneling magnetoresistance effect sensors

Tunneling magnetoresistance sensors are known for their extremely high sensitivity. However, their fabrication process is rather complex, as it requires state-of-the-art sputtering facilities to deposit high quality ultrathin MgO barriers, which is the corner stone of the highly sensitive TMR sensor. Additionally, three steps of lithography are usually necessary to define bottom and top electrodes, as well as to deposit protective oxide layer, in order to achieve the electrical transport via the tunnel barrier only.

For the purpose of being able to answer the question whether the TMR sensors are good candidates for the MADIA project needs, the main focus was put into magnetic and electrical characterization of an already optimized stack design. The samples were grown via magnetron sputtering deposition as described in Chapter 2. The details on the stack growth and optimization can be found elsewhere [152, 153].

Figure 3.1(a) shows a DC magnetic field loop of a typical TMR sensor with a MTJ pillar size of (22.5 $\times$ 22.5) μm^2. The loop was obtained by applying an AC current of 10 mA at the modulation frequency of 88.3 Hz and the first harmonic of the signal was then detected. The inset in Fig. 3.1(a) gives information on the TMR stack, where the buffer consists of Ta 5/Ru 30/Ta 10/Ru 5 (thickness in nm) and capping is made of Ta 2/Ru 2.

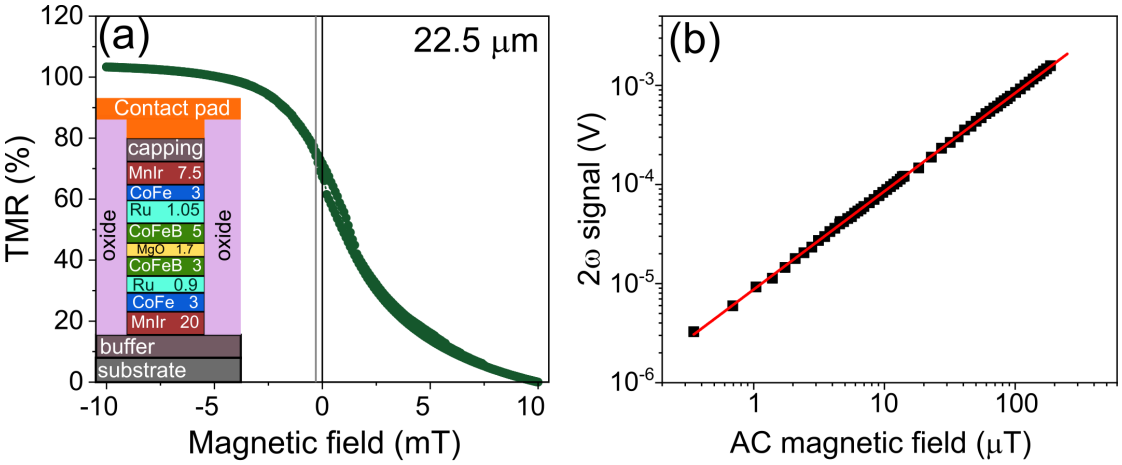

Figure 3.1: (a) Hysteresis field loop for a MTJ pillar with (22.5 $\times$ 22.5) μm^2 size. The inset depicts the thin films stack with thickness given in nm. (b) Second harmonic signal corresponding to directly measured sensitivity of the MTJ. The sensor was supplied with 10 mA AC current at 88.3 Hz.

The TMR stack contains two synthetic antiferromagnets (SAF) comprised of MnIr

20/CoFe 3/Ru 0.9/CoFeB 3 (bottom layer) and CoFeB 5/Ru 1.05/CoFe 3/MnIr 7.5 (top layer). The Ru interlayers on both sides are responsible for the RKKY coupling between the two FMs. The 5 nm CoFeB layer above the tunnel barrier is the sensing layer and it is weakly coupled, while the bottom 3 nm CoFeB layer acts as a reference layer and the coupling is set to be very strong [152]. In order to achieve the desired coupling, the blank TMR films were annealed twice at different temperatures and magnetic field orientation. The first annealing step was performed at 360 °C for 60 min. The consequent annealing step was then implemented at 260 °C for 30 min and the direction of the magnetic field was perpendicular to the first annealing, so a crossed magnetizations state was achieved (more details can be found here [152]). The maximum TMR ratio measured for this sensor was 103 % with a sensitivity at near zero magnetic field of 15.3 %/mT. Although, small hysteresis is observed at zero field, it is possible to overcome this issue by applying a small DC offset field of -0.3 mT during sensitivity measurements, where no hysteresis is observed, as indicated by a grey vertical line in Fig. 3.1(a).

The main effort in the investigation of TMR sensors was put into direct sensitivity measurements, where the conditions of the magnetic nanoparticles above the sensor were simulated by sending an AC current through a copper bar above the sensor, which generated an AC magnetic field. By adjusting the distance between the bar and the sensor's surface, as well as varying the AC current amplitude, it was possible to access the information on the detection limits of the TMR sensor. More details on the sensitivity measurement setup are given in Chapter 2.

Finally, Fig. 3.1(b) depicts the resulting sensitivity as a change of the second harmonic (2ω) signal, which emerges only when an AC current is sent through the sensor, in-phase and with the same frequency as the AC magnetic field in the copper bar. As mentioned previously, due to the hysteretic behavior of the magnetization switching at zero magnetic field, a constant DC offset field of -0.3 mT was applied during both sensitivity experiments. As was determined from these measurements, the lowest detectable magnetic field in the second harmonic is in the few μT range, which makes this TMR sensor a great candidate for the MNPs detection application. However, it must be mentioned, that the TMR sensor, as shown here, is a CPP-type and hence it requires a top electrode, which typically consists of Ta 10 nm/Au 80 nm layers. Hence, the distance between the sensing layer (CoFe 3) and sensor's surface, where a magnetic nanoparticle can be measured, is rather large and estimated to be at least 110 nm. Another challenging fact is that a way to magnetize the magnetic nanoparticles, without saturating or disturbing the magnetization state of the sensor, still has to be developed.

3.1.2 Giant magnetoresistance effect sensors

Another type of MR sensors, studied within this work, were GMR sensors. Unlike TMR, GMR sensors typically exhibit lower MR ratios and, as a result, lower sensitivities. Nevertheless, these sensors are robust and easier in production, as they do not require ultrathin barrier deposition and various complex lithography steps.

Three GMR stacks were investigated within this thesis: Si/SiO_2/Ta 5/Pt 8/Co 3/Cu *t*/Co 2.5/Ta 2 (stack A) and Si/SiO_2/$Ni_{81}Fe_{19}$ 5/MnIr 10/Co 3/Ru 0.9/Co 3/Cu 2.1/Co 3/Ru 5 (stack B) and finally Si/SiO_2/$Ni_{81}Fe_{19}$ 5/Ta 10/Co 3/Cu 2.1/Co 0.5/$Ni_{81}Fe_{19}$ 2.5/Ta 2 (stack C), in which $Ni_{81}Fe_{19}$ is Permalloy (Py). All thicknesses are indicated in nm. In the case of the stack A, there are two ferromagnetic Co layers, separated via a non-magnetic Cu layer, while the remaining Ta layers serve as buffer and capping. The Cu interlayer promotes the RKKY coupling between the two FMs. The thickness of Cu layer t was varied between 1.8 to 2.2 nm with 1 Å step, since the strength of RKKY coupling, as well as its type (ferromagnetic or antiferromagnetic) depends on the thickness of the NM layer, as discussed in Chapter 1. It is known for Cu, that the first antiferromagnetic coupling maximum (AFCM) is at 0.9 nm, while the second AFCM is at 1.8 nm [154]. However, due to high sputtering rates of Cu (≈0.94 nm/s at 115 W), there is a large uncertainty, when depositing 0.9 nm Cu to hit the first AFCM. Hence, in the case of the stack A, the Cu thickness was varied around the second AFCM. Figure 3.2(a) shows the GMR curves for various Cu thicknesses.

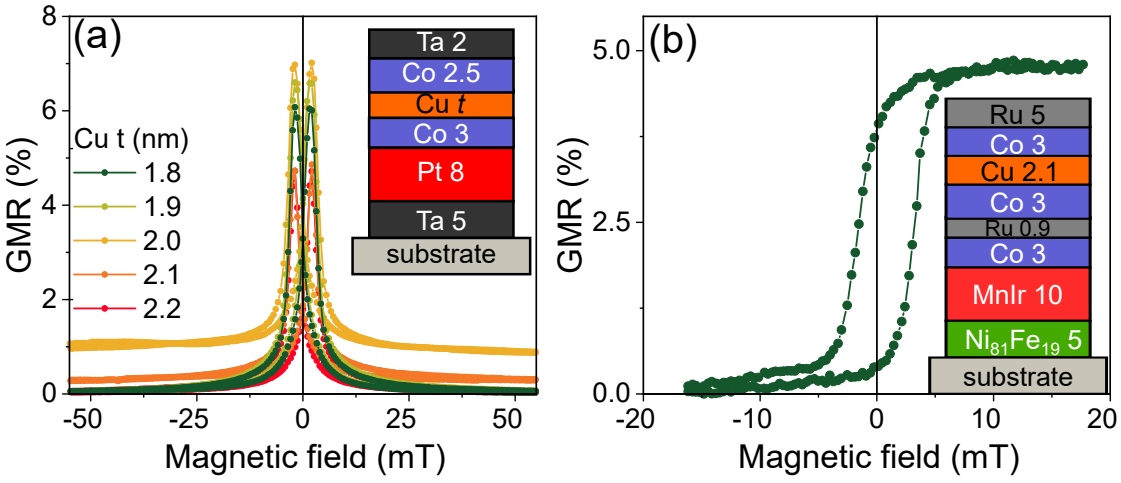

Figure 3.2: (a) Hysteresis loops for the GMR stack A with various Cu thicknesses t. The maximum GMR effect of 6.8% was obtained for the Cu thickness of 2.0 nm. The inset depicts the thin films stack. (b) A hysteresis loop of the GMR stack B. The inset shows the full thin films structure. The maximum GMR of 5% was measured.

For the case of the stack B, a SAF structure was introduced, as shown in the inset in Fig. 3.2(b). In comparison to the stack A, here three FM layers are present, with the combination of Co 3/Ru 0.9/Co 3 being the SAF, with the bottom Co layer pinned antiferromagnetically by the underlying MnIr. Such a structure, however, requires a magnetic annealing, which for this stack was performed at 260 °C for 60 min. Thus, the resulting mechanism fixes the magnetization direction of the second FM layer, allowing the top FM to rotate freely in the presence of magnetic field, making the top Co 3 nm the sensing layer. The thin Ru interlayer enables RKKY coupling between the two Co layers. The thickness of 0.9 nm was chosen to match the first AFCM [50]. The use of Ru instead of Cu allows to control the deposition rate more precisely, thus resulting in a better quality of the film.

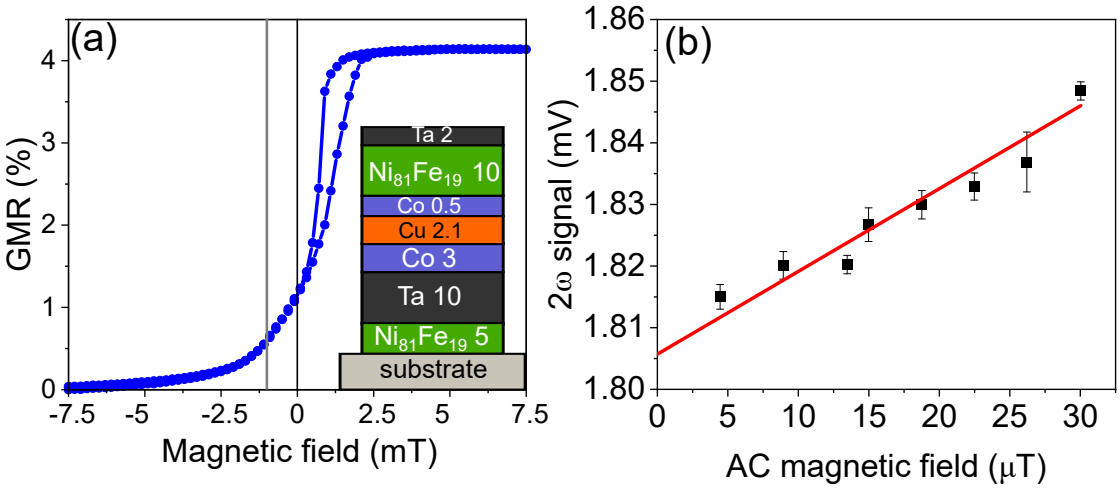

Figure 3.3: (a) GMR hysteresis loop measured applying a DC current of 1 mA. The inset is a schematic representation of the thin film stack. A DC offset field of -1 mT was applied (marked with a grey vertical line) to ensure a hysteresis-free linear behavior for the sensitivity measurements. (b) Sensitivity of the patterned GMR sensor with 1 mA AC current at 88.3 Hz.

Figure 3.3(a) demonstrates the GMR curve of the stack C, depicted in the inset. The maximum GMR achieved for this sample is 4.8%. Among all the three stacks, only stack C exhibits a linear hysteresis-free behavior near zero field, with the maximum sensitivity at -1 mT. Hence, the DC offset field of -1 mT was applied during the sensitivity measurements. This stack was further patterned and used for the sensitivity measurements. Furthermore, Fig. 3.4 represents the final design of the GMR sensor, proposed for the incorporation with the microfluidic channel, where arrays of GMR sensors are patterned. As one can see in Fig. 3.4(b), the GMR sensor is patterned into a form of a meander and two sensors share one current line, which allows to have a reference signal,

when one of the meanders does not lay under the microfluidic channel. The direction of the easy axis is along the meander. The easy axis direction was set during the annealing step. As the GMR effect is usually strongly dependent on the temperature, it is essential to have a good control of the experiment.

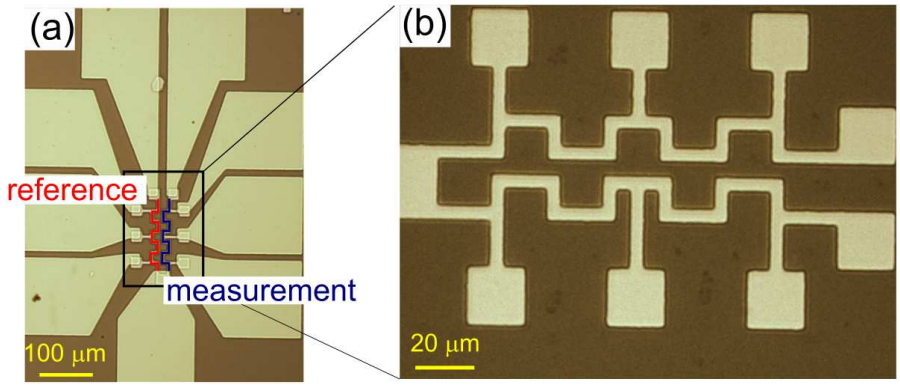

Figure 3.4: (a) Single GMR element, with reference and measurement channels highlighted in red and blue, respectively. (b) An enlarged view of the sensing channels, rotated 90 °.

Overall, various GMR stacks were developed within this work, where all of them exhibit an average GMR ratio between 4.8 and 6.8 %. Yet, only one stack was chosen for the further MNPs detection experiments, with almost no hysteresis in the linear range. All of the GMR stacks discussed here got only 2-5 nm capping layers and no contact electrodes on top. Therefore, the distance between the sensing FM layer to particles is rather low compared to the previously described TMR stack. However, one important question regarding the particles magnetization remains. In principle, it is possible to use current lines to produce Oersted fields, strong enough to magnetize the MNPs, but this required a lot of optimization and development time, which was not available within the project.

3.1.3 Planar Hall effect sensors

In parallel, planar Hall effect sensors were developed and investigated as potential candidates for the final MADIA sensors. The development of various stacks and their properties are described in more details elsewhere [155, 156]. The final PHE stack developed within the scope of MADIA project is as follows: substrate/Ru 3/MnIr 10/$Ni_{81}Fe_{19}$ 4/Ru 1.7/$Ni_{81}Fe_{19}$ 10/Ru 5.6, with the top $Ni_{81}Fe_{19}$ layer being the sensing layer. The stack is schematically depicted in the inset in Fig. 3.6(a). The antiferromagnetic MnIr layer, as in the case of the above discussed TMR stack, pins the magnetization state of the 4 nm thick Py layer above it, thus making it the reference layer. The

thin 1.7 nm Ru layer promotes the RKKY coupling between the two ferromagnets, so the sense layer is weakly ferromagnetically coupled to the bottom pinned Permalloy. The hysteresis loops for the 1ω and 2ω harmonic signals are presented in Fig. 3.6(a). The 2ω signal, shown in red circles, follows an expected shape of $\partial V^{1\omega}/\partial B$ and is highly sensitive at zero field. Finally, the thickness of the topmost Ru was optimized in such a way, that the resulting signal-to-current ratio is as small as possible, ideally zero. In order to find the optimal thickness, a series of thin film stacks were prepared with varying Ru thickness in the range from 5.3 to 6 nm in 1 Å steps. The Ru thickness of 5.6 nm yielded the minimum signal-to-current ratio, and thus was used for all the future samples (see Fig. 3.6(b)). The findings of this work on the Ru thickness optimization served as the basis for a German patent application [151].

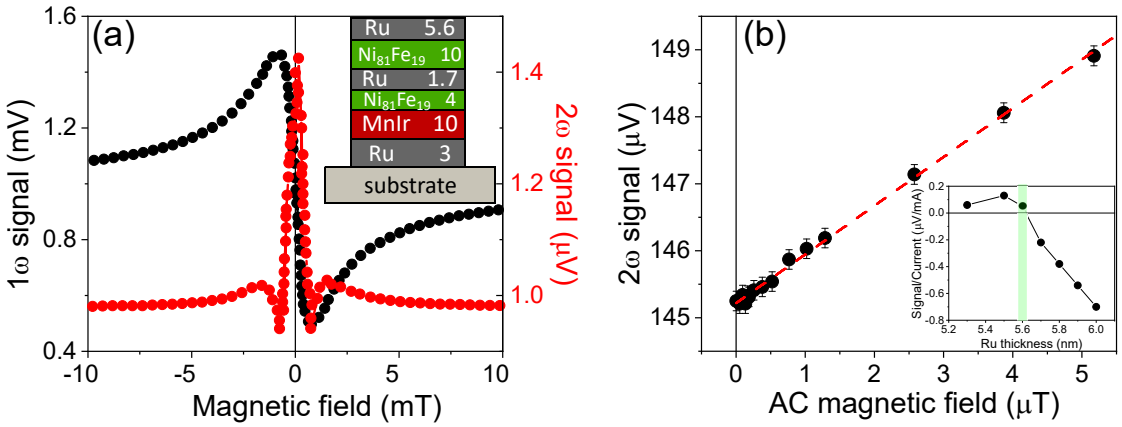

Figure 3.5: (a) Hysteresis loops for the first (in black) and second (in red) harmonics. Inset in (a) depicts the thin films stack. (b) PHE sensitivity. A minimum magnetic field that can be detected is down to 0.1 μT. Inset in (b) shows the dependence of the signal-to-current ratio on the Ru thickness. The optimal thickness of 5.6 nm is highlighted in green.

As can be observed from the Fig. 3.6(b), the resulting sensitivity achieved for the optimized sensor stack is about 0.1 μT, which makes PHE sensors the perfect candidate for magnetic nanoparticles detection application within the MADIA project.

A comparison between the different MR sensor types, which were investigated within this work, is shown in Table 3.1. Although, sensitivity is typically the main criteria for a sensor, here it was also important to evaluate the distance between the sensing layer and a magnetic particle, as well as to consider the fabrication complexity (see column "N. litho steps"). Another paramount property, not shown in Table 3.1, is the possibility to magnetize MNPs without disturbing the magnetic state of the sensor. The PHE sensors developed here, allow to magnetize the MNPs by using the sensors' Oersted field, generated in the stack layers, without a need for an external field. This

Table 3.1: A summary of evaluation of various MR sensors

type	production cost	N. litho steps	sensitivity	max MR %	robustness	distance to particles
TMR	high	3	15.3%/mT	103	low	>110 nm
GMR	moderate	2	0.57%/mT	5	moderate	∼20 nm
PHE	low/moderate	1-2	200 μV/mT	-	high	∼20 nm

is, however, not the case for TMR and GMR sensors. Both sensor types would require a special solution, in order to be able to magnetize the MNPs, without disturbing the magnetic state of the sensor and thus changing its sensitivity. Hence, it was decided to put all the efforts into the further development of the PHE sensors and their final implementation into the multidisciplinary platform for the early diagnosis of Alzheimer's and Parkinson's diseases.

3.2 Magnetic nanoparticles detection

The magnetic nanoparticles utilized at all stages of the work were superparamagnetic iron oxide (Fe_3O_4) nanoparticles produced by the MADIA project partner University of Santiago de Compostela. The MNPs were typically coated with a protective shell, for example silica and magnetic core diameters were different at various stages of this work, ranging between 20 nm to 150 nm. The details on the fabrication of the MNPs and their properties can be found elsewhere [157, 158].

The first experiments on the detection of magnetic nanoparticles were conducted using both GMR and PHE sensors with MG-105 nanoparticles (20 nm Fe_3O_4 coated in silica). These experiments were the initial tests to assess the overall detection principle and were performed without a microfluidic channel on top of the sensors. Instead, a 0.1 μl sized drop of a solution with diluted MNPs was placed on top of a sensing area. The experiment protocol was as following: 1 min shaking of the diluted MNPs solution followed by 1 min of ultrasonic bath and finally another shaking step for 15 s. Magnetic DC field loops were recorded right before the MNPs placement to serve as a reference signal, and immediately after the placement, to observe any difference in the shape of the loops, which is attributed to the presence of the MNPs.

Figure 3.6 reports the results of such static MNPs detection by means of GMR sensor (Fig.3.6(a) and (c)) and PHE sensor (Fig.3.6(b) and (d)). It is evident, that for the case of the GMR detection, a slight change of the signal is present, which is attributed to the MNPs presence. The microscope image shown in Fig.3.6(a) demonstrates the outer ring of the MNPs drop and that the ring's edge lays exactly on top of the sensing area

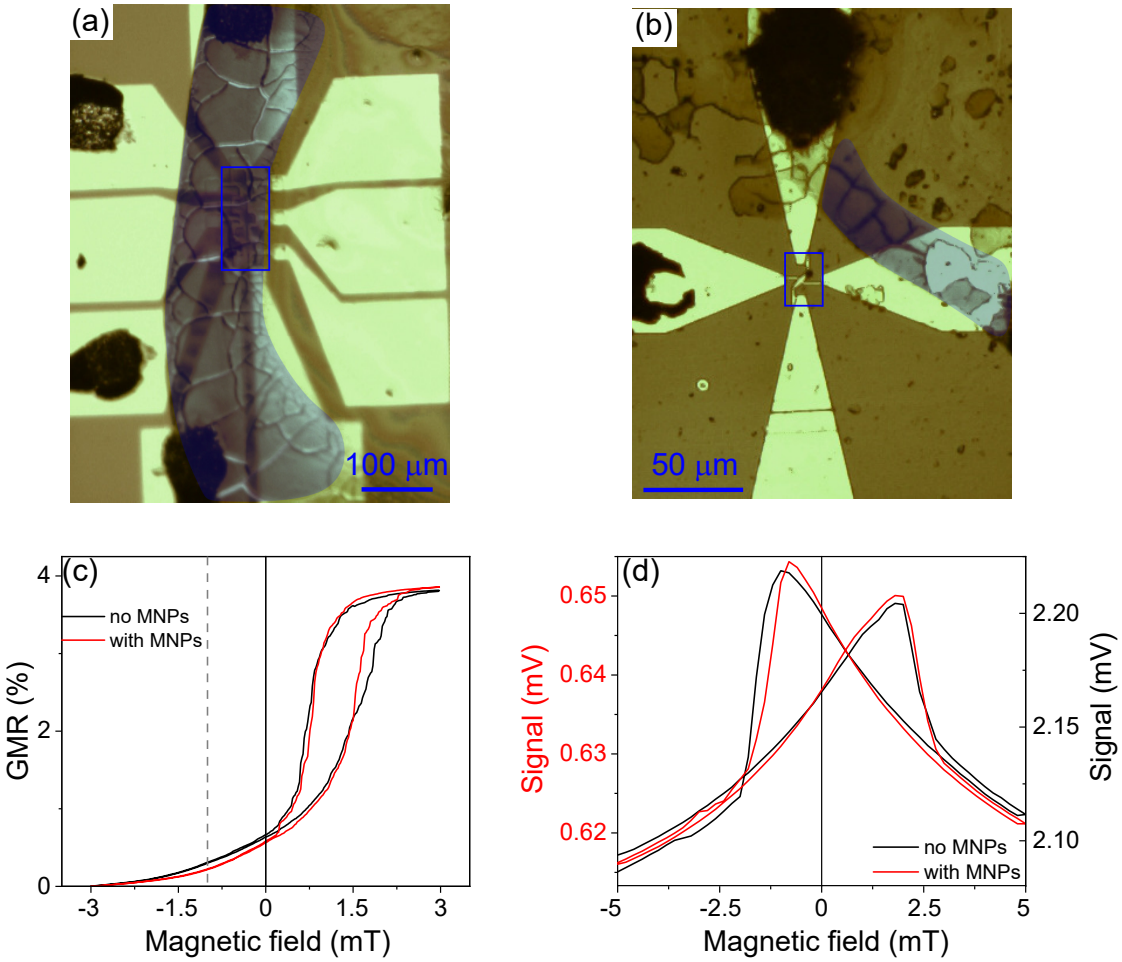

Figure 3.6: Static magnetic nanoparticles detection with a GMR sensor a PHE sensors. Microscope images of (a) the GMR sensor and (b) PHE sensor with a dried MNPs drop. The outer ring of the drop is highlighted in blue. The sensing area for both sensors is marked with a blue rectangle. Hysteresis loops measured without any MNPs (black lines) and with MNPs (red lines) for the (c) GMR sensor and (d) PHE sensor.

of the GMR meander. In the case of the PHE sensor, there is a detectable change of the signal as well, however, not significant enough to be surely correlated with the MNPs. As can be seen from Fig.3.6(b), unlike in the case of the GMR sensor, there are no large amounts of particles concentrated in the middle of the PHE sensing area.

In conclusion, the static detection experiments showed, that it is indeed possible to qualitatively detect the presence of magnetic nanoparticles using both GMR and PHE sensors. However, the detection method, in which a drop of a MNPs solution is placed manually on top of the sensor area is not optimal. One of the reasons, is that it is extremely difficult to precisely place a drop onto a desired area. Another reason, is that the number of particles in a drop cannot be determined, thus excluding quantitative MNPs

detection. Ultimately, it was decided to pursue the concept of utilizing magnetic field lines in a stack to magnetize particles and PHE sensors. Ultimately, all the consequent measurements were performed on a combined platform with a microfluidic channel fabricated on top of an isolated PHE sensor (as discussed in more detail in Chapter 2), thus enabling the detection of a controlled number of particles in a fluid and not a dried drop.

One of the first experiments, in which a dynamic detection method was implemented, utilized an array of PHE sensors connected to each other. Figure 3.7(a) depicts a sample containing two separate arrays with a microfluidic channel on top and connected to a SAMTEC connector board provided by a MADIA partner CNR-Lecce. As can be seen from Fig. 3.7(b), there are two arrays of Hall crosses connected together in a line and each Hall cross can be read out separately. All the electrical contact lines end at top and bottom edges, so the sample can be inserted into the connector board, which means only one side (one array) can be connected at the same time.

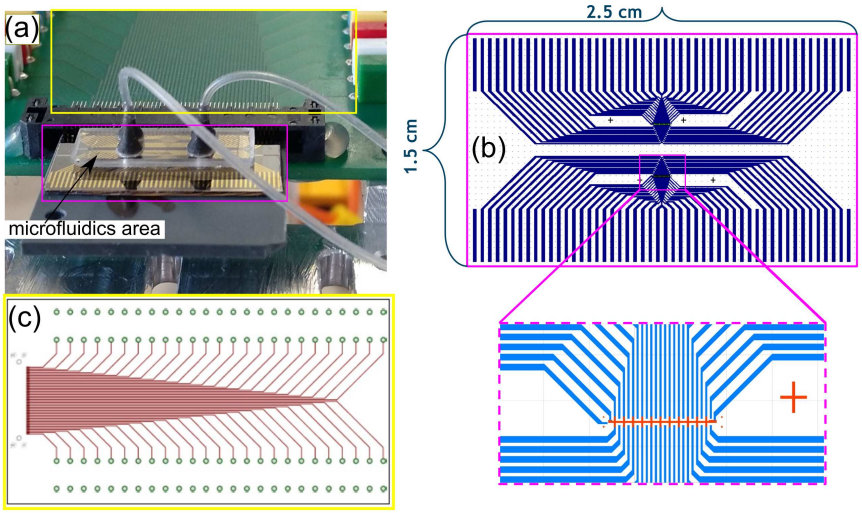

Figure 3.7: (a) Image of the PHE sensor array (marked in magenta) connected to the measurement board (marked in yellow) with a microfluidic channel fabricated on top. (b) CAD mask of the half of the PHE sensor array. The sample consists of two mirrored halves. (c) Schematic representation of the measurement board.

First, the Hall crosses in an array were characterized by measuring their hysteresis loops of the first and second harmonic signals and compared to the loops measured previously for a single Hall cross of the identical stack. When 1ω signals are compared, as shown in Fig.3.8(a), it can be seen, that the hysteresis loops shape and the overall signal of few mV are comparable to the previously characterized single Hall cross. However, in the case of 2ω signal an unexplained behavior was detected and no comparable response was measured for any of the Hall crosses in the array. Additionally, the 2ω signal

level is two orders of magnitude larger than expected.

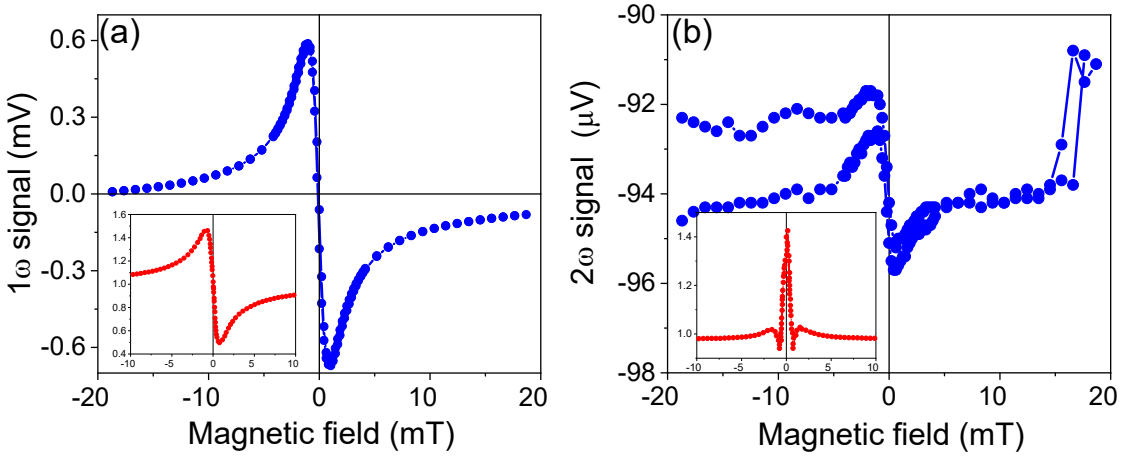

Figure 3.8: (a) Measured first harmonic response for a Hall cross in an array with a microfluidic channel. Inset in (a) depicts the expected first harmonic response detected for a single Hall cross without a microfluidic channel. (b) Second harmonic signal measured for a Hall cross in an array with a microfluidic channel on top. Inset in (b) shows the expected behavior.

Nevertheless, the sample was used further for the experiments with DI water and MNPs solution to test the sealing and change of the signal. A first test comprised of DI water being pumped through the microfluidic channel and several Hall crosses in the array were simultaneously contacted and their signal was monitored. The sensors were fed with 10 mA AC current and the resulting magnitude R, phase, X and Y responses of both harmonics were detected simultaneously. To move DI water or later MNPs solution through the channel, a microfluidic pump was used, as described in Chapter 2. This experiment proved stability of the sensors, since no change of the signal was detected, apart of that coming from the cooling effect. The whole system (sample + microfluidics) was found to be leakage-free and the hysteresis loops measured afterwards were identical to the ones measured previously.

The next step was to inject a MNPs solution through the channel and monitor any changes in the sensors' signal, related to the presence of the nanoparticles. As can be observed from the Fig. 3.9(a), at the beginning, when no particles were present in the channel, a reference signal was measured for some time. Afterwards, the MNPs solution was pumped and after the channel was filled, a change of signal for both harmonics and all sensors was observed. The solution was further pumped until the channel was empty again. It was expected, that when the MNPs solution was pumped away completely, the response of the sensors should go back to the initial levels. It is evident from Fig. 3.9(a) that this was not the case, as all the senors exhibit strange behavior after the microfluidic

channel was empty. Figure 3.9(b) depicts the current applied to the sensors and it can be seen, that shortly after the channel was filled with the solution, there a was a drop from 10 mA to around 10 μA, even though the sensors' signal did not vanish. Optical inspection of the sample revealed a damaged microfluidic channel, as shown in the inset in Fig. 3.9(b). This indicates that the measured sensors' responses after the damage occurred are related to some additional effects, not coming from the PHE.

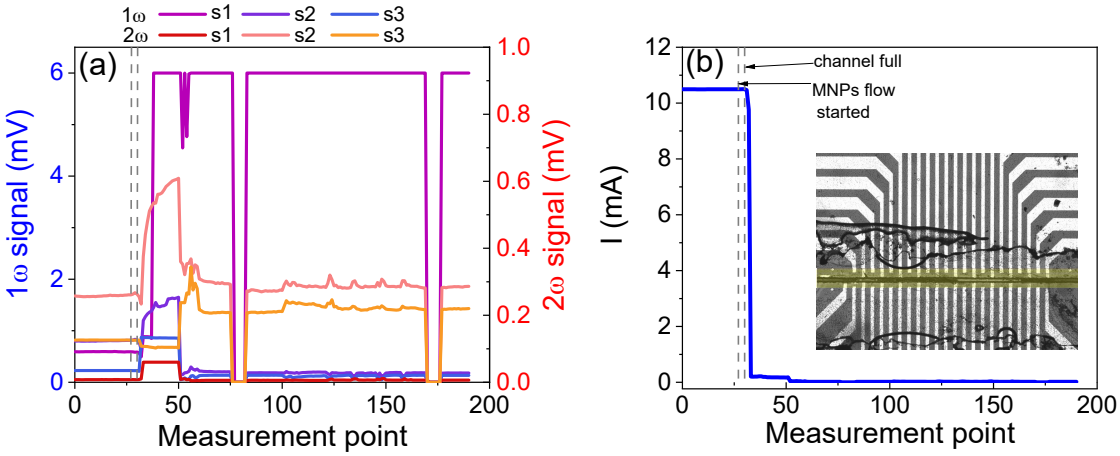

Figure 3.9: (a) First and second harmonic signals detected while MNPs flowing through the microfluidic channel. (b) Current flowing through the sensors during the experiment. Inset in (b) shows an optical image of the sample with the damaged microfluidic channel highlighted in yellow.

Ultimately, all the gathered information was then thoroughly analyzed and it was concluded that the strange 2ω behavior and the signal detected with the damaged microfluidic channel are associated to cross-talk emerging due to capacitive coupling in the Si substrate. This coupling was not detected previously for single Hall crosses and was found for the first time in the Hall crosses array, designed specifically to fit the SAMTEC connector board. When a closer look at the overall sample and board design is taken (see Fig. 3.7), it is evident that the long conducting lines close to each other are responsible for the generation of parasitic signals of the 2nd order, that add up to the sensor signal. The use of Si/SiO_2 substrate with only 50 nm Si dioxide is, thus, not optimal, as the conducting layer of Si underneath induces large capacitive coupling from the lines in the Si. To avoid all these issues it was decided to utilize a fully insulating single crystal MgO substrate, placed into a standard 1×1 cm chip carrier for further experiments.

The final experiments, in which a quantitative magnetic nanoparticles detection was successfully performed, were based on the static detection principle. For this case, a sample containing a single Hall cross deposited onto fully isolating MgO substrate was

used. Here, a drop of 1 μl of nanoparticle solution with 25 nm total diameter (8 nm magnetic core), diluted in proportion 1:10 with DI water was used. The sensors' response with and without MNPs was measured by sweeping the applied AC voltage from 100 mV to 12 V for five different frequencies. Before a MNPs drop was placed, the sensor was characterized and cooled down to room temperature for two hours. Afterwards, the sensor response with particles was detected, as presented in Fig. 3.10(a) (red squares) for one selected frequency of 367.713 Hz, where the largest signal difference was observed.

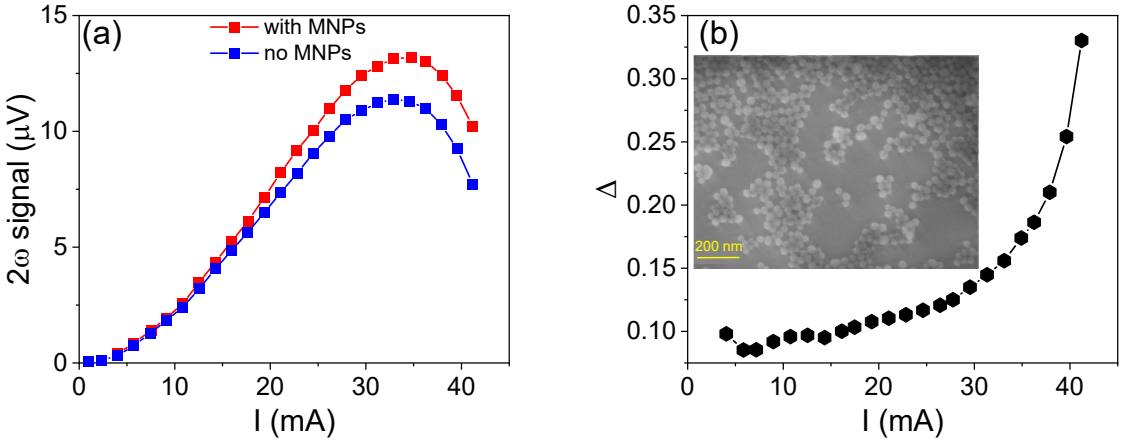

Figure 3.10: (a) Second harmonic signal of the Hall cross with (red squares) and without (blue squares) a MNPs drop. (b) The relative signal change Δ as a function of the applied current. Inset in (b) shows a SEM image of the MNPs in the drop.

The relative signal change was then determined as following

$$\Delta = \frac{V_{MNPs} - V_{NoMNPs}}{V_{NoMNPs}}, \tag{3.1}$$

and it is shown in Fig. 3.10(b) as a function of the applied current, with the maximum change of 33% at 40 mA. As the last step the number of particles, located on the sensor's surface was estimated by SEM-inspection and a selected SEM image is shown as the inset in Fig. 3.10(b). The details on the MNPs measurements and the particles calculations can be found elsewhere [155, 156].

In conclusion, it was demonstrated that the optimized single Hall cross PHE sensors deposited onto fully insulating MgO substrate are indeed able to detect low concentrations of magnetic nanoparticles. With a sensor's area of 400 μm^2 it was possible to detect 10^5 particles with a 8 nm magnetic core. These finding can be further improved by decreasing the sensor's area. For example, by optimizing the design of the microfluidic channel, the sensor's area down to 50 μm^2 is feasible. Alternatively, MNPs with

larger magnetic core can be used, since the strength of the stray fields is expected to be larger.

3.3 Noise characterizations

As discussed previously, noise is an important parameter, which needs to be characterized, since noise establishes the ultimate limit of measurement sensitivity. The noise characterizations within this thesis were performed for two PHE samples, with the same thin film stack, but deposited onto different substrates, one being 525 μm thick Si with a conductivity of σ = 0.2 - 1 S/m and Boron doping, with the top 50 nm being comprised of silicon dioxide, obtained by thermal oxidation. The second substrate used here was fully insulating single crystal MgO(100) and is a commercial substrate from CrysTec [159], with the thickness of 500 μm. The choice of substrates is based upon the conclusions of the magnetic particles detection experiments, as discussed previously. The thin films stack consisted of: substrate/Ru 3/MnIr 10/$Ni_{81}Fe_{19}$ 4/Ru 1.7/$Ni_{81}Fe_{19}$ 10/Ru 5.6, with substrate being either Si/SiO_2 or MgO (thicknesses are given in nm). The stack used here was developed as discussed above (see Subsection 3.1.3). The samples were patterned into Hall crosses with various widths between 6 μm and 24 μm by means of optical (for MgO) and e-beam (for Si) lithography. Figure 3.11(a) shows a microscope image of a Hall cross, while Fig. 3.11(b) depicts the CAD mask used for both samples.

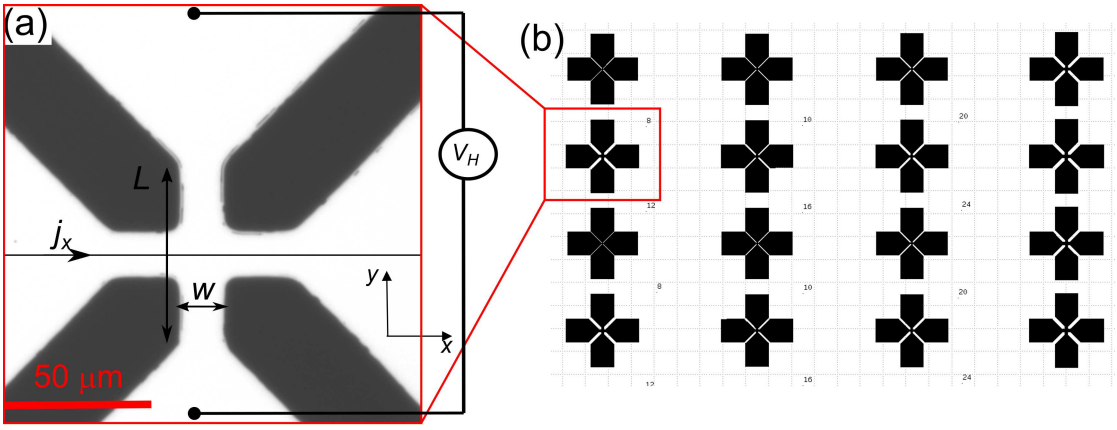

Figure 3.11: (a) Microscope image of the Hall cross. (b) CAD mask used for fabrication with various Hall cross sizes.

After patterning, the resistances of both longitudinal (R_{yy}) and transverse (R_{xy}) arms were measured. The obtained resistances and their ratios are shown in the Table 3.2. It is expected for an ideally patterned Hall cross, that R_{yy}/R_{xy} = 1, however due to even small misalignment during the lithography process the R_{yy} and R_{xy} may differ, thus changing

Table 3.2: Electrical resistance measured for Hall crosses of various sizes for both substrates

substrate	w (μm)	R_{yy} (Ω)	R_{xy} (Ω)	R_{yy}/R_{xy}
	6	93.2	104	0.9
	8	95.6	96	$\approx$1
Si	10	94.6	90.5	$\approx$1
	20	86	83	$\approx$1
	24	75.6	81.4	0.93
	10	160.7	132.5	1.21
	12	134.5	126.9	1.1
MgO	16	117.4	111.5	1.1
	20	101.5	101	$\approx$1
	24	97.1	93.2	1.04

this ratio. It can be seen, that for most Hall crosses the R_{yy}/R_{xy} is indeed $\approx$1, yet for the case of MgO substrate, there are more deviations. Additionally, the overall resistance values for the MgO sample are higher for all the sizes. It ix expected, that resistance decreases with increasing size as $1/w$. Nevertheless, as can be seen from the Table 3.2, there is a constant resistance term, which is independent from the Hall cross size and corresponds to the resistance of the Ta/Au contacts. This contact resistance is found to be 50 Ω and 72 Ω for MgO and Si samples, respectively.

The samples' magnetic and electrical properties were characterized by measuring their DC magnetic field loops. Here, an AC current with amplitudes between 10 and 80 mA (peak-to-peak) and modulation frequency of 767.713 Hz was injected into the Hall crosses in the x direction, as depicted in Fig.3.11(a), with j_x being the applied AC charge current density. A DC magnetic field in the range from -20 to 20 mT was then applied along the current direction. The 1ω and 2ω components of the transverse voltage were detected, as shown in Fig.3.12.

When a detailed look at the 1ω signal is taken, it can be seen, that both samples yield an expected shape with linear field dependence and high slope around zero field (see Fig.3.12(a) and (c) for Si and MgO, respectively). It is, however, striking that the MgO sample exhibits rather high offset voltage and the signal is not centered around zero, unlike in the case of Si. This is a puzzling finding, since the main difference between the sample is the substrate material. This question will be discussed later in this section in more detail. The 2ω signal, on the other hand, shows high sensitivity at zero field, as can be concluded from the field dependence shown in Fig.3.12(b) and (d).

The noise spectra were measured, following the procedure described in Chapter 2. Figure 3.13 shows the noise spectra for the 20 μm Hall crosses at four AC applied

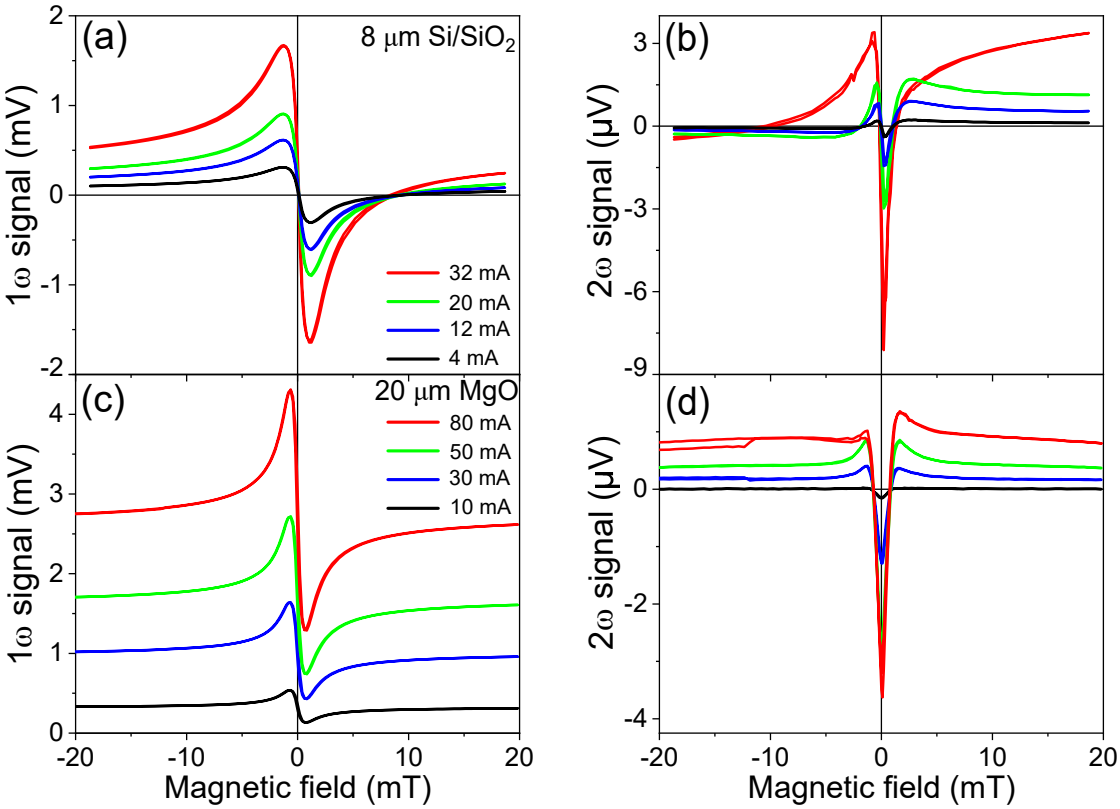

Figure 3.12: Hysteresis loops of the (a) first and (b) second harmonic response of the 8 μm Hall cross on the Si/SiO_2 substrate. Hysteresis loops of the (c) first and (d) second harmonic response of the 20 μm Hall cross on the MgO substrate. The loops were measured at four distinct AC current amplitudes.

voltages and both substrates for the first Fig.3.13(a) and (c), and second (b) and (d) harmonics.

Using the experimentally obtained noise spectra, the linear fits of the flicker noise-dominant range and white noise-dominant range were performed separately and the $1/f$ knee frequency was the extracted as an intersection of the both fits (see an example in the inset in Fig.3.13(d)). The noise levels at 10 Hz (for the first harmonic) and 20 Hz (for the second harmonic) were then extracted from the measured spectra for the further analysis. Finally, white noise levels were derived, as these values give the important information on the ultimate detectivity limitation. Selected values of the extracted parameters for the 20 μm Hall cross at maximum applied AC voltage are shown in the Table 3.3.

It can be observed from the Table 3.3 and Fig.3.13, that the Si sample exhibits lower white noise for both first and second harmonic components. This finding is surprising, since the thin film stacks are identical and the only significant difference is the substrate material. Therefore, a closer look at various parameters and their dependence is taken

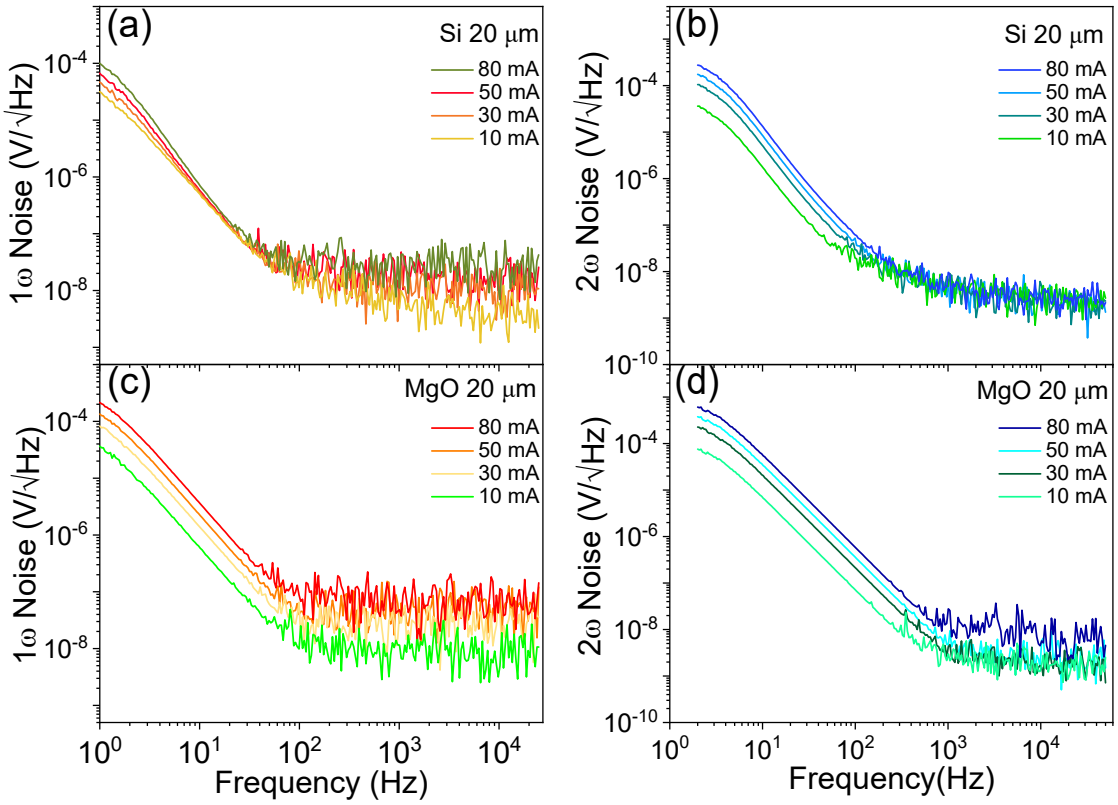

Figure 3.13: Noise measured at the four distinct applied AC current amplitudes for (a) first and (b) second harmonics for the 20 μm Hall cross on Si/SiO_2 substrate. Noise levels of (c) first and (d) second harmonics for the 20 μm Hall cross on MgO substrate.

in an attempt to find a root cause of this difference.

Following Persson *et al.* [160], a current dependence was studied, to understand the origin of the pink noise. If the this noise is coming only from the PHE sensor itself, it must follow a linear dependence on current, according to Eq. 1.6. Figure 3.14 displays the extracted $1/f$ and white noise for both harmonics and it can be observed, that the $1/f$ noise for the case of both 1ω and 2ω exhibit the linear dependence on current, as expected.

The white S_{white} dependence is presented in Fig.3.14(b). According to Eqs. 1.7 and 1.8, only shot noise depends on the current as $\sqrt{I_{rms}}$. Nevertheless, it is evident from the extracted and raw data, that MgO sample yields higher noise values for both flicker and white noise terms.

The first hypothesis was to compare thermal properties of the substrates, in assumption, that the lower noise levels for Si as compared to MgO sample are connected to the difference in thermal conductivity. The Si/SiO_2 substrate from Siegert wafer consisted of 525 μm thick Si and only 50 nm thermally oxidized SiO_2 layer, thus thermal

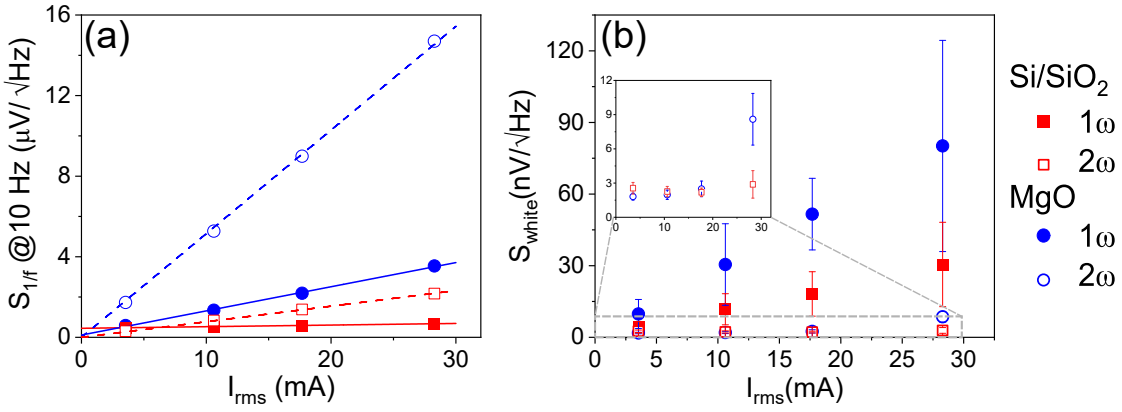

Figure 3.14: Current dependence of (a) the $1/f$ noise and (b) white noise, for the first and second harmonics and both substrates. The inset in (b) is a zoomed in region, showing details of the 2ω behavior.

Table 3.3: Extracted parameters for the 20 μm Hall cross and max applied voltage

	$1/f$ knee (Hz)	S_{therm} (nV/Hz$^{1/2}$)	Σ (μV/mT)	D_B (nT/Hz$^{1/2}$)
MgO 1ω	70	80.2	-	-
MgO 2ω	880	8.60	0.8	13
Si/SiO$_2$ 1ω	39	30.5	-	-
Si/SiO$_2$ 2ω	398	2.88	0.7	7.8

conductivity of Si of $\sim$ 150 W/mK [161, 162] dominates and acts as a more effective heat sink as in the case of MgO substrate, with thermal conductivity of $\sim$ 30 W/mK. According to Eq.1.7, an increase of temperature and/or resistance leads to higher noise levels. According to Raquet [163], a high current density (10^7 A/cm^2) flowing through a thin film stack promotes heating effects and can potentially activate new magnetic sources, like new domains or fluctuations. Therefore, a significantly lower noise levels for both harmonics in case of Si/SiO$_2$ substrate could be explained by the difference in thermal conductivity. On the other hand, the AC excitation current density used in the measurements here is in the range 0.05 - 0.4 $\times$ 10^7 A/cm^2 and, therefore, is not expected to induce significant overheating.

Another reason for the higher overall noise in the MgO sample can be attributed to the quality of the lithography, since the MgO sample was patterned via optical lithography setup, while the Si sample by means of the e-beam lithography. Figure 3.15 demonstrates the SEM images of the Hall crosses for both samples. A clear difference in the structures' quality can be recognized. While the Hall cross on Si substrate possesses sharp, well-defined edges and equal widths of all arms, as can be seen in Fig. 3.15(b), the Hall cross patterned on the MgO substrate has rounded edges and unequal

widths of top and bottom arms (Fig. 3.15(c)). This alone can explain the large 1ω signal offset in the hysteresis loops of the MgO sample (see Fig. 3.12(c)).

The voltage offsets were then investigated in more detail for all the sizes and substrates. The results are presented in Fig. 3.15(a). When the offsets are plotted as a function of the applied voltage, it is evident, that they all follow a linear dependence and converge to zero in the absence of applied voltage for both substrates. All the Hall crosses patterned on the MgO substrate yield significantly higher slopes (between 0.2 and 0.15) of the linear fits, when compared to the Hall crosses patterned on the Si substrate. In the case of Si substrate sample, only 10 μm Hall cross shows slightly increased slope of ~ 0.04, while the other Hall crosses yield rather small and constant offset below 0.2 mV.

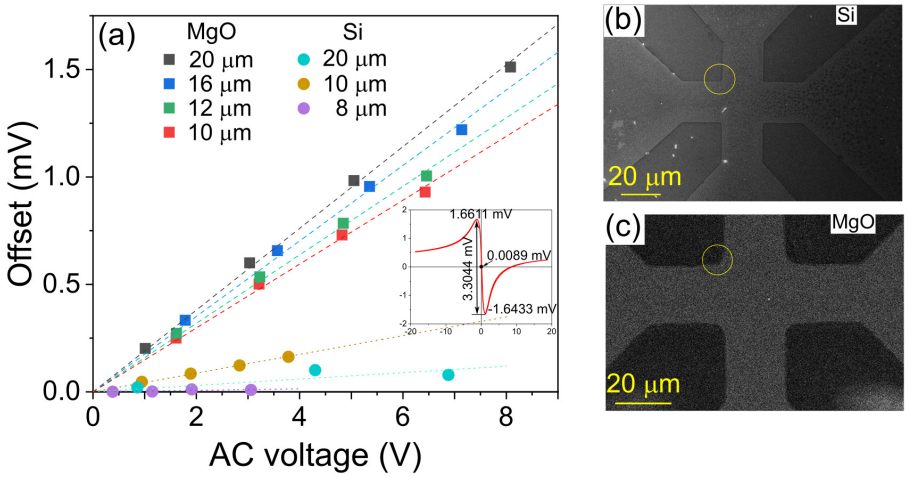

Figure 3.15: (a) Offset voltage extracted from the hysteresis loops. SEM images of a Hall cross for the (b) Si and (c) MgO samples.

The working frequency range is typically of $\sim$ 700 Hz, which is above the $1/f$ knee frequency. Based on these parameters, detectivities of the PHE sensors with the 20 μm Hall cross width and S_{white} are calculated, since this type of noise is dominant above the $1/f$ knee frequency. Thus, the noise at lower frequencies is not taken into account when calculating the detectivity.

The connection between the offset voltage and the increased noise can be explained as following:

- Misalignment of the transverse arms of the Hall cross leads to the emergence of an additional longitudinal component.
- This additional component is then picked up together with the planar Hall voltage

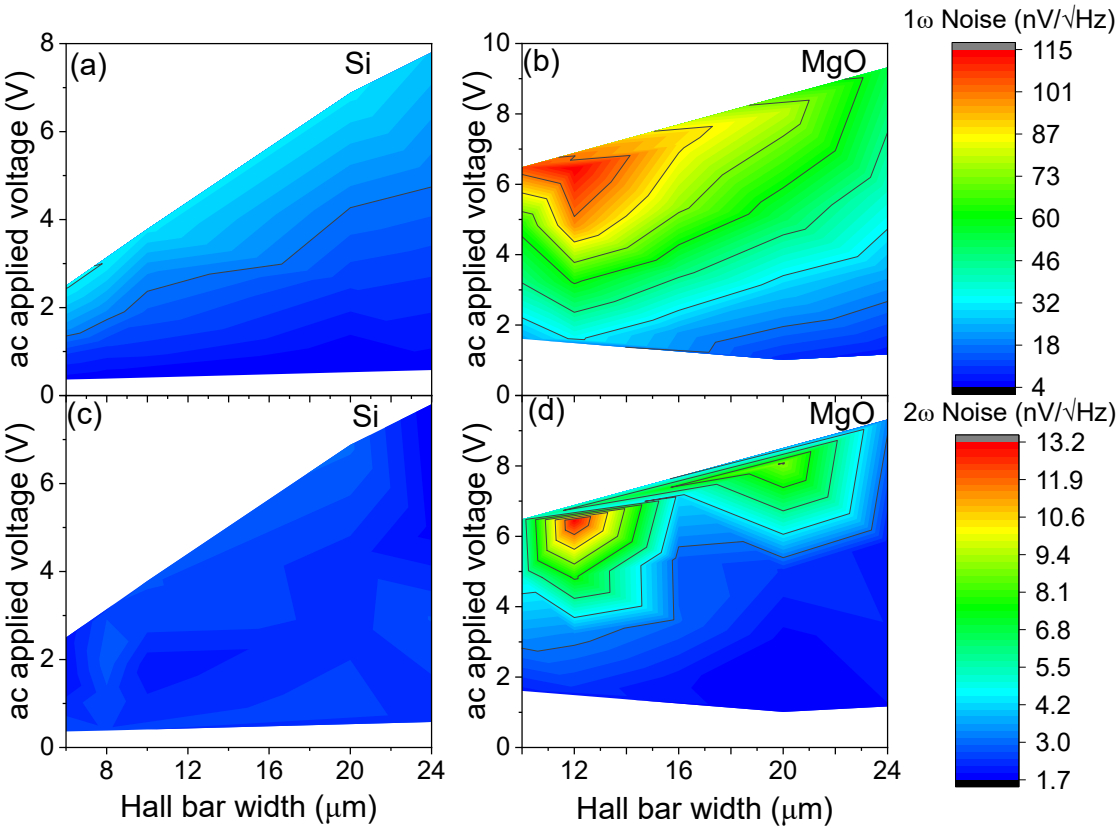

Figure 3.16: Noise dependence on voltage and Hall bar width for both harmonics (a) and (c) Si/SiO_2 substrate and (b) and (d) MgO substrate.

in the transverse measurement geometry. This is observed as the voltage offset in the 1ω signal.

- Thus, the noise measured in such a case corresponds not only to the planar Hall voltage response, but a combination of of PHE and longitudinal voltages.

Ultimately, Figure 3.16 summarizes the noise dependence on both applied voltage and the size of the Hall crosses in the contour plots for both substrates and harmonics. Having such a graphical map of the noise before using the sensor for its final application could help to determine the most optimal parameters, in this case the structure size and applied voltage. Of course, additional limitations may be imposed, such as in the case of MADIA project, with the optimal Hall cross size being equal to the width of the microfluidic channel of 20 μm.

CHAPTER 4

SPIN TRANSPORT IN BI- AND TRILAYERS

This chapter reports the results of the investigation of bi- and trilayers of HM/FM and HM_1/FM/HM_2 structure. In the first section, the samples containing the HMs Pt and Ta are discussed. The detailed analysis of the SOTs, temperature-induced non-linear effects and, ultimately, the USMR has been performed and is shown here. The experimental data was obtained utilizing the harmonic voltage measurement technique as described in details in Chapter 2. The second section focuses on the bi- and trilayer systems, in which Ta is exchanged by W, to study the influence of material choice on the above mentioned effects. Since the W resistivity lays in a wide range, depending on the deposition conditions, the first part of that section is dedicated to the W layer growth optimization.

Parts of the results reported in this chapter were presented at various conferences, including an oral presentation at International Conference on Magnetism and Magnetic Materials MMM-2019. Additionally, the manuscript is under preparation: **A. Moskaltsova**, D. Dyck, J.-M. Schmalhorst, G. Reiss, and T. Kuschel, *"Unidirectional spin Hall magnetoresistance and spin-orbit torques in HM_1/Co/HM_2 trilayer systems"* (in preparation) (2021).

4.1 Pt and Ta systems

4.1.1 Samples description

In this chapter, the following reference samples containing the HM materials Pt and Ta were studied: sub/Pt 6/Co 2.5/MgO 2/TaO_x and sub/Ta 6/Co 2.5/MgO 2/TaO_x, further mentioned as Pt/Co and Ta/Co bilayers, respectively. The main set of samples consisted of sub/Pt 6/Co 2.5/Ta 6/MgO 2/TaO_x and sub/Ta 6/Co 2.5/Pt 6/MgO 2/TaO_x, which are later called Pt/Co/Ta and Ta/Co/Pt trilayers, respectively. The substrate used for all the samples discussed in this chapter and mentioned above as sub is Si/SiO_2 with 525 μm Si and 50 nm of thermally oxidized SiO_2. The thicknesses of the layers are indicated in nm. The MgO 2/TaO_x is a capping layer, in which the top Ta oxide layer was obtained by natural oxidation of 2 nm metallic Ta. All the studied thin films stacks are represented graphically in Fig. 4.1. More details on the preparation of the samples

are given in Chapter 2.

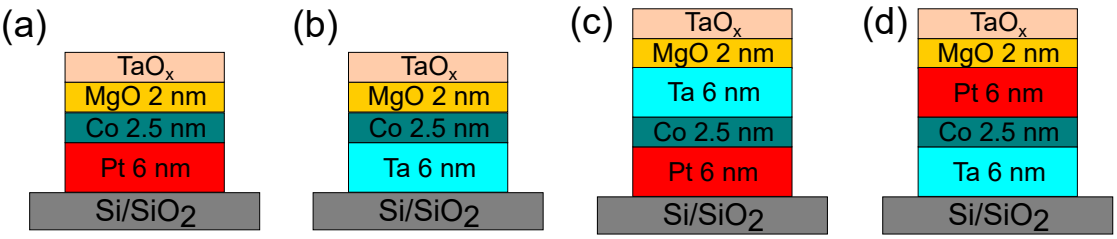

Figure 4.1: Thin films stacks studied in this chapter. (a) and (b) bilayers HM/FM/cap and (c) and (d) trilayers HM_1/FM/HM_2/cap.

4.1.2 Spin-orbit torques and thermal contributions

The main focus of the Pt and Ta bi- and trilayer systems studies was the analysis of the SOT and USMR effects in complex systems with various HM materials at the interface to an FM. An enhancement of the USMR effect in trilayer systems HM_1/FM/HM_2 as compared to a bilayer system HM_1/FM was expected, with HM_1 and HM_2 having the opposite sign of the SHA. In this work, in-plane magnetized Co with the thickness of 2.5 nm was used as an FM. As it was described in Chapter 2 (see Fig. 2.10), in order to extract the pure USMR effect, the SOT and thermal contributions have to be analyzed first and consequently subtracted from the experimental data. Thus, in this section, the details on thermally induced effects as well as SOTs and their separation are discussed.

Before patterning, the thin films stacks were characterized by VSM to ensure their magnetic properties and determine the saturation magnetization M_s and saturation fields H_s. The Pt/Co bilayer is saturated at 1 T, while the Ta/Co bilayer and both trilayers are saturated already at 0.4 T. The thicknesses and roughness of the individual layers were confirmed by XRR. The experimental data and its evaluation will be presented in the next Chapter. All the samples were patterned into Hall bar structures with various widths, as described in detail in Chapter 2.

Figure 4.2 shows the raw data for the second harmonic transverse (Hall) resistance $R_H^{2\omega}$ measured as a function of the in-plane rotation angle φ for the bi- and trilayers. Figures 4.2 (a) and (b) represent the Pt/Co and Ta/Co bilayers data, respectively. In this measurement geometry FL and DL SOTs can be detected. It can be seen, that at 1 T (red circles) the measured signals of Pt/Co and Ta/Co have an opposite sign as expected, since $\theta_{SH}^{Pt} > 0$ and $\theta_{SH}^{Ta} < 0$. The shape of the signal follows cosφ function, which corresponds to the DL SOT (see Eq. (2.13)). On the other hand, the measured

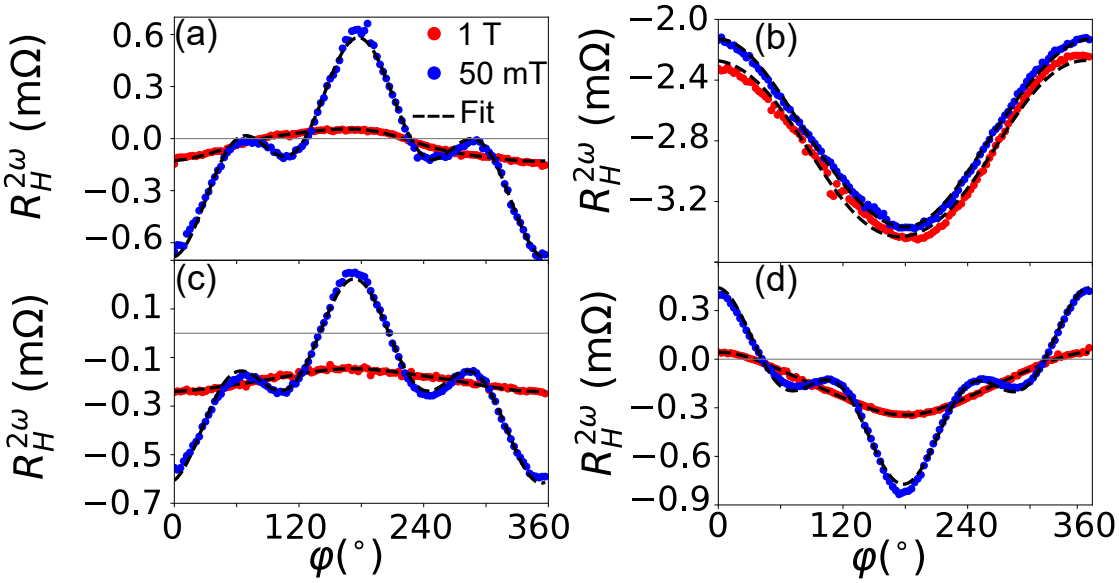

Figure 4.2: Second harmonic Hall resistances (a), (b) for the bilayers and (c), (d) for the trilayers. Red and blue circles correspond to the measured data at 1 T and 0.05 T, respectively. The fits with Eq. (2.13) are shown in black dashed lines.

signal at 50 mT (blue circles) does not change its shape drastically in the case of the Ta/Co bilayer (Fig. 4.2(b)), while for the Pt/Co case additional effect emerges with a higher amplitude and different angular dependence, compared to the signal at 1 T. This additional effect is FL SOT, which becomes more pronounced in the unsaturated state, e.g. for the magnetic fields below 0.4 T and can be described with a (2 cos $^3\varphi$ - cos φ) function (see Eq.2.13).

For the trilayers, which are represented in Figs. 4.2 (c) and (d), the sign of the effects correlates with the sign for the corresponding bilayer. Both Pt/Co/Ta and Ta/Co/Pt trilayers exhibit FL SOT contributions in the field range $<$ 0.4 T (see blue curve measured at 50 mT).

The measurements were performed at a number of fixed magnetic fields from 50 mT to 1 T, to be able to further separate the effects as described in Chapter 2.

Following the analysis method developed by Avci *et al.* [97, 139], the transverse second harmonic voltage measurements were analyzed, to obtain the information on the SOTs as well as to extract the transverse thermal effects. These effects arise from SSE and ANE and must be taken into account. As was shown in Ref. [97], it is important to convert the transverse contribution to the longitudinal one via the geometrical factor for the further USMR analysis. The second harmonic Hall voltage can be described as [105, 164]

$$V_H^{2\omega} = [-\frac{H_{FL+Oe}}{H_{ext}} R_{PHE} \cos 2\varphi + (-\frac{1}{2}\frac{H_{DL}}{H_{eff}} R_{AHE} + \alpha' I_0)] I_{rms} \cos\varphi, \tag{4.1}$$

with H_{FL} and H_{DL} being the FL and DL SOT fields, respectively, R_{PHE} is the PHE resistance, while R_{AHE} is the AHE resistance. I_{rms} is the rms current amplitude. Afterwards, the transverse second harmonic resistance can be described as

$$R_H^{2\omega} = R_{DL}^{2\omega} + R_{\nabla T}^{2\omega} + R_{FL+Oe}^{2\omega} \tag{4.2}$$

with $R_{\nabla T}^{2\omega}$ corresponding to the temperature effects driven by out-of-plane thermal gradients (SSE, ANE). The raw data was fit with a function A · cos φ + B · (2 cos$^3\varphi$ - cos φ), as described in detail in Chapter 2. As a result, two main contributions were then extracted from the fit: one with the prefactor A, corresponding to the sum of DL SOT and temperature effects (proportional to cos φ); and second with the prefactor B being a sum of FL SOT contribution and Oersted fields (proportional to (2 cos$^3\varphi$ - cos φ)).

The next step was to separate the DL SOT and temperature contributions by plotting the corresponding fit parameter against the inverse total magnetic field $1/H_{total}$. The example of such separation is shown in Fig. 4.3 for bi- and trilayers. The DL SOT is expected to have no influence in the large field regime and the only contribution left is related to the temperature effects. Thus, the transverse contribution corresponding to the temperature effects $R_{\nabla T}^{2\omega}$ was defined as the y-axis intercept.

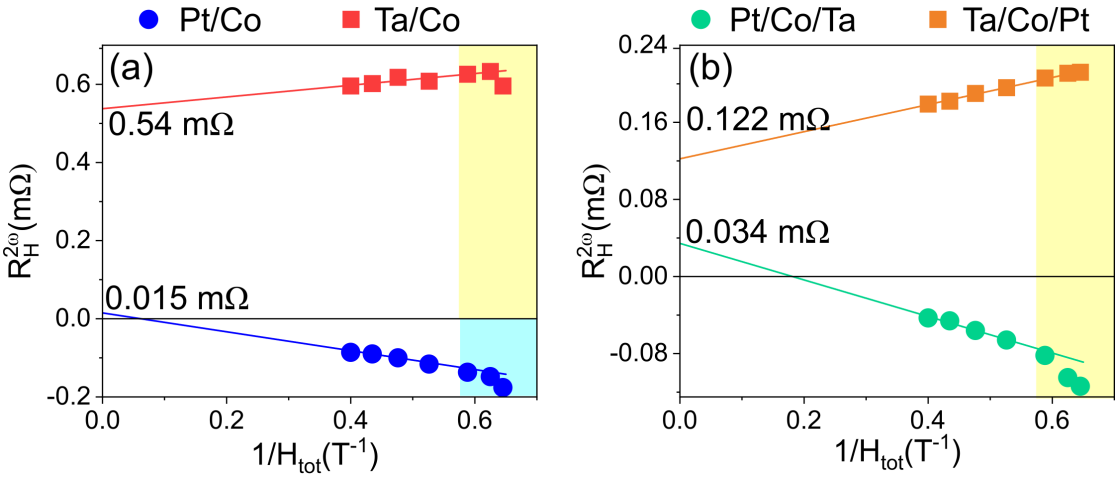

Figure 4.3: $R_H^{2\omega}$ cos φ contribution plotted against inverse magnetic field for (a) bilayers and (b) trilayers. Linear fits performed for the in-plane saturated regime > 0.4 T measured at an applied charge current amplitude of 2.5 mA.

It is evident from Fig. 4.3(a) that Pt/Co bilayer exhibits negligible $R_{\nabla T}^{2\omega}$ value of 15

$\mu\Omega$, while the Ta/Co bilayer possesses a significantly higher value of 0.54 mΩ. On the other hand, both trilayers yield lower, however non-negligible, $R^{2\omega}_{\nabla T}$ values of 34 $\mu\Omega$ and 0.122 mΩ for Pt/Co/Ta and Ta/Co/Pt, respectively.

As can be seen from the Eq. (4.1), R_{AHE} is needed to calculate the DL SOT field. The AHE measurements were performed using a Cryogenic Ltd. Cryostat at room temperature and maximum applied out-of-plane magnetic field of 4 T. The measured data is shown in Fig. 4.4 for all the samples.

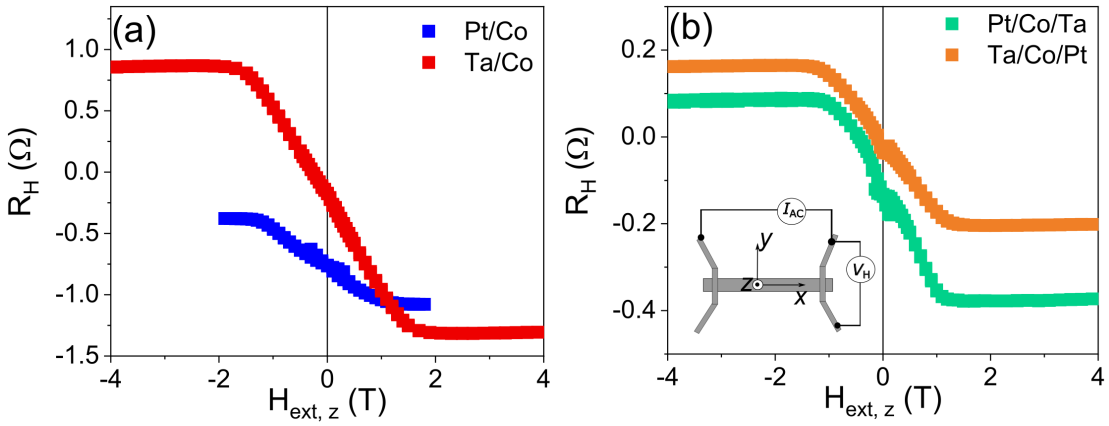

Figure 4.4: R_{AHE} measurement data for (a) bilayer and (b) trilayer samples with the magnetic field applied out-of-plane.

Figure 4.4 (a) shows the raw data for the bilayer samples. The Ta/Co sample (red squares) exhibits the highest AHE amplitude of 1.1 Ω among all the samples. The AHE of the Pt/Co bilayer (depicted in blue squares) was measured only in the range of -2 to 2 T and yields R_{AHE} of 0.35 Ω. In the case of trilayers, represented in Fig. 4.4 (b), both samples exhibit comparable AHE amplitudes of 0.23 Ω and 0.24 Ω for Pt/Co/Ta (turquoise squares) and Ta/Co/Pt (orange squares), respectively.

For the determination of the DL and FL SOT fields (H_{DL} and H_{FL+Oe}, respectively), Eq. (4.1) was used. The extracted SOT fields for bi- and trilayers at 2.5 mA applied current are shown in Figure 4.5. As expected, there is no dependence on the magnetic field, except for the unsaturated regime in the field range $<$ 0.4 T (in-plane). It can be seen, that Pt/Co and Pt/Co/Ta samples (open blue and turquoise circles, respectively) yield comparable DL SOT fields of 0.721 mT and 0.84 mT, respectively. In contrast, the Ta-based samples exhibit rather different DL SOT fields, with $H_{DL}^{Ta/Co/Pt}$ (open orange squares) being 5$\times$ larger than for Ta/Co bilayer (open red squares). The measured values are -0.71 mT and -0.133 mT for Ta/Co/Pt and Ta/Co, respectively.

The extracted term H_{FL+Oe} is a sum of FL SOT and Oersted field, generated by the

charge current flowing in Pt and/or Ta layer(s). The Oersted field can be then calculated as $\mu_0 I/2w$, in which w is the width of the current line and μ_0 is the vacuum permeability, μ_0 = 1.2566 $\times$ 10^{-6} H/m. For the current amplitude of 2.5 mA and Hall bar width of 4 μm, H_{Oe} = -0.39 mT. This value was later subtracted for the correct SOTs efficiency calculations. The H_{FL+Oe} fields are rather low in comparison to the DL SOT, with only Ta/Co/Pt sample exhibiting FL+Oe SOT field of 0.335 mT (filled orange squares). The remaining samples show H_{FL+Oe} values with a negative sign and lower than 0.2 mT.

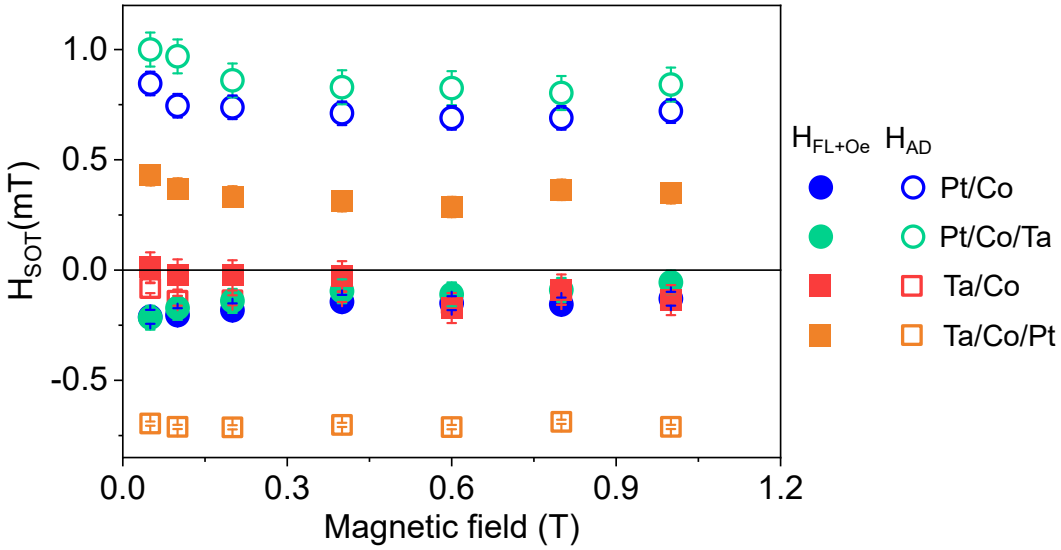

Figure 4.5: DL and FL SOT fields as a function of external magnetic field. The deviations in the low field regime are due to the unsaturated magnetization state.

As discussed in Chapter 1, one way to evaluate the SOTs is to compare the SOTs efficiencies (ξ_{DL} and ξ_{FL}), which were calculated as following

$$\xi_{DL(FL)} = \frac{2e}{\hbar} H_{DL(FL)} \frac{M_s t_{FM}}{j_{HM}}, \tag{4.3}$$

with e being the electron charge, $\hbar$ is the Planck constant, M_s is the saturation magnetization of the FM, t_{FM} is the thickness of the FM layer and j_{HM} is the current density in the HM layer.

Following a model, in which the DL torque is entirely ascribed to the absorption of the spin current produced by the bulk spin Hall effect in the HM [165, 166], the DL SOT efficiency is equal to the spin Hall angle of the HM: $\xi_{DL} = \theta_{SH}$ (for the case of bilayers). Thus, spin Hall angles θ_{SH}^{Pt} = 10%, θ_{SH}^{Ta} = - 3.5% were obtained, which are in agreement with the literature [91, 139]. For the trilayers, however, the extracted values correspond to the effective spin Hall angle θ_{SH}^{eff}, with both HMs contributing to the spin-polarization at both interfaces. The obtained values yield 20% for Pt/Co/Ta and -13% for Ta/Co/Pt

(see Table 4.1 for more details). The lower value for the latter trilayer may be attributed to the Ta oxidation at the substrate or poor interface. The θ_{SH} values obtained in this work are slightly lower than was previously reported (34%) for the same trilayer system, however with perpendicularly magnetized Co [167].

4.1.3 Unidirectional spin Hall magnetoresistance in Pt and Ta- based systems

After the detailed analysis of the second harmonic Hall voltages, a closer look at the second harmonic longitudinal voltages was taken. The corresponding data and fits are shown in Fig. 4.6. A similar behavior as for the transverse case is observed, where for the samples containing Pt, FL SOT contributions arise at lower magnetic fields (here shown for 50 mT in blue circles) at the angles $\varphi = 45°$, 135°, 270° and 315°. In contrast, the signals measured at 1 T (in red circles) all display a sin φ angular dependence with a different sign depending on the underlying HM, positive for Pt (Figs. 4.6 (a) and (c)) and negative for Ta (Figs. 4.6 (b) and (d)). The raw data was then fitted with the A · sin φ + B · (2 $\cos^3\varphi$ - cos φ) function, in which the sin φ contribution gives information on the USMR effect amplitude, while the (2 $\cos^3\varphi$ - cos φ) contribution describes the FL SOT and is only present at lower magnetic fields.

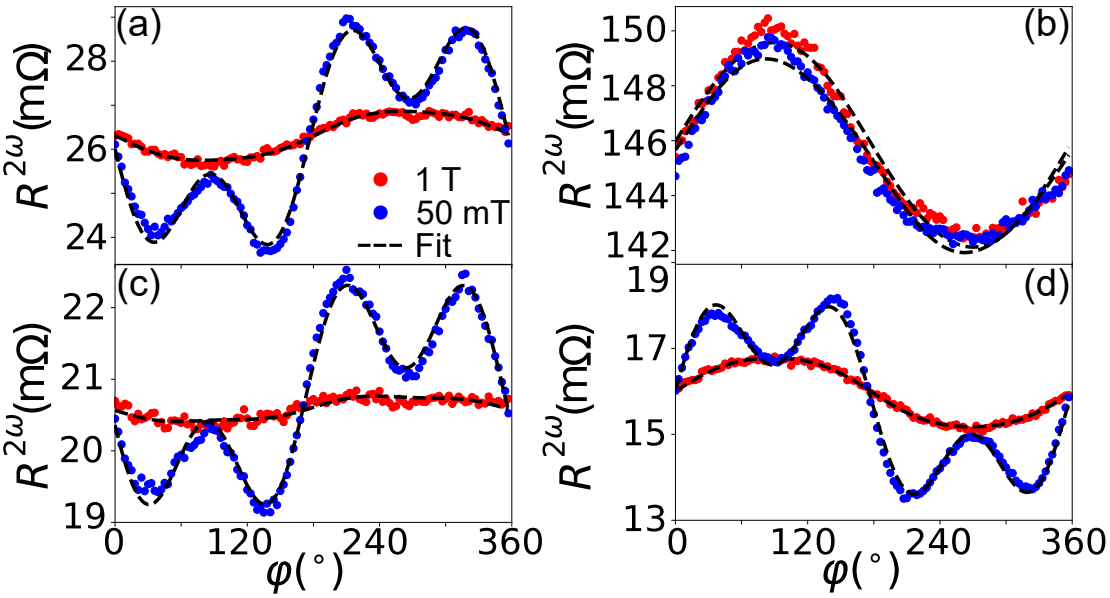

Figure 4.6: Longitudinal second harmonic resistance for (a) Pt/Co and (b) Ta/Co bilayers, (c) Pt/Co/Ta and (d) Ta/Co/Pt trilayers. Blue and red circles correspond to measurements at 1 T and 50 mT, respectively.

Following Avci *et al.* [168], a closer look at the $R^{2\omega}$ field dependence was taken. Figure 4.7(a) shows the raw signal dependence on the applied magnetic field at 2.5 mA.

The data was then fit with a *const.*·H^{-p} function (represented by dashed lines). It is clear that in the saturated regime there is no dependence on the magnetic field. However, Pt containing samples show a variation of the effect magnitude in the unsaturated state, which was attributed to the pronounced FL SOT, which is confirmed by the absence of the magnetic field dependence in the Ta/Co bilayer systems (red squares). The fitting procedure was performed for different current amplitudes and the dependence of the fit parameter p on the current was then analyzed. Figure 4.7(b) reports the p values for all the samples. It is evident that for all the systems there is no current dependence within the studied range. However, as was shown by Avci *et al.* [168] for Co(2.5)/Pt(6) bilayers, the exponent p increases monotonically from 0.6 to 0.9 with increasing current. It is important to note, that the authors utilized current amplitudes in the range from 4.25 mA to 21.25 mA, which is significantly larger, than used in this work. Nevertheless, the Pt/Co/Ta trilayer exhibits a comparable p value of 0.71 even at the lower current amplitudes.

The USMR effect amplitude was then calculated as: $R^{2\omega}_{USMR}$ (at 1 T) = $R^{2\omega}$-$\frac{l}{w}$ $R^{2\omega}_{\nabla T}$, with $R^{2\omega}$ being the raw second harmonic longitudinal signal, $\frac{l}{w} \approx 5$ is the geometrical ratio and $R^{2\omega}_{\nabla T}$ is the transverse thermal contributions, extracted previously.

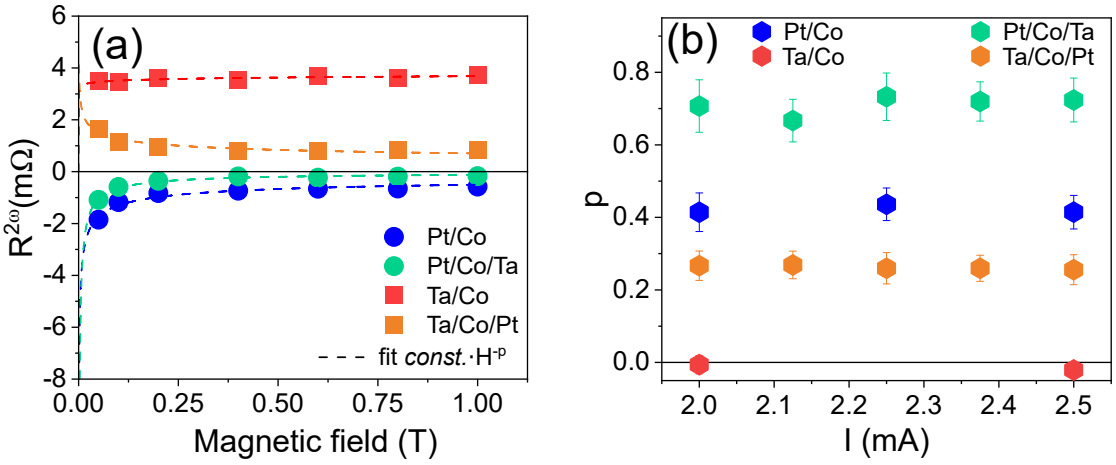

Figure 4.7: (a) $R^{2\omega}$ magnetic field dependence. (b) Extracted exponent p dependence on applied current.

Finally, a detailed analysis of $R^{2\omega}_{USMR}$ current dependence is shown in Fig. 4.8(a). The experimental data was fit with a linear function, converging to 0 with vanishing current. For further comparison, the values at 1×10^7 A/cm^2 (slope of the linear fit) are discussed. It can be seen, that for the Ta-based systems, the bilayer exhibits the highest value of 0.95 mΩ, while the respective trilayer yields $R^{2\omega}_{USMR}$ = 0.23 mΩ. In the case of the Pt based samples, the difference between the extracted USMR values is not large

($R^{2\omega}_{USMR}$ = -0.79 mΩ for the bilayer vs. $R^{2\omega}_{USMR}$ = -0.66 mΩ for the trilayer), however, no enhancement for the trilayer is found. Since Ta has resistivity ∼4 times higher than Co, it is anticipated that most of the current flows through the Co and Pt layers.

Thus, to correctly compare the USMR effect between the different samples, the ratio of the USMR effect $R^{2\omega}_{USMR}$ to the HM(s) resistance was calculated. Figure 4.8(b) displays the dependence of the normalized USMR on HM current density j_{HM}. A modest enhancement of the effect of about 20% as compared to the respective bilayer was obtained for both trilayers with the absolute value of the maximum normalized USMR of -0.32 × 10^{-5} per 10^7 A/cm^2 was observed in Pt/Co/Ta trilayer.

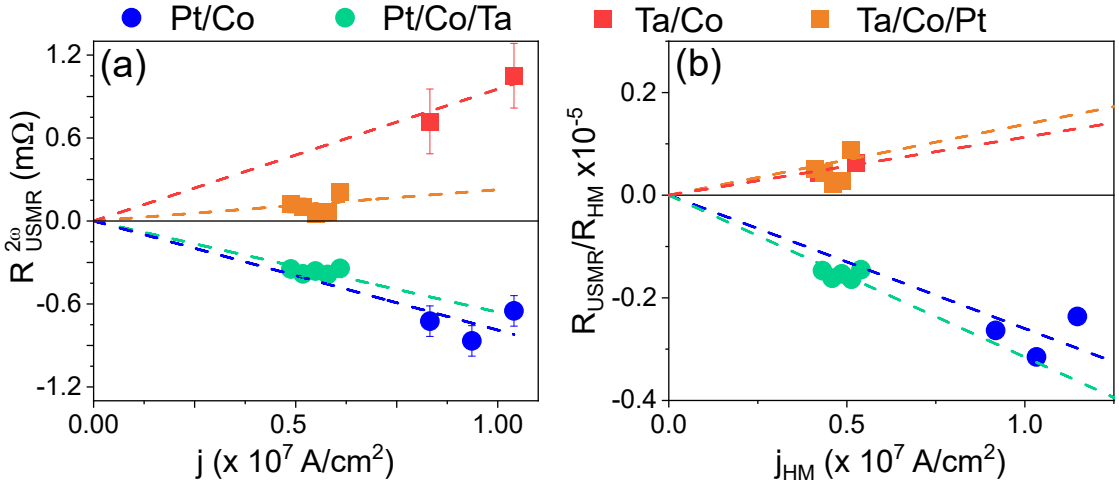

Figure 4.8: (a) $R^{2\omega}_{USMR}$ dependence on the total current density. (b) Normalized USMR dependence on the current density in the HM(s).

Nonetheless, after closer inspection of the experimental data fits, it is evident, that there is still a large uncertainty. For example, if the measured data point at maximum current is ignored for the Pt/Co bilayer, the extracted normalized USMR would be at least the same as for the respective trilayer. The similar picture is observed for the Ta-based samples, where, first of all, only measurements at two different currents were successfully performed and, secondly, the measured points of the trilayer show higher scattering and thus uncertainty of the fit.

Furthermore, taking a closer look at the bilayers, it can be seen that the normalized USMR effect is stronger for Pt than Ta, $|R^{Ta/Co}_{USMR}|$ = 0.11 × 10^{-5} per 10^7 A/cm^2 vs. $|R^{Pt/Co}_{USMR}|$ = 0.26 × 10^{-5} per 10^7 A/cm^2. All of the extracted values are reported in Table 4.1. Such a behavior of the Ta-based systems in comparison to Pt can be explained first of all by the difference in the θ_{SH} values, as Ta yields θ_{SH} of ∼ 3% while θ^{Pt}_{SH} ∼ 10%. Additional factors could also play a significant role, such as:

Table 4.1: A summary of the results for the Pt and Ta-based samples.

sample	I (mA)	R_{PHE} (Ω)	R_{AHE} (Ω)	$\frac{R_{USMR}}{R_{HM}} \times 10^{-5}$ per 10^7 A/cm^2	H_{DL} (mT)	H_{FL+Oe} (mT)	ξ_{DL}	ξ_{FL}
Pt/Co	0.11	0.35	2.0	-0.26	0.782	-0.092	0.098	0.013
			2.25	-0.32	1.064	-0.13	0.12	0.008
			2.5	-0.24	0.721	-0.194	0.07	0.0006
Ta/Co	0.12	1.1	2.0	0.04	-0.135	-0.092	-0.034	0.027
			2.5	0.06	-0.133	-0.136	-0.027	0.013
Pt/Co/Ta	0.07	0.23	2.0	-0.15	0.75	-0.056	0.185	-0.014
			2.125	-0.16	0.84	-0.056	0.19	-0.013
			2.25	-0.15	0.86	-0.084	0.186	-0.018
			2.375	-0.16	0.98	-0.028	0.2	-0.006
			2.5	-0.14	0.84	-0.056	0.17	-0.011
Ta/Co/Pt	0.05	0.2	2.0	0.05	-0.52	0.196	-0.135	0.05
			2.125	0.044	-0.47	0.284	-0.11	0.07
			2.25	0.023	-0.39	0.218	-0.09	0.05
			2.375	0.027	-0.5	0.218	-0.11	0.05
			2.5	0.89	-0.71	0.3348	-0.15	0.07

- intermixing at the Ta/Co interface,
- oxidation of Ta at the substrate,
- spin-transparency of the interface.

Unfortunately, no significant increase of the USMR effect was found for Ta and Pt thin films systems discussed in this section, as predicted by Zhang and Vignale [98]. The authors discussed that for a such a structure, with FM being sandwiched between Pt and Ta, the orientations of the spin accumulations on opposite sides of the FM will be equal, therefore the interface contributions to the USMR expected to add up and enhance the USMR. Hence, another attempt to tune the USMR in HM_1/Co/HM_2 systems was undertaken, in which Ta was exchanged with W. The details are discussed in the following section.

4.2 W-based systems

4.2.1 Sample preparation

Tungsten is a HM with a negative sign of SHA [90], which can exhibit resistivity in a wide range from $\sim$25 to $\sim$300 $\mu\Omega$cm depending on the deposition condition and crystallographic phase (e.g. α, β or the mixture of both phases). In this work, the

Table 4.2: W sputtering parameters for calibration.

thickness nominal (nm)	thickness XRR (nm)	Power (W)	throttle position (%)	sputter time (s)	R (Ω)	ρ ($\mu\Omega$ cm)
6	6.22	15	21	61.37	67.8	190
8	8.11	15	21	81.62	40.1	145
15	15.5	15	21	152.47	11.33	79
6	7.69	3	21	300.6	55.56	193
8	10.25	3	21	400.6	39.02	181
15	17.94	3	21	700.6	18.5	150
6	5.86	30	10	26.54	48.7	129.35
6	7.02	30	10	30.95	27.1	86
8	7.86	30	10	35.18	16.6	59.14

W thin films were deposited using magnetron sputtering technique, while varying the sputter power and throttle position. Consequently, in order to assess the quality of the W thin films crystallographic structure and extract the information about the phase, XRD investigations were performed. The thickness and roughness were determined by means of XRR. Another crucial parameter to monitor after sputtering is the electrical resistivity, as the resistivity in the range $50 < \rho < 150$ $\mu\Omega$ cm was targeted. The measurements were performed using the four-point probe method immediately after the deposition, before the W films could significantly oxidize. The amount of oxygen in the films, however, was not measured. The resistivity measurements were performed only once and the change of the resistivity over time was not monitored.

Table 4.2 summarizes the utilized sputter power and the respective sputter times, as well as the nominal thicknesses, used to prepare tungsten calibration samples.

Figures 4.9(a) and (b) illustrate the XRR and XRD measurements of the selected calibration samples, respectively. The experimental XRR data was fitted utilizing the recursive Parratt algorithm and GenX software [144]. The W layer thickness as well as roughness were extracted from the corresponding best fits, as presented in Fig. 4.9(a) in black solid lines. The determination of the crystallographic phase was carried out using XRD technique.

Finally, resistivity measurements were performed and further compared to the literature values reported by Pai *et al.* [90]. The W layer resistivity was extracted as following: $\rho = \frac{\pi}{ln2} R\, t$, with R being the electrical resistance of the film, measured directly after sputtering with a four-probe technique (see Fig. 4.10(b)) with four equidistant needles in a line, and t is the layer thickness, determined from the XRR measurements.

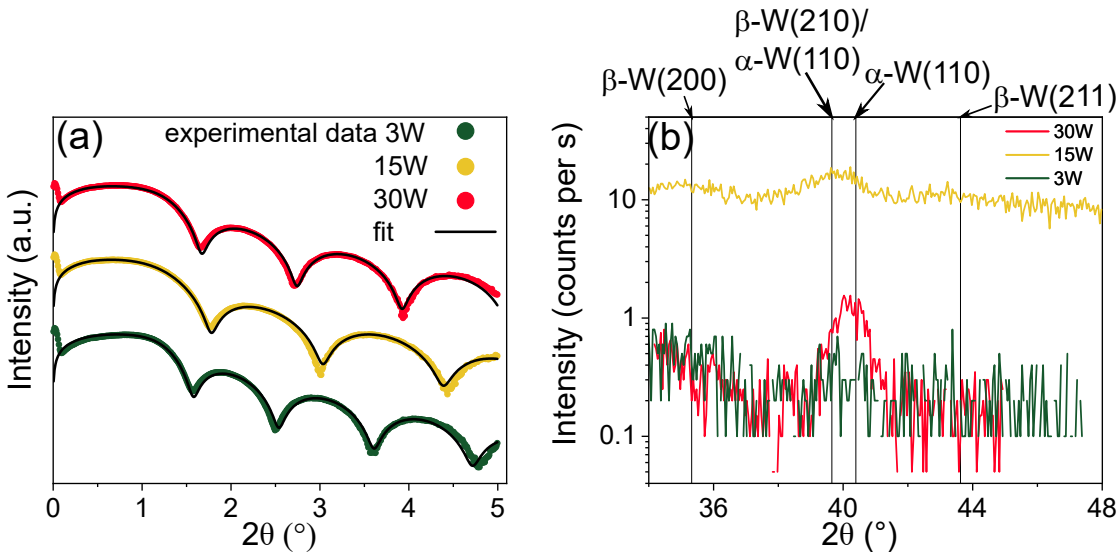

Figure 4.9: (a) XRR measurements to determine the layers thickness. (b) XRD measurements to confirm the phases/crystallographic orientation.

It can be seen from Fig. 4.10(a), that the resistivity values for the samples deposited at 30 W correlate well with the values reported in [90] and are in the targeted range $50 < \rho < 150$ $\mu\Omega$ cm. Hence, these sputtering conditions were chosen for further deposition of the bi- and trilayers.

Thus, after a detailed study and optimization of the deposition parameters for W and investigation of their influence on resistivity and phase, the following set of samples with W instead of Ta, as a material with $\theta_{SH} < 0$, has been prepared for the consequent SOTs and USMR studies: sub/ W 7/Co 2.5 /MgO 2/TaO_x and sub/W 8/Co 2.5/MgO 2/TaO_x and trilayers sub/Pt 6/Co 2.5/W 8/MgO 2/TaO_x and sub/W 8/Co 2.5/Pt 6/MgO 2/TaO_x. The thin films stacks are depicted in the Fig. 4.11. As for the previously discussed Pt and Ta systems, the W thin films were patterned via electron beam lithography into Hall bar structures with various widths between 4 μm and 10 μm.

4.2.2 Spin transport effects

As for the case of Pt and Ta samples, the samples with tungsten studied in this section were measured using the harmonic Hall measurement technique, in which both first and second harmonics of both longitudinal and transverse voltages were simultaneously detected. As it was discussed previously, the analysis of the transverse voltage was performed first to separate the SOTs and the thermal effects.

Figure 4.12 shows the raw data for the (a) and (b) bi- and (c) and (d) trilayers at two selected magnetic field strengths of 1 T (orange circles) and 0.2 T (violet circles). All

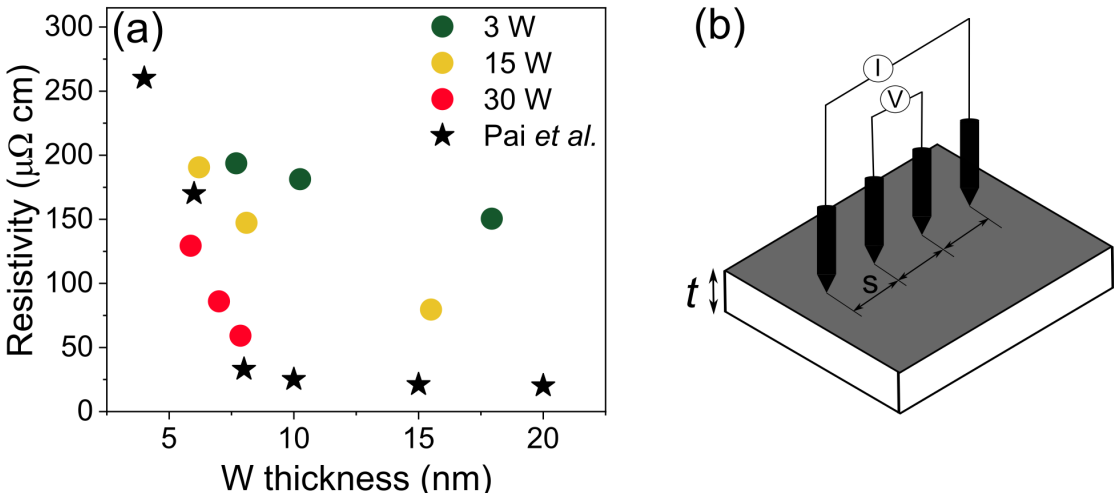

Figure 4.10: (a) Resistivity of the calibration samples at various sputter powers (circles) compared to the literature values taken from Pai *et al.* [90] (red stars). (b) Four-point measurement scheme with equidistant needles.

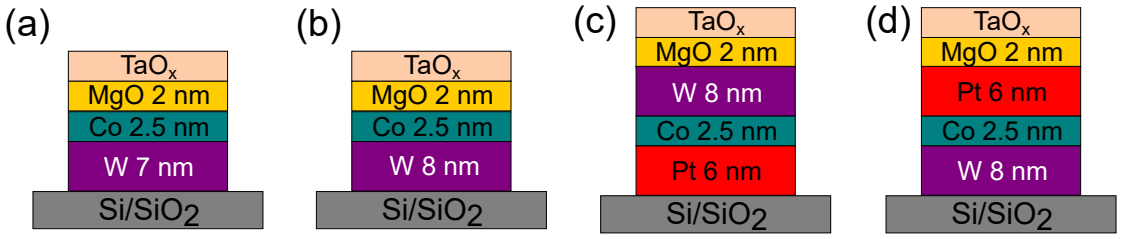

Figure 4.11: Thin films stacks with W. (a) and (b) bilayers HM/FM/cap and (c) and (d) trilayers HM_1/FM/HM_2/cap.

samples were measured at applied magnetic fields from 50 mT to 1 T, as for the case of Pt and Ta samples described previously. However, for W samples the data measured below 0.2 T were showing higher noise levels and thus were not evaluated and not shown here. It can be seen, that the W 7/Co bilayer and the W 8/Co/Pt trilayer systems depicted in Figs. 4.12(a) and (d), respectively, follow the expected cos φ angular dependence. At the same time, the W 8/Co bilayer and the Pt/Co/W 8 trilayer (Figs. 4.12(b) and (c)) do not yield a reliable experimental data and cannot be unambiguously fitted. Thus, the further data analysis procedure was applied only to the W 7/Co bilayer and the W 8/Co/Pt trilayer.

The AHE was measured for all four samples and the experimental data is shown in Fig. 4.13. The inset in (b) demonstrates the measurement geometry. The bilayers depicted in Fig. 4.13 (a) yield very similar shape of the curve and rather comparable R_{AHE} values: $R_{AHE}{}^{W\ 7/Co} = 0.1\ \Omega$ (shown in magenta circles) and $R_{AHE}{}^{W\ 8/Co} = 0.076\ \Omega$ (olive circles). In case of the trilayers, the Pt/Co/W 8 trilayer (dark cyan circles) exhibits the

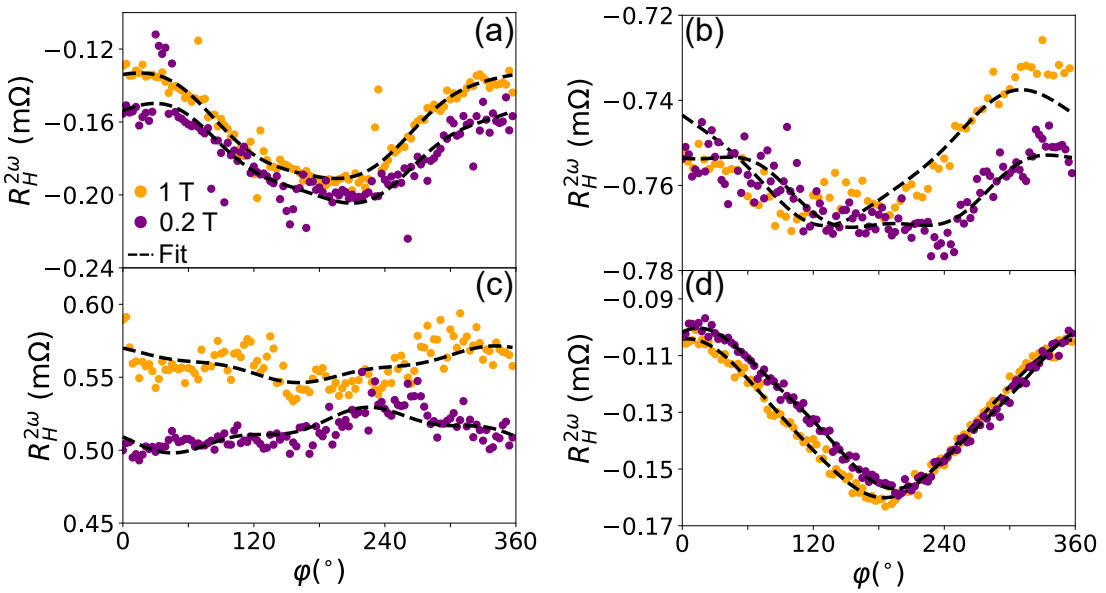

Figure 4.12: Second harmonic Hall resistances for (a) and (b) bi- and (c) and (d) trilayers with W. Orange and purple circles correspond to the measured data at 1 T and 0.2 T, respectively. The fits with the Eq. (2.13) are shown in black dashed lines.

same R_{AHE} value as W 8/Co bilayer, while the trilayer (violet circles) with the switched HMs order yields the lowest value among all four samples of 0.053 Ω. Additionally, the out-of-plane saturation fields were extracted from the AHE measurements, since they are necessary for further data analysis. The H_{sat} of 2.8 T for both bilayers were found, while the Pt/Co/W and W/Co/Pt trilayers exhibit H_{sat} = 1.05 T and 2.05 T, respectively.

After fitting the transverse second harmonic data for various applied magnetic fields with the A · cosφ + B · (2 cos$^3\varphi$ - cosφ) function, the DL and FL SOT contributions were extracted. Figure 4.14(a) presents the extracted $R_H^{2\omega}$ cosφ contribution dependence on the inverse total magnetic field. As discussed previously, it is expected that the cosφ contribution is a sum of temperature effects, which are field-independent, and DL SOT, typically exhibiting a linear $1/H_{tot}$ dependence. As can be seen from the Fig. 4.14(a), the trilayer sample yields a constant value of 26 $\mu\Omega$, while the bilayer converges to 43 $\mu\Omega$ and indeed shows a linear $1/H_{tot}$ dependence. However, when these results are compared to the previously studied Pt and Ta systems, as shown in Fig. 4.14(b), the extracted contributions for W samples are extremely low and, thus, negligible. Additionally, it can be seen, that unlike Pt and Ta stacks, W-based samples yield negligible field dependence, which indicates the absence of the DL SOT in these samples. Hence, the USMR effect for W systems can be written simply as $R^{2\omega} = R^{2\omega}_{USMR}$, since no significant temperature effects have been found.

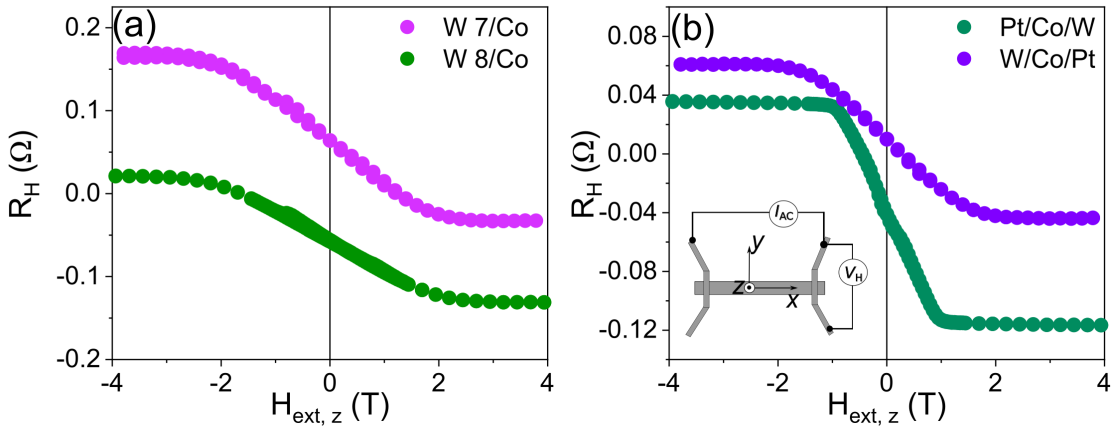

Figure 4.13: R_{AHE} measurement data for W-based (a) bilayer and (b) trilayer samples.

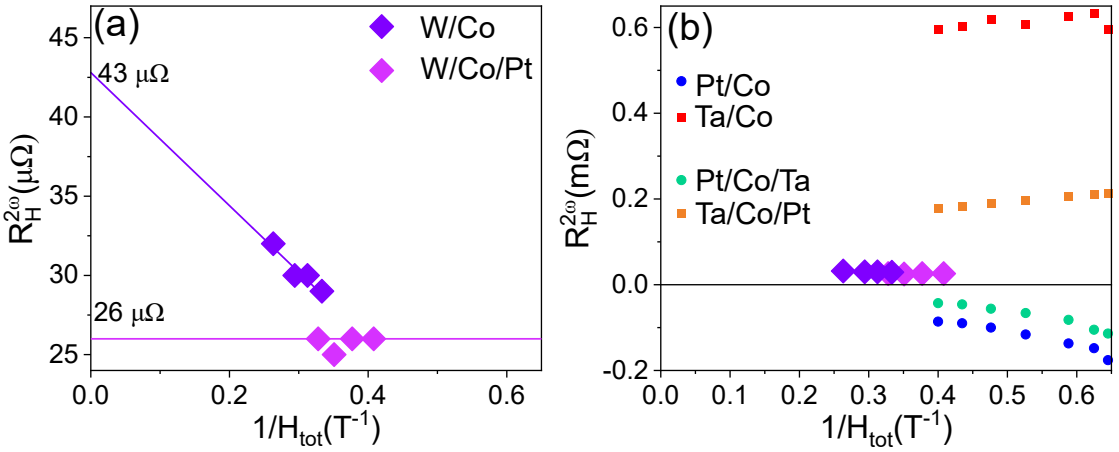

Figure 4.14: (a) $R_H^{2\omega}$ cosφ contribution plotted against the inverse magnetic field for W-based samples. (b) Comparison to the Pt and Ta systems.

Finally, the USMR analysis for the W-based samples have been performed in the same manner as discussed previously (see Section 4.1). The measured raw second harmonic resistances for the four samples are shown in Fig. 4.15. Here, unlike for the transverse case, both W 7/Co and W 8/Co, as seen in Figs. 4.15(a) and (b), respectively, exhibit sin φ dependence attributed to the USMR effect. However, due to the large uncertainty of the data and its fits, the W 8/Co bilayer was not further analyzed. As for the Pt/Co/W trilayer depicted in Fig. 4.15(c), no identifiable signal was detected for both 1 T and 0.2 T fields.

The field dependence of the second harmonic longitudinal resistance is shown in Fig. 4.16(a). Here, for a direct comparison the data for Pt and Ta systems is included as well. It is evident, that when compared to Pt and Ta samples, W-based systems, firstly, yield relatively low $R^{2\omega}$ values and, secondly, do not show any significant field

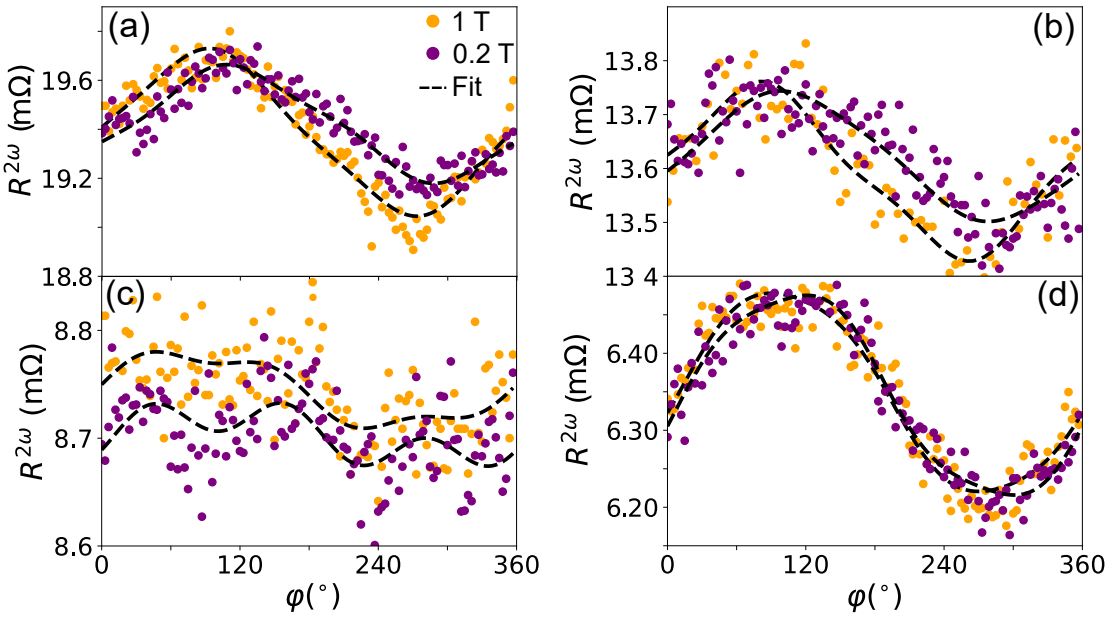

Figure 4.15: Longitudinal second harmonic resistances for (a) and (b) bi- and (c) and (d) trilayers, orange and purple circles correspond to the measurements at 1 T and 0.2 T, respectively.

dependence. When a zoomed-in region as shown in Fig. 4.16(b) is analyzed in detail, one can see, that the W/Co bilayer (in violet stars) exhibits a low field dependence and, when fit with the *const.*·H^{-p} function, the value for the exponent p of 0.21 is extracted, which is slightly lower as for Ta/Co/Pt trilayer, $p = 0.26$. For the case of W/Co/Pt trilayer (magenta stars), the extracted exponent $p = 0.07$, which is higher compared to the Ta/Co bilayer, where no field dependence was found ($p = 0.01$).

Regarding the charge current dependence of the USMR effect, a comparison of all investigated samples (see Fig. 4.16(c)) reveals that the W-based samples yield a slightly higher normalized USMR slope, compared to the Ta-based samples. Still, no significant enhancement of the effect was observed. The extracted normalized USMR of the W bilayer is $\frac{R_{USMR}}{R_{HM}} = 0.147 \times 10^{-5}$, while for the Ta/Co bilayer it is 0.11×10^{-5}. An enhancement of the USMR effect was observed for W- and Ta- based trilayer systems as compared to the respective bilayers. An increase of 10% was measured for W-based sample, whereas Ta-based sample show an increase of 27%. However, the W/Co/Pt trilayer yields the highest normalized USMR effect of 0.162×10^{-5}, which is $\sim 16\%$ higher than for the Ta/Co/Pt trilayer system.

The low values of the W systems may be attributed mainly to the crystallographic phase, since the α - W or the mixture of α and β-phase usually exhibit modest θ_{SH}, unlike pure β phase with a giant spin Hall angle of $\theta_{SH} = 33\%$ [90]. Resistivity is another

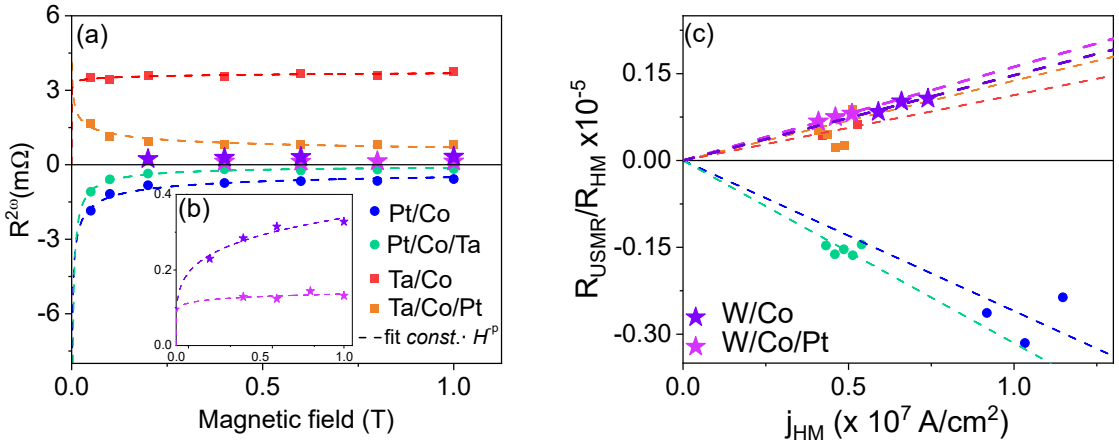

Figure 4.16: (a) $R^{2\omega}$ magnetic field dependence in comparison to the Pt and Ta systems. (b) Zoom-in of the W samples data and the respective fits with the *const.*$\cdot \mathrm{H}^{-p}$ function. (c) Normalized $R^{2\omega}_{USMR}$ charge current dependence for all samples.

major parameter, playing a crucial role in the current distribution in a thin film system and consequently the amount of the spin-current created via the SHE. Another possible reason for rather low USMR values can be W oxidation at the substrate or even on top of the FM, even though a cap of MgO/TaO_x was used for all the samples. Nevertheless, several alternatives for the USMR enhancement have been reported recently, for example by inserting a Cu interlayer, where an USMR increase of 36% due to spin-dependent scattering is observed [169].

In conclusion, the studies of the SOTs and USMR in HM_1/FM/HM_2 systems with Pt, Ta and W showed, that it is indeed possible to tune the USMR effect by adding a second FM/HM interface as compared to the bilayers. Nevertheless, further investigations are needed in order to further improve the thin film systems and thus the achieved tuning of the USMR effect.

CHAPTER 5

MAGNETIC PROXIMITY EFFECT IN BI- AND TRI-LAYER SYSTEMS WITH CO/PT INTERFACE

In this chapter, studies of the MPE in bi- and trilayer systems with Pt/Co and Co/Pt interfaces are reported. Additionally, a comprehensive comparison of the total magnetic moment and the influence of the MPE is discussed. The MPE was studied by means of XRMR and the measurements were conducted at the scattering and diffraction beamline P09 of the third generation synchrotron PETRA III at DESY (Hamburg, Germany). The details on the XRMR experiments as well as the analysis procedure are described in Chapter 2. The total magnetic moment of the samples was obtained via VSM at room temperature.

The results discussed in this chapter were presented at the International Conference on Magnetism and Magnetic Materials - MMM-2019 and published as a peer-reviewed article **A. Moskaltsova**, J. Krieft, D. Graulich, T. Matalla-Wagner, and T. Kuschel, *"Impact of the magnetic proximity effect in Pt on the total magnetic moment of Pt/Co/Ta trilayers studied by x-ray resonant magnetic reflectivity"*, AIP Advances, **10** 015154 (2020) (**Editor's Pick**) [170]. Some of the results were also used for developing an advanced fitting procedure and are part of the publication J. Krieft, D. Graulich, **A. Moskaltsova**, L. Bouchenoire, S. Francoual, and T. Kuschel, *"Advanced data analysis procedure for hard x-ray resonant magnetic reflectivity discussed for Pt thin film samples of various complexity"*, Journal of Physics D: Applied Physics, **53** 375004 (2020) [147].

5.1 Magnetic proximity effect in bilayers and trilayers with Pt/Co interface

The samples studied in this section are the bi- and trilayers Si/SiO_2 50/Ta 6/Co 2.5/MgO 2/TaO_x 2, Si/SiO_2 50/Ta 6/Co 2.5/Pt 6/MgO 2/TaO_x 2 and Si/SiO_2 50/Pt 6/Co 2.5/Ta 6/MgO 2/TaO_x 2. Here the nominal thicknesses are given in nm and the samples are further referenced as Ta/Co, Ta/Co/Pt and Pt/Co/Ta, respectively. The Ta/Co bilayer does not contain Pt and is not expected to have any MPE, thus this system is used as a reference sample in this study.

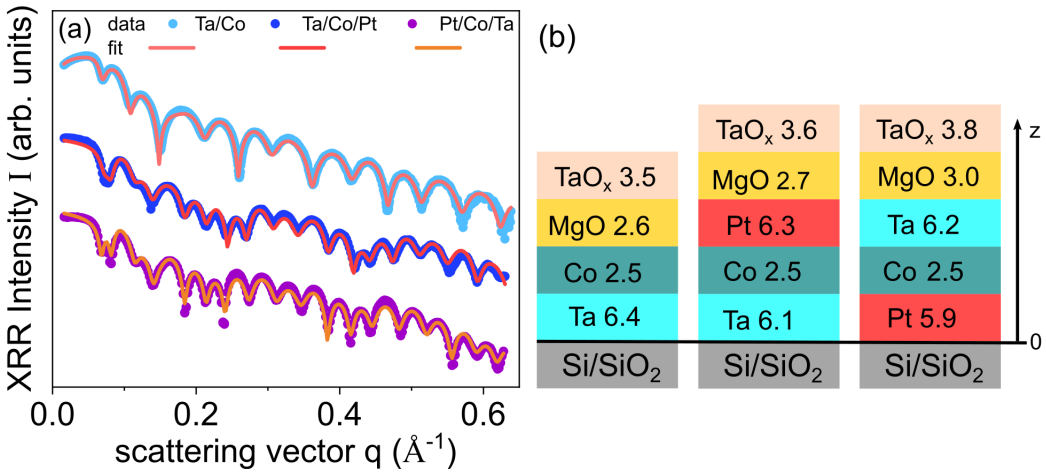

Figure 5.1: (a) XRR data and fits for the three samples. (b) Stack representations with the structural parameters obtained from the XRR fits (thicknesses in nm). Z-axis is defined vertically to the film plane with 0 being located at the substrate/stack interface.

As reported by Klewe *et al.* [132], the first step in the XRMR experimental procedure is measuring the off-resonant XRR curves to extract the structural parameters thickness, roughness and density. For the trilayers, the resonant XRR curves were obtained at a wavelength λ = 1.07192 Å (11566.5 eV), while for the Ta/Co bilayer, the off-resonant XRR was obtained by the Philips X'Pert Pro MPD x-ray diffractometer at wavelength λ = 1.5406 Å (8047.7 eV), corresponding to Cu K_α energy (see Fig. 5.1(a)). The experimental XRR curves were then fitted using the recursive Parratt algorithm [143], as described in Chapter 2. The corresponding experimental XRR curves and their fits, as well as the extracted thicknesses of the stacks are shown in Fig. 5.1(b).

To calculate the MPE-induced Pt magnetic moment, a closer look at the asymmetry ratio curves has to be taken. Figures 5.2(a)-(c) present the asymmetry ratio for the Ta/Co/Pt trilayer sample. As discussed previously in Chapter 2, one measure for the quality of the fit is the so-called goodness of fit (GOF) χ^2 value. In order to study the χ^2 dependence on various parameters, 2D χ^2 mapping [147] was performed by varying the Gaussian profile parameters, namely variance and z position, keeping the profile amplitude fixed. The χ^2 2D mapping is part of the advanced fitting procedure, developed for complex stacks, as the ones studied in this work. The obtained χ^2 map is shown in Fig. 5.2(d). By using the calculated landscape it was possible to narrow the parameter range and perform a more detailed analysis of the fits. Figures 5.2(a)-(c) show various asymmetry ratio fits obtained from different depth profile models, corresponding

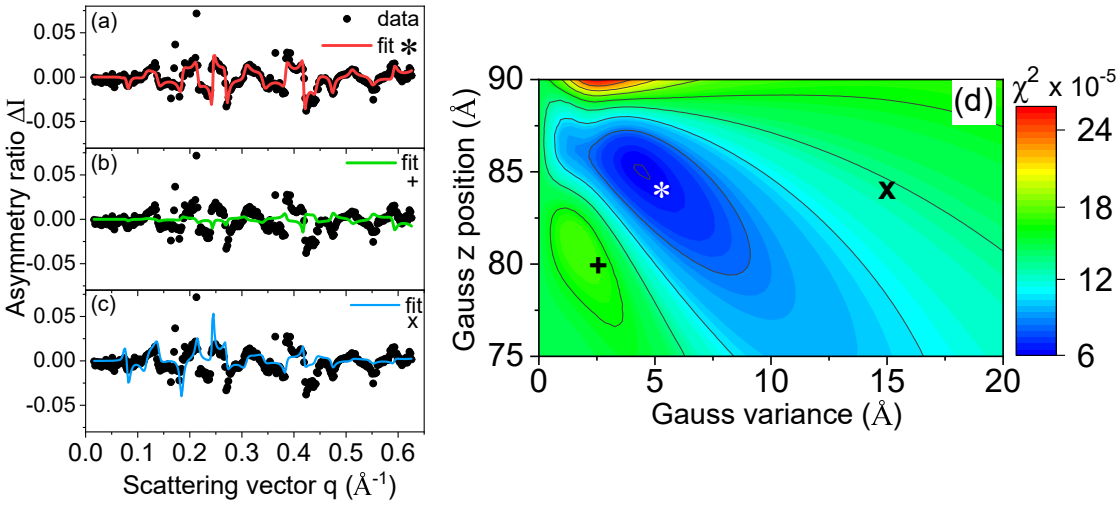

Figure 5.2: (a), (b), (c) Asymmetry ratio and various fits for the Ta/Co/Pt trilayer. (d) χ^2 map plot of the Gauss variance vs. the Gauss z position. The +, ✻ and $\times$ symbols identify the respective asymmetry ratios.

to the highlighted areas in the χ^2 landscape (the +, ✻ and $\times$ symbols). If the Gauss profile parameters (variance and z position) are chosen far from the χ^2 minimum, the resulting asymmetry ratio does not fit the experimental data neither qualitatively, nor quantitatively (Figs. 5.2(b) and (c)). For those cases, the convoluted $\Delta\beta$ depth profiles are not physically meaningful, due to the median being inside Co layer (Fig. 5.3(b) green line) or far into Pt layer (Fig. 5.3(b) light blue line). The final Gauss parameters for the best fit lie inside the global χ^2 minimum area, as shown in Figure 5.2(a), with the minimal goodness of fit χ^2 = 5.47 $\times 10^{-5}$. The physically most meaningful optic and magnetooptic profiles are presented in Fig. 5.3(a). The optic profile (solid blue line) shows the δ depth profile along the sample stack. The top TaO_x layer indicates in both cases a change of δ within the layer, which can be explained by different stages of oxidation of the metallic Ta.

A similar procedure was performed for the Pt/Co/Ta system with reversed stacking order and the resulting asymmetry ratio simulation as well as the optic and magnetooptic profiles are represented in Fig. 5.4. Here, two selected fits are shown, corresponding to different χ^2 values. Figure 5.4 (b) describes a zoomed-in region to highlight a selected asymmetry feature. One can clearly see that, even though both fits describe the experimental data rather well, the fit with higher GOF (solid green line) $\chi^2 = 16 \times 10^{-5}$ deviates stronger from the experimental data. Although both fits do not describe the experimental data perfectly, the fit with lower GOF $\chi^2 = 8.47 \times 10^{-5}$ is chosen for the further MPE analysis. As compared to the other stacking order, this modeled asymmetry ratio yields a slightly higher χ^2 value ($\chi^2_{Pt/Co/Ta}$ = 8.47 $\times 10^{-5}$ vs $\chi^2_{Ta/Co/Pt}$ =

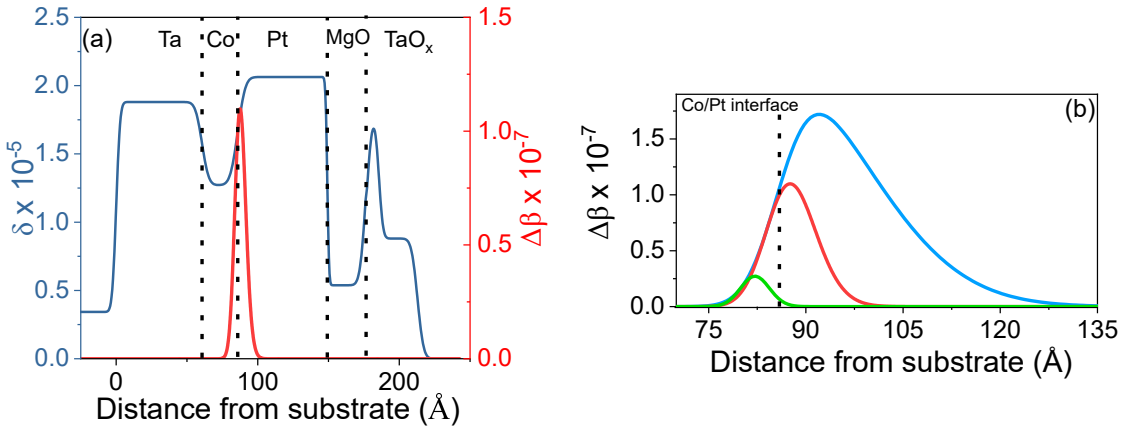

Figure 5.3: (a) Optic δ depth profile (solid blue line) and best fit magnetooptic $\Delta\beta$ depth profile (solid red line). (b) Corresponding magnetooptic Pt depth profiles from the various asymmetry ratio fits.

5.47 $\times 10^{-5}$). This might result in a higher uncertainty of $\Delta\beta$ and the final Pt magnetic moment per atom. Thus, the fit with the lowest χ^2 was chosen for further analysis.

By comparing the obtained $\Delta\beta$ values to the *ab initio* calculations, as described in detail by Kuschel *et al.* [130], the induced Pt magnetic moments of 0.56 μ_B per Pt atom at the interface for Ta/Co/Pt and 0.42 μ_B per atom at the interface for Pt/Co/Ta have been extracted. These obtained moments are comparable with the previously reported values for Pt/Fe [132] or Pt/$Co_{1-x}Fe_x$ [133] bilayers. The difference in the induced moments among the trilayers might arise due to differently textured crystal growth for Pt grown on Co compared to Pt grown on the substrate Si/SiO_2. For example, it was recently shown that different textures of Pt thin films result in a different magnitude of the MPE [134].

The extracted thicknesses of the Pt spin-polarized layer are 0.9 nm and 0.8 nm for Ta/Co/Pt and Pt/Co/Ta, respectively. These thicknesses are slightly lower than the previously reported values for the MPE in Pt/Fe bilayers [132].

5.2 Magnetic moment comparison

To understand the influence of the induced magnetism in Pt due to the MPE, this section is dedicated to the comparison of the magnetic moment values per Pt atom obtained in the previous section and the total magnetic moment of the samples measured directly via VSM.

The corresponding VSM curves are shown in Fig. 5.5, from which the saturation magnetic fields and saturation magnetic moments are extracted. It is important to note here, that the samples have different dimensions (see Table 5.1). Therefore, the resulting

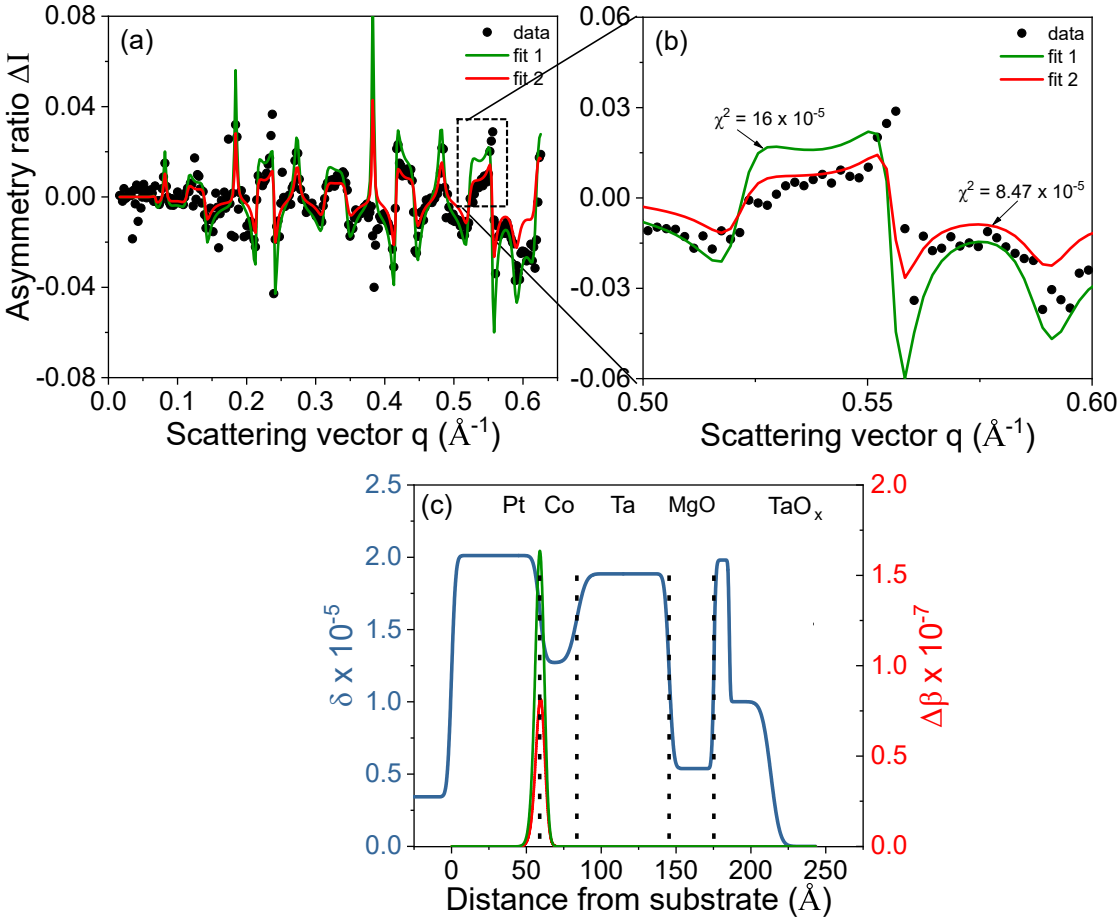

Figure 5.4: (a) Asymmetry ratio and chosen representative fits for the Pt/Co/Ta trilayer. (b) Close up of a region of the asymmetry ratio curve, comparing two fits. (c) Optic δ (solid blue line) and magnetooptic $\Delta\beta$ (solid red and green lines) depth profiles.

absolute magnetic moments μ_{VSM} in emu vary. If the MPE does not contribute to the total magnetic moment of the sample, then the measured moment should correspond to the literature value of Co for the given Co thickness and geometry of the sample. Thus, the obtained total magnetic moments are first compared to the literature value expected for Co which is 1.7 μ_{B} per Co atom according to the Slater-Pauling curve [116] (see Tab. 5.1).

For the Ta/Co reference bilayer, with no MPE, the measured magnetic moment is indeed close to the literature value and thus $\mu_{\mathrm{VSM}} = \mu_{\mathrm{Co,lit}}$. However, when comparing the trilayers containing Pt in proximity to Co, the measured magnetic moment is higher than expected for Co only. Hence, it can be concluded, that the magnetic moment in Pt is in the same direction as the Co moment, and the MPE contributes to the total magnetic moment in the case of the trilayer samples.

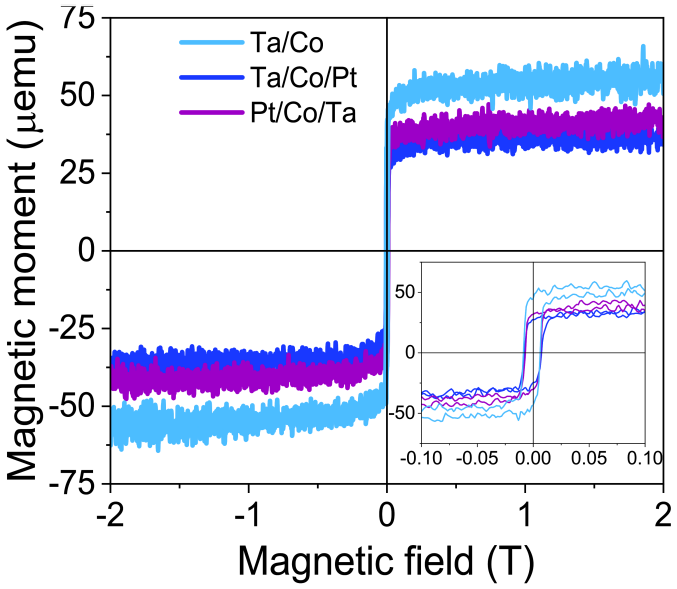

Figure 5.5: VSM hysteresis loops for the reference Ta/Co bilayer and the trilayer systems.

In order to quantitatively characterize the MPE induced magnetic moment, the extracted information is further used to recalculate the magnetic moment in μemu and to compare with the measured moment of the sample. The $\mu_{Pt} = m_{Pt} \cdot \mu_B \cdot N_{Pt}$ formula was used for the calculations, in which m_{Pt} is the moment per Pt atom in μ_B as found from the asymmetry fitting, μ_B is the Bohr magneton, $\mu_B = 9.274 \times 10^{-24}$ $\frac{J}{T}$ and N_{Pt} is the number of Pt atoms in the specific volume. N_{Pt} is then defined as

$$N_{Pt} = \frac{N_A \cdot \rho_{Pt} \cdot A \cdot t_{Pt}}{mass_{Pt}}, \tag{5.1}$$

with N_A being the Avogadro constant, $N_A = 6.022 \times 10^{23}$ mol^{-1}, ρ_{Pt} Pt density, $\rho_{Pt} = 21.45$ g/cm^3, A the sample area, t_{Pt} the thickness of the Pt spin-polarized layer as derived from the asymmetry analysis, and finally $mass_{Pt}$ corresponding to the Pt atomic mass, $mass_{Pt} = 195$ g/mol.

Using the above mentioned equations, it was found that the Pt moment is 2.8 μemu for Ta/Co/Pt trilayer, while for the reversed order trilayer it is 2.2 μemu. When these values are added to the Co literature values, the resulting moments are comparable to the measured ones (see Table 5.1). Thus, the measured magnetic moments, which are higher compared to the literature values for Co alone, can be represented as a sum of the Co moment and the induced magnetic moment of the Pt, $\mu_{\text{VSM}} = \mu_{\text{Co,lit}} + \mu_{\text{Pt,XRMR}}$.

In conclusion, it has been shown that when the MPE is present in a system, it is necessary to correctly take it into account for the total magnetic moment estimation. While

Table 5.1: Co literature values, Pt induced magnetic moments and magnetic moments measured by VSM.

Sample	A (cm^2)	$\mu_{Co,lit}$ [116] (μemu)	$\mu_{Pt,XRMR}$ (μemu)	$\mu_{Co,lit}$ + $\mu_{Pt,XRMR}$ (μemu)	μ_{VSM} (μemu)
Ta/Co	0.15 $\pm$0.04	53.6	0.0	53.6	53.0 $\pm$4.9
Ta/Co/Pt	0.09 $\pm$0.03	32.0	2.8 $\pm$1.0	34.8 $\pm$1.0	35.6 $\pm$1.1
Pt/Co/Ta	0.12 $\pm$0.04	42.8	2.2 $\pm$0.9	45.0 $\pm$0.9	44.9 $\pm$1.9

XRMR allows to probe the spin-depth profile of complex stacks, the VSM technique has been proven to aid in accessing the quantitative estimation of the induced magnetic moment of Pt. With the help of the χ^2 landscape mapping it is possible to compare different combinations of fit parameters yielding the best fit and physically consistent spin-depth profiles. The obtained magnetic moments of 0.56 μ_B and 0.42 μ_B per Pt atom at the interface are comparable to the previously reported values for simple bilayers consisting of Pt and 3d magnetic metal alloys. The calculated induced magnetic moments of the spin-polarized Pt layer correlate well with the additional increased total moment for the samples containing Pt.

CHAPTER 6

SUMMARY AND OUTLOOK

This last chapter summarizes the results obtained within this work. Several specific points are highlighted and future steps in the corresponding field are discussed.

This thesis focuses on the development of novel magnetoresistive sensors and the optimization of the known ones. The first part of this work is dedicated to the advancements in magnetoresistive sensing of magnetic nanoparticles, emphasizing the planar Hall effect sensors, due to their robustness, high sensitivity, comparably low-cost production and low noise levels. The latter was studied in detail for the applied voltages in the range of 1 to 8 V and for two different substrate materials, Si and MgO, as it was found previously that additional capacitive coupling can emerge in Si substrate itself and, thus, interfere with the sensor's output signal. Therefore, a fully insulating substrate, in this case single-crystal MgO(001), was used for the fabrication of the samples at the final stage of the work. The influence of the Hall cross width on the noise levels in PHE sensors was also investigated, where Hall crosses with the widths between 6 and 24 μm were patterned. The optimized PHE sensors exhibit noise levels as low as 2.88 nV/$\sqrt{Hz}$ (Si substrate) and 8.6 nV/$\sqrt{Hz}$ (MgO substrate) for 20 μm Hall cross width and applied ac current of 80 mA. Higher noise values for the MgO substrate were found to be related to the patterning method, as the optical lithography system was used leading to lower structure quality as compare to the e-beam lithography.

High sensitivity was achieved by adjusting the thickness of the topmost Ru layer and thus achieving almost fully compensated thin films stack. This novel method ensured near-zero sensor signal in the second harmonic in the absence of an external magnetic field, for example induced by magnetic nanoparticles. Such an approach was successfully patented [151]. Finally, the PHE sensors developed within this work were combined with the microfluidic channels, where a MNPs solution flows in close distance on top of the sensor. Ultimately, it was demonstrated that the optimized sensors with an area of 400 μm^2 are able to detect concentrations of magnetic nanoparticles down to 10^5 particles. It is possible to decrease the sensing area to 50 μm^2 for a sensor layout in a microfluidic channel. Thus, taking average numbers from the experiment, a sensor with 50 μm^2 surface area can possibly detect about 5000 MNPs with an 8 nm magnetite core.

The second part of this work is dedicated to the study of the spin Hall-based magnetoresistive effect, the so-called unidirectional spin Hall magnetoresistance, which can be potentially used for in-plane magnetization sensing, since this effect is not quadratic with the magnetization **m**, unlike other MR effects. In order to investigate the effect dependence on the thin films stack and its order, various sample systems were prepared and characterized, where a ferromagnetic material for all the samples was an in-plane magnetized Co layer with a thickness of 2.5 nm. Following the work of Avci *et al.* [97], first the bilayer systems HM/FM/cap, where HM and FM correspond to a heavy metal and ferromagnetic materials, respectively, were fabricated. After a characterization of these samples, the Hall bar design and the measurement technique were validated, since the obtained results for the USMR and SOTs correlated well with the previously reported. The main question, inspired by theoretical work of Zhang and Vignale [98], was to investigate systems with two HM/FM interfaces, and how the spintronic effects changed, when the stack order is changed. According to Zhang and Vignale, adding another HM interface to a ferromagnet would enhance the USMR effect, since it brings an additional source of spin-current injection. However, the material choice plays an important role, since the HMs must have opposite signs of SHA. The obvious HMs choice at the beginning of this work were Pt and Ta, typically demonstrating spin Hall angles of $\theta_{SH}^{Pt} \sim 10\%$ and $\theta_{SH}^{Ta} \sim$ -3%. The USMR effect in such trilayer structures, when normalized to the resistance of the HM, was proven to be indeed enhanced by about 20 % for the Pt/Co/Ta system as compared to the Pt/Co bilayer. Nevertheless, later in the work the next question arose, namely, how to increase the effect even further. Thus, the samples with W were studied, where a low resistance phase was targeted, after the reports on giant spin Hall angle values of -33% for this material [90]. The W-based systems have been characterized and a slight increase of the USMR effect ($<$ 20 %) was found as compared to Ta-based samples, studied within this work.

Additionally, a closer look at the magnetic proximity effect in the above discussed thin films systems was taken by using a synchrotron-based technique XRMR, allowing to probe magnetism of individual layers at a resonance energy of a material of interest. In this case, induced magnetism in the Pt layer via the magnetic proximity effect was studied at the Pt L_3 edge resonant energy of 11566.5 eV. The induced Pt moments of 0.56 μ_B and 0.42 μ_B per Pt atom at the interface were extracted for Ta/Co/Pt and Pt/Co/Ta samples, respectively. The extracted thickness of the spin polarized Pt layer were found to be 0.9 nm (Ta/Co/Pt) and 0.8 nm (Pt/Co/Ta), which is in good agreement with the expected values. Finally, it was found that the extracted induced magnetic moments of Pt in the studied systems correlate well with magnetic moments measured via

VSM.

As a progression of this work, final stage of the experiments is planed, where the PHE sensors in combination with microfluidics will be tested for the detection of Alzheimer's and Parkinson's biomarkers attached to MNPs in the solution, flowing through the channel. It is expected, that the aforementioned diseases' biomarkers can be found in blood or saliva samples, thus facilitating the early diagnosis procedure. Considering, that the amount of the AD and PD biomarkers in blood and saliva are significantly lower as in cerebrospinal fluid, sensing devices with extraordinary sensitivity, low noise and high robustness are required.

The work presented here on the spin Hall magnetoresistance can be a base point for the further investigations of more complex thin films structures, like multilayers, where HM_1/FM/HM_2 part repeated several times. As a continuation of this thesis, a closer look at the combination of antiferromagnetically coupled FMs and HM in one system can be studied in order to engineer a sensing device, based on USMR effect, following the first works of Avci *et al.*.

Additionally, investigation of systems with alternative materials may be necessary, since it was shown recently that Pt is associated with high global warming potential [171]. At the same time Ta and W are included in the Conflict Minerals Regulation of the European Union [172] and thus their extensive usage should be avoided.

LIST OF SCIENTIFIC CONTRIBUTIONS

Peer-reviewed Publications:

1. **A. Moskaltsova**, J. Krieft, D. Graulich, T. Matalla-Wagner and T. Kuschel, *"Impact of the magnetic proximity effect in Pt on the total magnetic moment of Pt/Co/Ta trilayers studied by x-ray resonant magnetic reflectivity"*, AIP Advances, 10, 015154 (2020) (**Editor's Pick**) — **Finalist Advances in Magnetism Award**

2. J. Krieft, D. Graulich, **A. Moskaltsova**, L. Bouchenoire, S. Francoual, and T. Kuschel, *"Advantages and limits of hard x-ray resonant magnetic reflectivity discussed for Pt thin film samples of various complexity"*, Journal of Physics D: Applied Physics, 53, 375004 (2020)

3. D. Graulich, J. Krieft, **A. Moskaltsova**, J. Demir, T. Peters, T. Pohlmann, J. Wollschläger, J.R. Linares Mardegan, S. Francoual and T. Kuschel, *"Quantitative comparison of the magnetic proximity effect in Pt detected by XRMR and XMCD"*, Applied Physics Letters, 118, 012407 (2021)

4. A. Elzwawy, H. Pişkin,N. Akdoğan, M. Volmer, G. Reiss, L. Marnitz, **A. Moskaltsova**, O. Gurel, J.- M. Schmalhorst ,*"Current trends in planar Hall effect sensors: evolution, optimization and applications*, Journal of Physics D Applied Physics, 54, 353002 (2021)

5. **A. Moskaltsova**, L. Marnitz, J.-M. Schmalhorst, and G. Reiss, *"Influence of the substrate material on the noise in PHE sensors"* (in preparation)

6. **A. Moskaltsova**, D. Dyck, J.-M. Schmalhorst, G. Reiss, and T. Kuschel, *"Influence of the stack modification on the unidirectional spin Hall magnetoresistance and spin-orbit torques in HM_1/Co/HM_2 trilayer systems"* (in preparation)

Patents:

1. G. Reiss, J.-M. Schmalhorst, L. S. Marnitz, **A. Moskaltsova**, G. Maruccio, DE 10 2019 121 379.7 "Vorrichtung und Verfahren zum Detektieren von magnetischen Partikeln", issued on 11.02.2021

Book chapters:

1. G. Reiss, L. Marnitz, **A. Moskaltsova**, and J.-M. Schmalhorst, Subchapter 9.1 "Magnetic biosensors" in *"Nanomagnetic Materials"*, ed. A. Yamaguchi, A. Hirohata and B. Stadler, Micro and Nano Technologies (Elsevier, 2021), pp.623-637.

Conferences:

1. Oral presentation at the **64th Conference on Magnetism and Magnetic Materials MMM-2019**, Las Vegas, USA (November 2019)
2. Oral presentation at the **Magnetooptic workshop**, Bielefeld, Germany (September 2019)
3. Poster at the **MagFrontiers**, Lisbon, Portugal (June 2019)
4. Poster at the **Nanotechnologies and Smart Systems for Early Diagnostics Workshop**, Bologna, Italy (June 2019)
5. Poster at the **X Spin Caloritronics**, Groningen, the Netherlands (May 2019)
6. Poster at the **83rd DPG Spring meeting**, Regensburg, Germany (April 2019)
7. Poster at the **Synchrotron Radiation School**, Mittelhwihr, France (October 2018)
8. Poster at the **International Conference on Magnetism (ICM)**, San Francisco, USA (July 2018)
9. Poster at the **82nd DPG Spring meeting**, Berlin, Germany (March 2018)
10. Poster at the **DESY Photon Science user meeting**, Hamburg, Germany (January 2018)

BIBLIOGRAPHY

[1] W. Suchowerskyj, B. Seibel, and P. Werner, *United states patent, test circuit for automotive passenger restraint systems*, 1981.

[2] B. Ording, M. van Os, and I. Chaudhri, *Screen rotation gestures on a portable multifunction device, United States patent*, 2007.

[3] M. Li, V. T. Rouf, M. J. Thompson, and D. A. Horsley, "Three-axis Lorentz-force magnetic sensor for electronic compass applications", J. Microelectromech. Syst. **21**, 1002–1010 (2012).

[4] J. Wu, Z. Zhou, H. Fourati, and Y. Cheng, "A super fast attitude determination algorithm for consumer-level accelerometer and magnetometer", IEEE Trans. Consum. Electron. **64**, 375–381 (2018).

[5] N. Tyler, *Safe and secure*, `www.newelectronics.co.uk`, 2016.

[6] P. Kleinschmidt and F. Schmidt, "How many sensors does a car need?", Sens. Actuator A Phys. **31**, Proceedings of Eurosensors V, 35–45 (1992).

[7] A. M. R. Patil Asavari, *Global sensor market: opportunities and forecast, 2019-2025*, 2020.

[8] M. Chhabra and A. M. R. Patil Asavari, *Magnetic sensor market by type (hall effect sensor, magnetoresistive sensor, squid sensor, and fluxgate sensor), application (speed sensing, detection, position sensing, navigation, and others), and end user (consumer electronics, automotive, industrial, aerospace defense, healthcare, and others): global opportunity analysis and industry forecast, 2019–2026*, 2020.

[9] C. Datlinger and M. Hirz, "Benchmark of rotor position sensor technologies for application in automotive electric drive trains", Electronics (Switzerland) **9**, 1–29 (2020).

[10] *KMT32B magnetic angle sensor Data Sheet*, TE Connectivity, 2017.

[11] A. S. Almansouri, N. A. Alsharif, M. A. Khan, L. Swanepoel, A. Kaidarova, K. N. Salama, and J. Kosel, "An imperceptible magnetic skin", Adv. Mater. Technol. **4**, 1900493 (2019).

[12] P. P. Freitas, F. A. Cardoso, V. C. Martins, S. A. Martins, J. Loureiro, J. Amaral, R. C. Chaves, S. Cardoso, L. P. Fonseca, A. M. Sebastião, M. Pannetier-Lecoeur, and C.

Fermon, "Spintronic platforms for biomedical applications", Lab on a Chip **12**, 546–557 (2012).

[13]X. Zhou, M. Sveiven, and D. A. Hall, "A CMOS Magnetoresistive Sensor Front-End With Mismatch-Tolerance and Sub-ppm Sensitivity for Magnetic Immunoassays", IEEE Trans. Biomed. Circuits Syst. **13**, 1254–1263 (2019).

[14]M. Melzer, D. Makarov, A. Calvimontes, D. Karnaushenko, S. Baunack, R. Kaltofen, Y. Mei, and O. G. Schmidt, "Stretchable magnetoelectronics", Nano Lett. **11**, 2522–2526 (2011).

[15]D. Makarov, M. Melzer, D. Karnaushenko, and O. G. Schmidt, "Shapeable magnetoelectronics", Appl. Phys. Rev. **3**, 011101 (2016).

[16]M. Kim, S. Oh, W. Jeong, A. Talantsev, T. Jeon, R. Chaturvedi, S. Lee, and C. Kim, "Highly Bendable Planar Hall Resistance Sensor", IEEE Magn. Lett. **11**, 4100705 (2020).

[17]V. Renaudin and C. Combettes, "Magnetic, acceleration fields and gyroscope quaternion (MAGYQ)-based attitude estimation with smartphone sensors for indoor pedestrian navigation", Sensors (Switzerland) **14**, 22864–22890 (2014).

[18]S. Sordo-Ibanez, B. Pinero-Garcia, M. Munoz-Diaz, A. Ragel-Morales, J. Ceballos-Caceres, L. Carranza-Gonzalez, S. Espejo-Meana, A. Arias-Drake, J. Ramos-Martos, J. M. Mora-Gutierrez, and M. A. Lagos-Florido, "A front-end ASIC for a 3-d magnetometer for space applications by using anisotropic magnetoresistors", IEEE Trans. Magn. **51**, 4001804 (2015).

[19]D. M. Miles, I. R. Mann, M. Ciurzynski, D. Barona, B. B. Narod, J. R. Bennest, I. P. Pakhotin, A. Kale, B. Bruner, C. D. Nokes, C. Cupido, T. Haluza-DeLay, D. G. Elliott, and D. K. Milling, "A miniature, low-power scientific fluxgate magnetometer: A stepping-stone to cube-satellite constellation missions", J. Geophys. Res. Space Phys. **121**, 11,839–11,860 (2016).

[20]K. M. C. Fu, G. Z. Iwata, A. Wickenbrock, and D. Budker, "Sensitive magnetometry in challenging environments", AVS Quantum Sci. **2**, 044702 (2020).

[21]*EU Horizon 2020 MADIA Project*, `http://www.madia-project.eu/`.

[22]*World Alzheimer Report 2018. The state of the art of dementia research: New frontiers* (Alzheimer's Disease International (ADI), London, 2018).

[23]C. O. Avci, A. Quindeau, C. F. Pai, M. Mann, L. Caretta, A. S. Tang, M. C. Onbasli, C. A. Ross, and G. S. Beach, "Current-induced switching in a magnetic insulator", Nat. Mater. **16**, 309–314 (2017).

[24]C. O. Avci, M. Mann, A. J. Tan, P. Gambardella, and G. S. Beach, "A multi-state memory device based on the unidirectional spin Hall magnetoresistance", Appl. Phys. Lett. **110**, 203506 (2017).

[25]T. McGuire and R. Potter, "Anisotropic magnetoresistance in ferromagnetic 3d alloys", IEEE Trans. Magn. **11**, 1018–1038 (1975).

[26]P. P. Freitas, R. Ferreira, S. Cardoso, and F. Cardoso, "Magnetoresistive sensors", J. Phys. Condens. Matter **19**, 165221 (2007).

[27]Alzheimer's Association, "Alzheimer 's Disease Facts and Figures in California", Alzeheimer's & Dementia **15**, 321–387 (2019).

[28]E. Nichols, C. E. Szoeke, S. E. Vollset, N. Abbasi, F. Abd-Allah, J. Abdela, M. T. E. Aichour, R. O. Akinyemi, F. Alahdab, S. W. Asgedom, and A. Awasthi *et al.*, "Global, regional, and national burden of Alzheimer's disease and other dementias, 1990-2016: a systematic analysis for the Global Burden of Disease Study 2016", The Lancet Neurology **18**, 88–106 (2019).

[29]J. Jankovic, "Parkinson's disease: Clinical features and diagnosis", J. Neurol. Neurosurg. Psychiatry **79**, 368–376 (2008).

[30]E. Tolosa, G. Wenning, and W. Poewe, "The diagnosis of Parkinson's disease", Lancet Neurology **5**, 75–86 (2006).

[31]B. Thomas and M. Flint Beal, "Parkinson's disease", Hum. Mol. Genet. **16**, 183–194 (2007).

[32]B. N. Engel, J. Akerman, B. Butcher, R. W. Dave, M. DeHerrera, M. Durlam, G. Grynkewich, J. Janesky, S. V. Pietambaram, N. D. Rizzo, J. M. Slaughter, K. Smith, J. J. Sun, and S. Tehran, "A 4-Mb toggle MRAM based on a novel bit and switching method", IEEE Trans. Magn. **41**, 132–136 (2005).

[33]W. Zhao, E. Belhaire, C. Chappert, and P. Mazoyer, "Spin transfer torque (STT)-MRAM - Based runtime reconfiguration FPGA circuit", ACM Trans. Embed. Comput. Syst. **9**, 14 (2009).

[34]D. Apalkov, A. Khvalkovskiy, S. Watts, V. Nikitin, X. Tang, D. Lottis, K. Moon, X. Luo, E. Chen, A. Ong, A. Driskill-Smith, and M. Krounbi, "Spin-Transfer Torque Magnetic Random Access Memory (STT-MRAM)", J. Emerg. Technol. Comput. Syst. **9**, 13 (2013).

[35]W. Thomson, "On the electro-dynamic qualities of metals:—effects of magnetization on the electric conductivity of Nickel and of Iron", Proc. Royal Soc. Lond. **8**, 546–550 (1857).

[36]K. Sato and E. Saitoh, *Spintronics for next generation innovative devices* (John Wiley Sons, Ltd, 2015).

[37]K. M. Seemann, F. Freimuth, H. Zhang, S. Blügel, Y. Mokrousov, D. E. Bürgler, and C. M. Schneider, "Origin of the planar Hall effect in nanocrystalline $Co_{60}Fe_{20}B_{20}$", Phys. Rev. Lett. **107**, 086603 (2011).

[38]S. Kokado, M. Tsunoda, K. Harigaya, and A. Sakuma, "Anisotropic Magnetoresistance Effects in Fe, Co, Ni, Fe_4N, and Half-Metallic Ferromagnet: A Systematic Analysis", J. Phys. Soc. Jpn. **81**, 024705 (2012).

[39]K. L. Yau and J. T. Chang, "The planar Hall effect in thin foils of Ni-Fe alloy", J. Phys. F: Met. Phys. **1**, 38–43 (1971).

[40]I. A. Campbell, A. Fert, and O. Jaoul, "The spontaneous resistivity anisotropy in Ni-based alloys", J. Phys. Condens. Matter **3**, S95–S101 (1970).

[41]A. Grosz, V. Mor, S. Amrusi, I. Faivinov, E. Paperno, and L. Klein, "A High-Resolution Planar Hall Effect Magnetometer for Ultra-Low Frequencies", IEEE Sensors Journal **16**, 3224–3230 (2016).

[42]M. Volmer and M. Avram, "Electrical characterization of magnetoresistive sensors based on AMR and GMR effects used for lab-on-a-chip applications", Rev. Adv. Mater. Sci. **15**, 220–224 (2007).

[43]D. Y. Kim, B. S. Park, and C. G. Kim, "Optimization of planar Hall resistance using biaxial currents in a NiO/NiFe bilayer: Enhancement of magnetic field sensitivity", J. Appl. Phys. **88**, 3490–3494 (2000).

[44]A. P. Malozemoff, "Anisotropic magnetoresistance of amorphous and concentrated polycrystalline iron alloys", Phys. Rev. B **32**, 6080–6083 (1985).

[45]M. N. Baibich, J. M. Broto, A. Fert, F. N. Van Dau, F. Petroff, P. Etienne, G. Creuzet, A. Friederich, and J. Chazelas, "Giant Magnetoresistance of (001)Fe/(001)Cr Magnetic Superlattices", Phys. Rev. Lett. **61**, 2472–2475 (1988).

[46]G. Binasch, P. Grünberg, F. Saurenbach, and W. Zinn, "Enhanced magnetoresistance in layered magnetic structures with antiferromagnetic interlayer exchange", Phys. Rev. B **39**, 4828–4830 (1989).

[47]M. A. Ruderman and C. Kittel, "Indirect exchange coupling of nuclear magnetic moments by conduction electrons", Phys. Rev. **96**, 99–102 (1954).

[48]T. Kasuya, "A Theory of Metallic Ferro- and Antiferromagnetism on Zener's Model", Prog. Theor. Phys. **16**, 45–57 (1956).

[49]K. Yosida, “Magnetic Properties of Cu-Mn Alloys”, Phys. Rev. **106**, 893–898 (1957).

[50]S. S. P. Parkin and D. Mauri, “Spin engineering: Direct determination of the Ruderman-Kittel-Kasuya-Yosida far-field range function in ruthenium”, Phys. Rev. B **44**, 7131–7134 (1991).

[51]N. F. Mott, “The electrical conductivity of transition metals”, Proc. Math. Phys. Sci. **153**, 699–717 (1936).

[52]S. A. Wolf, D. D. Awschalom, R. A. Buhrman, J. M. Daughton, S. von Molnar, M. L. Roukes, A. Y. Chtchelkanova, and D. M. Treger, “Spintronics: A Spin-Based Electronics Vision for the Future”, Science **294**, 1488–1495 (2001).

[53]R. Weiss, R. Mattheis, and G. Reiss, “Advanced giant magnetoresistance technology for measurement applications”, Meas. Sci. Technol. **24**, 082001 (2013).

[54]M. Johnson, *Magnetoelectronics* (2004), pp. 67–150.

[55]T. Shinjo and H. Yamamoto, “Large magnetoresistance of field-induced giant ferrimagnetic multilayers”, J. Phys. Soc. Jpn. **59**, 3061–3064 (1990).

[56]B. Dieny, V. S. Speriosu, S. Metin, S. S. P. Parkin, B. A. Gurney, P. Baumgart, and D. R. Wilhoit, “Magnetotransport properties of magnetically soft spin-valve structures”, J. Appl. Phys. **69**, 4774–4779 (1991).

[57]M. Julliere, “Tunneling between ferromagnetic films”, Phys. Lett. A **54**, 225 –226 (1975).

[58]S. Maekawa and U. Gafvert, “Electron tunneling between ferromagnetic films”, IEEE Trans. Magn. **18**, 707–708 (1982).

[59]J. S. Moodera, L. R. Kinder, T. M. Wong, and R. Meservey, “Large magnetoresistance at room temperature in ferromagnetic thin film tunnel junctions”, Phys. Rev. Lett. **74**, 3273–3276 (1995).

[60]T. Miyazaki and N. Tezuka, “Giant magnetic tunneling effect in fe/al2o3/fe junction”, Journal of Magnetism and Magnetic Materials **139**, L231–L234 (1995).

[61]S. Knudde, G. Farinha, D. C. Leitao, R. Ferreira, S. Cardoso, and P. P. Freitas, “AlO_x barrier growth in magnetic tunnel junctions for sensor applications”, J. Magn. Magn. Mater. **412**, 181–184 (2016).

[62]X. Liu and G. Xiao, “Thermal annealing effects on low-frequency noise and transfer behavior in magnetic tunnel junction sensors”, J. Appl. Phys. **94**, 6218–6220 (2003).

[63]H. X. Wei, Q. H. Qin, M. Ma, R. Sharif, and X. F. Han, "80% tunneling magnetoresistance at room temperature for thin Al-O barrier magnetic tunnel junction with CoFeB as free and reference layers", J. Appl. Phys. **101**, 09B501 (2007).

[64]S. Ikeda, J. Hayakawa, Y. Ashizawa, Y. M. Lee, K. Miura, H. Hasegawa, M. Tsunoda, F. Matsukura, and H. Ohno, "Tunnel magnetoresistance of 604% at 300 K by suppression of Ta diffusion in CoFeBMgOCoFeB pseudo-spin-valves annealed at high temperature", Appl. Phys. Lett. **93**, 082508 (2008).

[65]S. Yuasa and D. D. Djayaprawira, "Giant tunnel magnetoresistance in magnetic tunnel junctions with a crystalline MgO(0 0 1) barrier", J. Phys. D: Appl. Phys. **40**, R337–R354 (2007).

[66]O. Schebaum, V. Drewello, A. Auge, G. Reiss, M. Mnzenberg, H. Schuhmann, M. Seibt, and A. Thomas, "Tunnel magnetoresistance in alumina, magnesia and composite tunnel barrier magnetic tunnel junctions", J. Magn. Magn. Mater. **323**, 1525–1528 (2011).

[67]J. G. Webster, S. Peng, Y. Zhang, M. Wang, Y. Zhang, and W. Zhao, "Magnetic Tunnel Junctions for Spintronics: Principles and Applications", Wiley Encyclopedia of Electrical and Electronics Engineering **1936**, 1–16 (2014).

[68]D. Ebke, J. Schmalhorst, N. N. Liu, A. Thomas, G. Reiss, and A. Hütten, "Large tunnel magnetoresistance in tunnel junctions with Co_2MnSi/Co_2FeSi multilayer electrode", Appl. Phys. Lett. **89**, 162506 (2006).

[69]C. Sterwerf, M. Meinert, J. M. Schmalhorst, and G. Reiss, "High TMR ratio in Co_2FeSi and Fe_2CoSi based magnetic tunnel junctions", IEEE Trans. Magn. **49**, 4386–4389 (2013).

[70]J. Jeong, Y. Ferrante, S. V. Faleev, M. G. Samant, C. Felser, and S. S. P. Parkin, "Termination layer compensated tunnelling magnetoresistance in ferrimagnetic Heusler compounds with high perpendicular magnetic anisotropy", Nat. Commun. **7**, 10276 (2016).

[71]C. Zheng, K. Zhu, S. C. De Freitas, J. Y. Chang, J. E. Davies, P. Eames, P. P. Freitas, O. Kazakova, C. G. Kim, and C. W. Leung *et al.*, "Magnetoresistive Sensor Development Roadmap (Non-Recording Applications)", IEEE Trans. Magn. **55**, 0800130 (2019).

[72]G. Vasilescu, *Electronic Noise and Interfering Signals* (Springer, Berlin, Heidelberg, 2005).

[73]F. N. Hooge and A. M. H. Hoppenbrouwres, "1/f Noise in Continuous Thin Gold Films", Physica **45**, 386–392 (1969).

[74]J. B. Johnson, “Thermal agitation of electricity in conductors”, Phys. Rev. **32**, 97–109 (1928).

[75]H. Nyquist, “Thermal agitation of electric charge in conductors”, Phys. Rev. **32**, 110–113 (1928).

[76]W. Schottky, “Über spontane Stromschwankungen in verschiedenen Elektrizitätsleitern”, Annalen der Physik **362**, 541–567 (1918).

[77]I. Ahmed, Z. Zhao, M. G. Mankalale, S. S. Sapatnekar, J.-P. Wang, and C. H. Kim, “A Comparative Study Between Spin-Transfer-Torque and Spin-Hall-Effect Switching Mechanisms in PMTJ Using SPICE”, IEEE J. Explor. Solid-State Computat. Devices Circuits **3**, 74–82 (2017).

[78]M. Kharbouche-Harrari, R. Alhalabi, J. Postel-Pellerin, R. Wacquez, D. Aboulkassimi, E. Nowak, I. L. Prejbeanu, G. Prenat, and G. D. Pendina, “MRAM: from STT to SOT, for security and memory”, in 2018 conference on design of circuits and integrated systems (dcis) (2018), pp. 1–6.

[79]A. Manchon, I. M. Miron, T. Jungwirth, J. Sinova, J. Zelezny, A. Thiaville, K. Garello, and P. Gambardella, “Current-induced spin-orbit torques in ferromagnetic and antiferromagnetic systems”, Rev. Mod. Phys. **91**, 035004 (2019).

[80]E. H. Hall, “On a new action of the magnet on electric currents”, Am. J. Math. **2**, 287–292 (1879).

[81]A. Hoffmann, “Spin Hall effects in metals”, IEEE Trans. Magn. **49**, 5172–5193 (2013).

[82]M. Dyakonov and V. Perel, “Current-induced spin orientation of electrons in semiconductors”, Phys. Lett. A **35**, 459 (1971).

[83]J. N. Chazalviel and I. Solomon, “Experimental Evidence of the Anomalous Hall Effect in a Nonmagnetic Semiconductor”, Phys. Rev. Lett. **29**, 1676–1679 (1972).

[84]J.-N. Chazalviel, “Spin-dependent Hall effect in semiconductors”, Phys. Rev. B **11**, 3918–3934 (1975).

[85]J. E. Hirsch, “Spin Hall effect”, Phys. Rev. Lett. **83**, 1834 (1999).

[86]S. Zhang, “Spin hall effect in the presence of spin diffusion”, Phys. Rev. Lett. **85**, 393–396 (2000).

[87]Y. K. Kato, R. C. Myers, A. C. Gossard, and D. D. Awschalom, “Observation of the spin Hall effect in semiconductors”, Science **306**, 1910–1913 (2004).

[88]J. Wunderlich, B. Kaestner, J. Sinova, and T. Jungwirth, "Experimental observation of the spin-hall effect in a two-dimensional spin-orbit coupled semiconductor system", Phys. Rev. Lett. **94**, 047204 (2005).

[89]J. Sinova, S. O. Valenzuela, J. Wunderlich, C. H. Back, and T. Jungwirth, "Spin hall effects", Rev. Mod. Phys. **87**, 1213–1260 (2015).

[90]C.-F. Pai, L. Liu, Y. Li, H. W. Tseng, D. C. Ralph, and R. A. Buhrman, "Spin transfer torque devices utilizing the giant spin Hall effect of tungsten", Appl. Phys. Lett. **101**, 122404 (2012).

[91]E. Sagasta, Y. Omori, M. Isasa, M. Gradhand, L. E. Hueso, Y. Niimi, Y. Otani, and F. Casanova, "Tuning the spin Hall effect of Pt from the moderately dirty to the superclean regime", Phys. Rev. B **94**, 060412(R) (2016).

[92]K. Fritz, S. Wimmer, H. Ebert, and M. Meinert, "Large spin Hall effect in an amorphous binary alloy", Phys. Rev. B **98**, 094433 (2018).

[93]L. Ma, L. Lang, J. Kim, Z. Yuan, R. Wu, S. Zhou, and X. Qiu, "Spin diffusion length and spin Hall angle in $Pd_{1-x}Pt_x$/YIG heterostructures: Examination of spin relaxation mechanism", Phys. Rev. B **98**, 224424 (2018).

[94]M. Weiler, M. Althammer, F. D. Czeschka, H. Huebl, M. S. Wagner, M. Opel, I. M. Imort, G. Reiss, A. Thomas, R. Gross, and S. T. Goennenwein, "Local charge and spin currents in magnetothermal landscapes", Phys. Rev. Lett. **108**, 106602 (2012).

[95]Y.-T. Chen, S. Takahashi, H. Nakayama, M. Althammer, S. Goennenwein, E. Saitoh, and G. Bauer, "Theory of spin Hall magnetoresistance", Phys. Rev. B **87**, 144411 (2013).

[96]S. Y. Huang, X. Fan, D. Qu, Y. P. Chen, W. G. Wang, J. Wu, T. Y. Chen, J. Q. Xiao, and C. L. Chien, "Transport magnetic proximity effects in platinum", Phys. Rev. Lett. **109**, 107204 (2012).

[97]C. O. Avci, K. Garello, A. Ghosh, M. Gabureac, S. F. Alvarado, and P. Gambardella, "Unidirectional spin Hall magnetoresistance in ferromagnet/normal metal bilayers", Nat. Phys. **11**, 570–575 (2015).

[98]S. S. Zhang and G. Vignale, "Theory of unidirectional spin Hall magnetoresistance in heavy-metal / ferromagnetic-metal bilayers", Phys. Rev. B **94**, 140411(R) (2016).

[99]Y. Yin, D. S. Han, M. C. De Jong, R. Lavrijsen, R. A. Duine, H. J. Swagten, and B. Koopmans, "Thickness dependence of unidirectional spin-Hall magnetoresistance in metallic bilayers", Appl. Phys. Lett. **111**, 232405 (2017).

[100]I. M. Miron, G. Gaudin, S. Auffret, B. Rodmacq, A. Schuhl, S. Pizzini, J. Vogel, and P. Gambardella, "Current-driven spin torque induced by the Rashba effect in a ferromagnetic metal layer", Nat. Mat. **9**, 230–234 (2010).

[101]I. M. Miron, K. Garello, G. Gaudin, P.-J. Zermatten, M. V. Costache, S. Auffret, S. Bandiera, B. Rodmacq, A. Schuhl, and P. Gambardella, "Perpendicular switching of a single ferromagnetic layer induced by in-plane current injection", Nature (London) **476**, 189–193 (2011).

[102]P. Gambardella and I. M. Miron, "Current-induced spin-orbit torques", Phil. Trans. R. Soc. **369**, 3175–3197 (2011).

[103]L. Liu, O. J. Lee, T. J. Gudmundsen, D. C. Ralph, and R. A. Buhrman, "Current-induced switching of perpendicularly magnetized magnetic layers using spin torque from the spin Hall effect", Phys. Rev. Lett. **109**, 096602 (2012).

[104]J. Slonczewski, "Current-driven excitation of magnetic multilayers", J. Magn. Magn. Mater. **159**, L1 –L7 (1996).

[105]Y. C. Lau and M. Hayash, "Spin torque efficiency of Ta, W, and Pt in metallic bilayers evaluated by harmonic Hall and spin Hall magnetoresistance measurements", Jpn. J. Appl. Phys. **56**, 0802B5 (2017).

[106]E. C. Stoner, "Collective electron ferronmagnetism", Proc. R. Soc. Lond. A **165**, 372 (1938).

[107]S. Rüegg, G. Schütz, P. Fischer, R. Wienke, W. B. Zeper, and H. Ebert, "Spin-dependent x-ray absorption in Co/Pt multilayers", J. Appl. Phys. **69**, 5655–5657 (1991).

[108]J. Vogel, A. Fontaine, V. Cros, F. Petroff, J.-P. Kappler, G. Krill, A. Rogalev, and J. Goulon, "Structure and magnetism of Pd in Pd/Fe multilayers studied by x-ray magnetic circular dichroism at the Pd $L_{2,3}$ edges", Phys. Rev. B **55**, 3663–3669 (1997).

[109]T. P. A. Hase, M. S. Brewer, U. B. Arnalds, M. Ahlberg, V. Kapaklis, M. Björck, L. Bouchenoire, P. Thompson, D. Haskel, Y. Choi, J. Lang, C. Sánchez-Hanke, and B. Hjörvarsson, "Proximity effects on dimensionality and magnetic ordering in Pd/Fe/Pd trialyers", Phys. Rev. B **90**, 104403 (2014).

[110]M. M. Schwickert, R. Coehoorn, M. A. Tomaz, E. Mayo, D. Lederman, W. L. O'Brien, T. Lin, and G. R. Harp, "Magnetic moments, coupling, and interface interdiffusion in Fe/V(001) superlattices", Phys. Rev. B **57**, 13681–13691 (1998).

[111]A. Scherz, P. Poulopoulos, H. Wende, G. Ceballos, K. Baberschke, and F. Wilhelm, "Thickness dependence of the V induced magnetic moment in Fe/V/Fe(110) trilayers", J. Appl. Phys. **91**, 8760–8762 (2002).

[112]M. M. Schwickert, G. Y. Guo, M. A. Tomaz, W. L. O'Brien, and G. R. Harp, "X-ray magnetic linear dichroism in absorption at the L edge of metallic Co, Fe, Cr, and V", Phys. Rev. B **58**, R4289–R4292 (1998).

[113]T. Lin, M. A. Tomaz, M. M. Schwickert, and G. R. Harp, "Structure and magnetic properties of Ru/Fe(001) multilayers", Phys. Rev. B **58**, 862–868 (1998).

[114]F. Nasirpouri and A. Nogaret, *Nanomagnetism and spintronics : fabrication, materials, characterization and applications* (Singapore ; Hackensack, NJ : World Scientific, 2011).

[115]W. Heisenberg, "Zur Theorie des Ferromagnetismus", Zeitschrift für Physik **49**, 619–636 (1928).

[116]S. Chikazumi, *Physics of ferromagnetism* (Oxford University Press, Oxford, 1997).

[117]W. Pauli, "Über den Zusammenhang des Abschlusses der Elektronengruppen im Atom mit der Komplexstruktur der Spektren", Zeitschrift für Physik **31**, 765–783 (1925).

[118]M. M. Sigalas and D. A. Papaconstantopoulos, "Calculations of the total energy, electron-phonon interaction and Stoner parameter in the 5d transition metal hydrides", Phys. Rev. B **50**, 7255 (1994).

[119]G. van der Laan, B. T. Thole, G. A. Sawatzky, J. B. Goedkoop, J. C. Fuggle, J.-M. Esteva, R. Karnatak, J. P. Remeika, and H. A. Dabkowska, "Experimental proof of magnetic x-ray dichroism", Phys. Rev. B **34**, 6529–6531 (1986).

[120]G. Schütz, W. Wagner, W. Wilhelm, P. Kienle, R. Zeller, R. Frahm, and G. Materlik, "Absorption of circularly polarized x-rays in iron", Phys. Rev. Lett. **58**, 737–740 (1987).

[121]G. Schütz, R. Wienke, W. Wilhelm, W. Wagner, R. Frahm, and P. Kienle, "Spin-dependent absorption at the K- and $La_{2,3}$- edges in ferromagnetic $Fe_{50}Pt_{20}$ alloy", Physica B **158**, 284–286 (1989).

[122]G. Schütz, R. Wienke, W. Wilhelm, W. B. Zeper, H. Ebert, and K. Spörl, "Spin-dependent x-ray absorption in Co/Pt multilayers and $Co_{50}Pt_{50}$ alloy", J. Appl. Phys. **67**, 4456–4458 (1990).

[123]W. J. Antel, M. M. Schwickert, T. Lin, W. L. O'Brien, and G. R. Harp, "Induced ferromagnetism and anisotropy of Pt layers in Fe/Pt(001) multilayers", Phys. Rev. B **60**, 12933–12940 (1999).

[124]F. Wilhelm, P. Poulopoulos, A. Scherz, H. Wende, K. Baberschke, M. Angelakeris, N. K. Flevaris, J. Goulon, and A. Rogalev, "Interface magnetism in 3d/5d multilayers probed by x-ray magnetic circular dichroism", Phys. Status Solidi A **196**, 33–36 (2003).

[125]J. B. Goedkoop, J. C. Fuggle, B. T. Thole, G. van der Laan, and G. A. Sawatzky, "Magnetic x-ray dichroism of rare-earth materials", J. Appl. Phys. **64**, 5595–5597 (1988).

[126]C. T. Chen, F. Sette, Y. Ma, and S. Modesti, "Soft-x-ray magnetic circular dichroism at the $L_{2,3}$ edges of nickel", Phys. Rev. B **42**, 7262–7265 (1990).

[127]J. Geissler, E. Goering, M. Justen, F. Weigand, G. Schütz, J. Langer, D. Schmitz, H. Maletta, and R. Mattheis, "Pt magnetization profile in a Pt/Co bilayer studied by resonant magnetic x-ray reflectometry", Phys. Rev. B **65**, 020405 (2001).

[128]S. Macke and E. Goering, "Magnetic reflectometry of heterostructures", J. Phys.: Condens. Matter **26**, 363201 (2014).

[129]D. Graulich, J. Krieft, A. Moskaltsova, J. Demir, T. Peters, T. Pohlmann, F. Bertram, J. Wollschläger, J. R. L. Mardegan, S. Francoual, and T. Kuschel, "Quantitative comparison of the magnetic proximity effect in Pt detected by XRMR and XMCD", Appl. Phys. Lett. **118**, 012407 (2021).

[130]T. Kuschel, C. Klewe, J.-M. Schmalhorst, F. Bertram, O. Kuschel, T. Schemme, J. Wollschläger, S. Francoual, J. Strempfer, A. Gupta, M. Meinert, G. Götz, D. Meier, and G. Reiss, "Static magnetic proximity effect in Pt/$NiFe_2O_4$ and Pt/Fe bilayers investigated by x-ray resonant magnetic reflectivity", Phys. Rev. Lett. **115**, 097401 (2015).

[131]T. Kuschel, C. Klewe, P. Bougiatioti, O. Kuschel, J. Wollschläger, L. Bouchenoire, S. D. Brown, J.-M. Schmalhorst, D. Meier, and G. Reiss, "Static magnetic proximity effect in Pt layers on sputter-deposited $NiFe_2O_4$ and on Fe of various thicknesses investigated by XRMR", IEEE Trans. Magn. **52**, 4500104 (2016).

[132]C. Klewe, T. Kuschel, J.-M. Schmalhorst, F. Bertram, O. Kuschel, J. Wollschläger, J. Strempfer, M. Meinert, and G. Reiss, "Static magnetic proximity effect in Pt/$Ni_{1-x}Fe_x$ bilayers investigated by x-ray resonant magnetic reflectivity", Phys. Rev. B **93**, 214440 (2016).

[133]P. Bougiatioti, O. Manos, O. Kuschel, J. Wollschläger, M. Tolkiehn, S. Francoual, and T. Kuschel, "Impact of magnetic moment and anisotropy of $Co_{1-x}Fe_x$ thin films on the magnetic proximity effect of Pt", arXiv: 1807.09032.

[134]A. Mukhopadhyay, S. Koyiloth Vayalil, D. Graulich, I. Ahamed, S. Francoual, A. Kashyap, T. Kuschel, and P. S. Anil Kumar, "Asymmetric modification of the magnetic proximity effect in Pt/Co/Pt trilayers by the insertion of a Ta buffer layer", Phys. Rev. B **102**, 144435 (2020).

[135]*SCRIBA Nanotecnologie Srl*, `https://www.scriba-nanotec.com/`.

[136]*About lock-in amplifiers. application note #3*, `http://www.thinkSRS.com/`.

[137]*MFLI User Manual (Revision 45800, 29-Jun-2017)*.

[138]K. Garello, I. M. Miron, C. O. Avci, F. Freimuth, Y. Mokrousov, S. Blügel, S. Auffret, O. Boulle, G. Gaudin, and P. Gambardella, "Symmetry and magnitude of spin-orbit torques in ferromagnetic heterostructures", Nat. Nanotechnol. **8**, 587–593 (2013).

[139]C. O. Avci, K. Garello, M. Gabureac, A. Ghosh, A. Fuhrer, S. F. Alvarado, and P. Gambardella, "Interplay of spin-orbit torque and thermoelectric effects in ferromagnet/normal-metal bilayers", Phys. Rev. B **90**, 1–11 (2014).

[140]M. Tolan, *X-ray scattering from soft-matter thin films* (Springer-Verlag, Berlin Heidelberg, 1999).

[141]A. Gibaud and G. Vignaud, "X-ray and Neutron Reflectivity", in (2009) Chap. Specular Reflectivity from Smooth and Rough Surfaces, pp. 85–131.

[142]H. Kiessig, "Interferenz von Röntgenstrahlen an dünnen Schichten", Annalen der Physik **10**, 769 (1931).

[143]L. G. Parratt, "Surface studies of solids by total reflection of x-rays", Phys. Rev. **95**, 359 (1954).

[144]M. Björck and G. Andersson, "*GenX*: an extensible X-ray reflectivity refinement program utilizing differential evolution", J. Appl. Crystallogr. **40**, 1174–1178 (2007).

[145]S. Macke, *ReMagX - x-ray magnetic reflectivity tool*.

[146]J. Strempfer, S. Francoual, D. Reuther, D. K. Shukla, A. Skaugen, H. Schulte-Schrepping, T. Kracht, and H. Franz, "Resonant scattering and diffraction beamline P09 at PETRA III", J. Synchrotron Radiat. **20**, 541–549 (2013).

[147]J. Krieft, D. Graulich, A. Moskaltsova, L. Bouchenoire, S. Francoual, and T. Kuschel, "Advanced data analysis procedure for hard x-ray resonant magnetic reflectivity discussed for Pt thin film samples of various complexity", J. Phys. D: Appl. Phys. **53**, 375004 (2020).

[148]J. Zak, E. Moog, C. Liu, and S. Bader, "Universal approach to magneto-optics", J. Magn. Magn. Mater. **89**, 107 (1990).

[149]A. Elzwawy, H. Pişkin, N. Akdoğan, M. Volmer, G. Reiss, L. Marnitz, A. Moskaltsova, O. Gurel, and J.-M. Schmalhorst, "Current trends in planar Hall effect sensors: evolution, optimization, and applications", J. Phys. D: Appl. Phys. **54**, 353002 (2021).

[150]"Chapter 9 - Systems and application biopsy", in *Nanomagnetic Materials*, edited by A. Yamaguchi, A. Hirohata, and B. J. Stadler, Micro and Nano Technologies (Elsevier, 2021), pp. 623–712.

[151]G. Reiss, J.-M. Schmalhorst, L. Marnitz, A. Moskaltsova, and G. Maruccio, *Vorrichtung und Verfahren zum Detektieren von magnetischen Partikeln*, `https://register.dpma.de/DPMAregister/pat/PatSchrifteneinsicht?docId=DE102019121379A1`, Feb. 2021.

[152]N. Dohmeier, A. Tavassolizadeh, K. Rott, E. Quandt, D. Meyners, and G. Reiss, "Inverse magnetostrictive stress sensors based on crossed pinned CoFeB/MgO/CoFeB tunnel junctions", J. Appl. Phys. **124**, 064501 (2018).

[153]N. Dohmeier, "Sensors for mechanical stress based on inverse magnetostrictive CoFeB/ MgO/CoFeB tunnel junctions", PhD thesis (Bielefeld University, 2019).

[154]S. Heitmann, A. Hütten, T. Hempel, W. Schepper, G. Reiss, and C. Alof, "Interplay of antiferromagnetic coupling in copper/permalloy combination multilayers", J. Appl. Phys. **87**, 4849–4851 (2000).

[155]L. Marnitz, "Phd thesis", PhD thesis (Bielefeld University, 2021).

[156]L. Marnitz, A. Moskaltsova, J.-M. Schmalhorst, and G. Reiss, "Harmonic Detection of Superparamagnetic Nanoparticles Using the Planar Hall Effect", in preparation (2021).

[157]J. Rivas, M. Bañobre-López, Y. Piñeiro-Redondo, B. Rivas, and M. López-Quintela, "Magnetic nanoparticles for application in cancer therapy", J. Magn. Magn. Mater. **324**, Fifth Moscow international symposium on magnetism, 3499–3502 (2012).

[158] Y. Piñeiro, Z. Vargas, J. Rivas, and M. A. López-Quintela, "Iron oxide based nanoparticles for magnetic hyperthermia strategies in biological applications", Eur. J. Inorg. Chem. **2015**, 4495–4509 (2015).

[159] *CrysTec GmbH*, `http://www.crystec.de/`.

[160] A. Persson, R. S. Bejhed, H. Nguyen, K. Gunnarsson, B. T. Dalslet, F. W. Østerberg, M. F. Hansen, and P. Svedlindh, "Low-frequency noise in planar Hall effect bridge sensors", Sens. Actuator A Phys. **171**, 212–218 (2011).

[161] A. Jacquot, B. Lenoir, A. Dauscher, M. Stölzer, and J. Meusel, "Numerical simulation of the 3 method for measuring the thermal conductivity", J. Appl. Phys. **91**, 4733–4738 (2002).

[162] Z. Chen, H. Nan, Z. Liu, X. Wang, X. Gu, and S. Xiao, "Effect of thermal conductivity of substrate on laser-induced phase transition of $MoTe_2$", J. Raman Spectrosc. **50**, 755–761 (2019).

[163] B. Raquet, "Electronic noise in magnetic materials and devices", in *Spin electronics*, edited by M. Ziese and M. J. Thornton (Springer Berlin Heidelberg, Berlin, Heidelberg, 2001), pp. 232–273.

[164] L. Neumann and M. Meinert, "Influence of the Hall-bar geometry on harmonic Hall voltage measurements of spin-orbit torques", AIP Adv. **8**, 095320 (2018).

[165] L. Liu, C.-F. Pai, Y. Li, H. Tseng, D. Ralph, and R. Buhrman, "Spin-torque switching with the giant spin Hall effect of tantalum", Science **336**, 555 (2012).

[166] C. O. Avci, K. Garello, J. Mendil, A. Ghosh, N. Blasakis, M. Gabureac, M. Trassin, M. Fiebig, and P. Gambardella, "Magnetoresistance of heavy and light metal/ferromagnet bilayers", Appl. Phys. Lett. **107**, 192405 (2015).

[167] S. Woo, M. Mann, A. J. Tan, L. Caretta, and G. S. Beach, "Enhanced spin-orbit torques in Pt/Co/Ta heterostructures", Appl. Phys. Lett. **105**, 212404 (2014).

[168] C. O. Avci, J. Mendil, G. S. D. Beach, and P. Gambardella, "Origins of the Unidirectional Spin Hall Magnetoresistance in Metallic Bilayers", Phys. Rev. Lett. **121**, 087207 (2018).

[169] K. Hasegawa, T. Koyama, and D. Chiba, "Enhanced unidirectional spin Hall magnetoresistance in a Pt/Co system with a Cu interlayer", Phys. Rev. B **103**, L020411 (2021).

[170]A. Moskaltsova, J. Krieft, D. Graulich, T. Matalla-Wagner, and T. Kuschel, "Impact of the magnetic proximity effect in pt on the total magnetic moment of Pt/Co/Ta trilayers studied by x-ray resonant magnetic reflectivity", AIP Adv. **10**, 015154 (2020).

[171]A. Palomino, J. Marty, S. Auffret, I. Joumard, R. Sousa, I. Prejbeanu, B. Ageron, and B. Dieny, "Evaluating critical metals contained in spintronic memory with a particular focus on Pt substitution for improved sustainability", SMT **28**, e00270 (2021).

[172]*EU's Conflict Minerals Regulation*, 2021.

LIST OF TABLES

LIST OF FIGURES

ACKNOWLEDGEMENTS

Finally, I would like to express my sincere gratitude to everyone who contributed to successful realization of this thesis and supported me during this journey. I am extremely grateful that such an opportunity was given to me and during the three and a half years spent at D2 I could grow not only professionally, but also personally and could meet so many wonderful people.

First of all I would like to thank my doctoral supervisor, Prof. Dr. Günter Reiss, for giving me a chance to pursue my Ph.D. in such a great group and always being available for discussion and giving valuable feedback. I am also thankful for the many opportunities I was given to visit numerous conferences and workshops, where I could present my work, learn from other peers and expand my network.

I would also like to express my gratitude to Dr. Jan-Michael Schmalhorst for his support and advice, for numerous discussions and his passion in finding the answer in the piles of measured data.

Another very special thanks I would like to express to Dr. Timo Kuschel, who opened me a world of synchrotrons and gave me an opportunity to take part in various beamtimes. It was a unique experience, including numerous nightshifts and sometimes frustrating measurement sessions. Thank you for various discussions, which often started with "I have just a short question" and two hours later ended up with some clarity and a better understanding of a problem.

For the scientific discussions at the very beginning of my Ph.D. path I wish to thank Dr. Daniel Carsten (Meier), who took his time and patience to teach me and explain the principles of the measurement technique and from the first day encouraged me to learn Python. I am glad I actually listened to his advice.

I wish also to thank Prof. Dr. Markus Meinert for the fruitful discussions and his valuable advice. His knowledge and comments helped to look at some open questions in my work from another perspective.

For the technical support and various e-beam-related troubleshooting I would like to thank Dr. Karsten Rott. His assistance and wide technical knowledge helped me a lot during the various experiments.

Apart from the scientific questions, there were many bureaucratic and administrative ones, which were always quickly and effectively resolved thanks to the help of Aggi Windmann.

I wish to acknowledge EU HORIZON 2020 Program for the financial support in

frame of the MADIA project. Additionally, I would like to thank the whole MADIA consortium, especially Dr. Alek Dediu, Dr. Alessandro Surpi, Prof. Dr. Giuseppe Maruccio, Fausto Sirsi, Dr. Pierpaolo Greco, Dr. Giulia Fosci, Dr. Vitaliy Parkula and the others.

This work would not be accomplished without the amazing atmosphere and team spirit created by the people of D2. Thank you every one for the many laughs in the coffee room, for funny Xmas parties, for dinners after long conference days. Thank you Prof. Dr. Andreas Hütten, Dr. Jan Krieft, Denis Dyck, Tristan Matalla-Wagner, Katharina Fritz, Philipp Zilske, Mareike Dunz, Andreas Becker, Tobias Peters, Johannes Demir, Oliver Ritter, Jan Biedinger, Dr. Niklas Dohmeier, Dr. Oliver Reimer, Dr. Torsten Hübner, Dr. Robin Klett, Dr. Niclas Teichert. A special thanks goes to my office colleagues: Luca Marnitz and Dominik Graulich for a good atmosphere, help and funny moments we had in D2-201.

The list above would not be full without mentioning very special colleagues, who became my friends. Thank you Dr. Alessia Niesen, Dr. Polina Bougiatioti, Dr. Orestis Manos and Dr. Robin Silber for fun dinners and serious discussions and your mental support.

A very special thank goes to Prof. Dr. Sergey Tarapov for him believing in me since my school times, teaching me the very basics of scientific experiment and always encouraging me to move forward and keep asking questions. The scientific and social experience I received from him and his team at Radiospectroscopy Dept. of IRE NASU formed my spirit and helped tremendously in my scientific career.

Of course, of all the people my deepest gratitude goes to my family: my mother and brother, and my sister. No words are enough to express how thankful I am for all the support, no matter what. You encouraged me to not be afraid and to dream big. You taught me, everything is possible if you work hard enough. Thank you from the bottom of my heart.

Thank you. Danke.